UNIVERSITÁ DEGLI STUDI DI ROMA "TOR VERGATA"

MACROAREA di INGEGNERIA

MECHANICAL ENGINEERING MASTER'S THESIS

Analysis of Vortex Induced Vibration of a thermowell by high fidelity FSI numerical analysis based on RBF structural modes embedding

Advisor: **Candidate:**
Prof. Marco Evangelos Biancolini   Alessandro Felici

Co-Advisor:
Ph.D. Ubaldo Cella

Academic year 2019/2020

Ai miei genitori

Table of contents

List of Figures

List of Tables

List of Symbols

β weight of the polynomial correction

γ coefficient of the RBF

ε dissipation rate

θ_{shadow} amplification factor for the shadow rotation

μ dynamic viscosity

μ_t turbulent viscosity

ρ density

ς damping factor

ϕ radial basis function

$[\boldsymbol{\Omega}]$ spectral matrix

ω specific dissipation rate

ω_d damped circular natural frequency

ω_n circular natural frequency

$[\boldsymbol{A}]$ interpolation matrix

A_B cross-sectional area of the beam

A_z directional deformation of the mode in the z direction

A_x directional deformation of the mode in the x direction

$[\boldsymbol{C}]$ damping matrix

$[\boldsymbol{c}]$ modal damping matrix

C_d drag coefficient

C_l lift coefficient

D diameter

E Young's Modulus

f frequency

f_n natural frequency

$\boldsymbol{F}$ modal forces vector

$\boldsymbol{F}_v$ volume forces vector

F_d drag force

F_l lift force

g known value of the function at source point

h polynomial correction

$[\boldsymbol{I}]$ identity matrix

I_B moment of inertia of the beam cross-section

$[\boldsymbol{K}]$ stiffness matrix

$[\boldsymbol{k}]$ modal stiffness matrix

k turbulent kinetic energy

L characteristic length

L_B length of the beam

$[\boldsymbol{M}]$ mass matrix

$[\boldsymbol{m}]$ modal mass matrix

n_{modes} number of considered modes

$[\boldsymbol{P}]$ constraint matrix

p pressure

$\boldsymbol{Q}$ external forces vector

$\boldsymbol{q}$ modal coordinates vector

$\tilde{\boldsymbol{R}}$ Reynolds stress tensor

Re Reynolds number

R_{tip} the distance of the tip of the thermowell from the duct axis

S front area

s interpolation function

St Strouhal number

t	time
Δt	time-step size
U	flow velocity
$\boldsymbol{u}$	velocity vector
$[\boldsymbol{v}]$	modal matrix
$\boldsymbol{v}$	modal shape vector
$\boldsymbol{x}$	position vector
$\boldsymbol{x}_k$	position vector of a source point
X_{shadow}	shadow translation in the transverse direction
$\boldsymbol{y}$	generalized coordinates vector
y^+	non-dimensional wall distance
Z_{shadow}	amplification factor for the shadow translation

List of Abbreviations

CAD   computer aided design

CAE   computer aided engineering

CFD   computational fluid dynamics

CPU   central processing unit

DNS   direct numerical simulation

FDM   finite difference method

FEM   finite element method

FSI   fluid-structure interaction

FVM   finite volume method

GUI   graphical user interface

LCM   local correction method

LES   large eddy simulation

RANS   Reynolds averaged Navier-Stokes equations

RBF   radial basis function

RMS   root mean square

TUI   text user interface

URANS   unsteady RANS

VIV   vortex-induced vibration

Introduction

Today the need for developing multi-physics approaches in order to address modern and complex design challenges is rising. The core of the numerical methods involved is the coupled-field analysis, that allows to determine the combined effects of multiple physical phenomena on a given system. A typical multi-physics phenomenon is the interaction between a fluid and a structure. This particular interaction occurs according to the following options: it can be the working principle of the considered component; it can be due to the lightweight design of the structure or else it can be exploited to finely tune the design.

The Fluid Structure Interaction describes the interaction of a movable or deformable structure with an internal or a surrounding fluid flow; moreover it plays a fundamental role in a wide range of engineering fields, as for example industrial, automotive, aerospace, marine, civil and biomedical. Given the complexity of the differential equations governing those interactions and their associated boundary conditions, it can be inferred that few analytical solutions exist. Relying on numerical simulations or experiments is therefore the only way to tackle the above mentioned problems.

The numerical approaches, based on the coupling of computational fluid dynamics and computational structural dynamics, can be divided in two main categories: the monolithic approach and the partitioned approach. In the former the two sets of equations, governing respectively the fluid dynamics and the structural dynamics, are studied and solved simultaneously within a unified solver; in the latter they are solved separately, with two distinct solvers. In the first approach the interfacial conditions between the solid and the fluid domains are implicit within the solution procedure, whereas in the second one they are taken into account to exchange information (such as in terms of loads and displacements) between the two solving procedures. The monolithic approach is able to guarantee better accuracy and stability of the coupling method but it requires a specific code and, generally speaking, more computational resources; furthermore, at the moment, there is a lack of monolithic solvers capable of dealing with industrial applications involving high fidelity models composed of hundred million of cells. The partitioned approach, on the other hand, allows to use an existing flow solver and a structural solver after the development of a reliable and accurate coupling algorithm, which is able to correctly define the interfacial data exchange conditions. The last task is not easy because it requires complex mapping algorithm able to transfer loads and displacements among different grids (the structural and the fluid dynamical one).

Another possible way of classification is based on the treatment of meshes: the conforming mesh methods and non-conforming mesh methods. In the first case the interfacial conditions are treated as physical boundary conditions and the interface location is treated as a part of the solution, with the consequence that meshes conforming at the interface are needed. It can be so inferred that the nodes have to be equally spaced at the interface. Hence if the structure moves or is deformed, a re-meshing or a mesh update is needed. In the second case the boundary location and the interfacial conditions are treated as constraints imposed on the model equations, therefore non-conforming grids can be used and the re-meshing is not necessary.

Whatever approach is chosen, it must be said that the deformation of the CFD mesh is needed in order to accommodate the shape changes of the structure and consequently to introduce them into the fluid modeling without altering the grid topology. In this work a mesh morphing algorithm based on the Radial Basis Functions will be used to update the CFD mesh according to the derived deformed shape of the structure, doing so exploiting its meshless nature to reduce the mesh deterioration during the morphing actions. The proposed FSI modal approach allows the adaptation of the shape of the deformable structure according to modes superposition during the advancement of the computation. This method, based on the structural modes embedding, proved its efficiency and reliability in many studies and it can be adopted for both transient and steady state FSI analyses. However, the hypotheses behind this method have to be constantly taken into consideration, as it cannot be employed in problems involving non-linearities of any kind, contact or pre-stressed components.

The underlying idea of the proposed workflow is that at each time-step, the fluid forces over the structure surface together with inertial loads are computed as modal forces that determine the amplitude of each modal shape. Superimposing the modal shapes, the overall deformation of the structure is deducible at each instant and can be imposed through mesh morphing. What just stated allows for a transient FSI solution based on the weak coupling approach (so-named "weak" because the data transfer and the mesh update are accomplished at the end of each time-step, whereas in a strong coupling approach they are accomplished at each inner iteration), with a much lower computational cost if compared to other methods, since it eliminates the bottleneck represented by the complex data mapping between the two solvers and makes it suitable for transient FSI simulations with industrial meshes.

In this thesis, the proposed method will be implemented to investigate an industrial problem: the vortex induced vibration of a thermowell immersed in a fluid flow. Thermowells are cylindrical fittings used to protect temperature sensors (as for example thermometers or thermocouples) installed in industrial processes. In such setup the process fluid transfers heat to the thermowell wall which, in turn, transfers heat to the sensor. The usage of a thermowell, other than protecting the sensor from the pressure and chemical effects of the process fluid, allows to easily replace the sensor without draining the vessel or the piping. However, it has to be considered that the thermowell is exposed to the risk of flow-induced vibrations. They are due to the vortex shedding and eventually lead to bending fatigue failure. Hence, in modern applications involving high strength piping and elevated fluid velocity, the dynamics of the system have to be carefully evaluated in order to prevent the above mentioned failures by implementing ad-hoc solutions, as for example twisted square thermowells. A numerical method able to reliably reproduce this kind of interaction is therefore needed to quickly evaluate different designs and reduce the time to market of new products.

With regard to the industrial problem some experimental data are available and the aim of the presented work is to set up a numerical procedure able to model the VIV phenomenon accurately and to reproduce the experimental results. The complexity of the physical phenomenon, influenced by various elements such as the Reynolds number, the mass ratio, the damping, the amplitude and the frequency of the resulting oscillations

(the last one due to the mutual influence between the fluid dynamics filed and the body motions), made this task extremely challenging.

In the first chapter a brief overview of the vortex shedding and the vortex induced vibration phenomena is presented, distinguishing their different observable regimes. In the second chapter an overview of the mathematical formulation of the used FSI method is laid out, namely the theory behind: the CFD modeling, the modal analysis, the modal coordinates formulation, the modal superposition approach for the FSI calculation, the radial basis functions. In the third chapter a two-dimensional analysis used to validate the CFD setup and its results will be shown. In the fourth chapter the procedure followed to perform the FSI analysis by embedding the modes into the CFD solver will be presented and the results of the study on the thermowell will be shown.

1 Vortex shedding phenomenon

Vortex shedding is an oscillating flow that occurs when a fluid flows past a bluff body at specific Reynolds number. In this flow vortices detach periodically and alternately from each side of the body generating a Von Kármán vortex street. An example of vortex shedding past a circular cylinder at Re=105 is shown in Figure 1.1 [1].
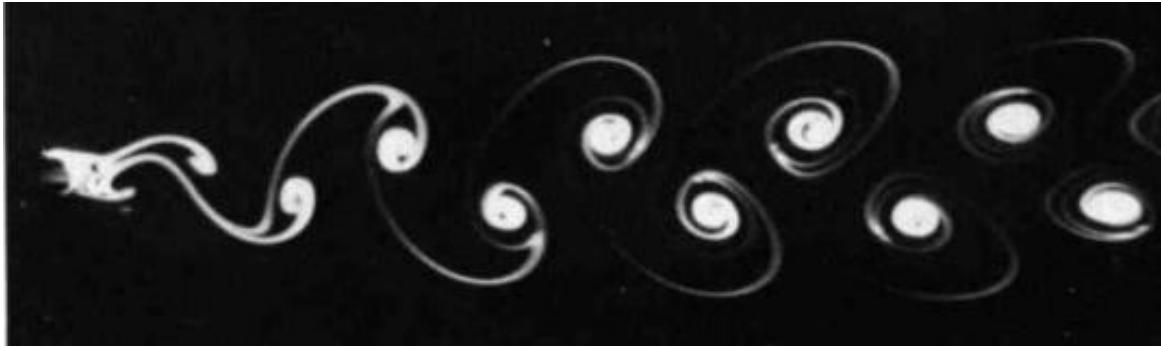
Figure 1.1: Visualization of vortex shedding past a circular cylinder, at *Re=105*

If a circular cylinder is considered, a typical bluff body object of vortex shedding studies and also object of this work, its diameter appears as the characteristic length in the definition of the Reynolds number, as reported in equation 1.1:

$$Re = \frac{\rho U D}{\mu} \tag{1.1}$$

Where ρ is the fluid density, U is the velocity of the oncoming flow, D is the cylinder diameter and μ is the dynamic viscosity of the fluid.

Many studies showed that based on the value of Reynolds number, different flow regimes can be identified [2].

At Re below 4 the flow is creeping laminar without any separation (see Figure 1.2 [1]).
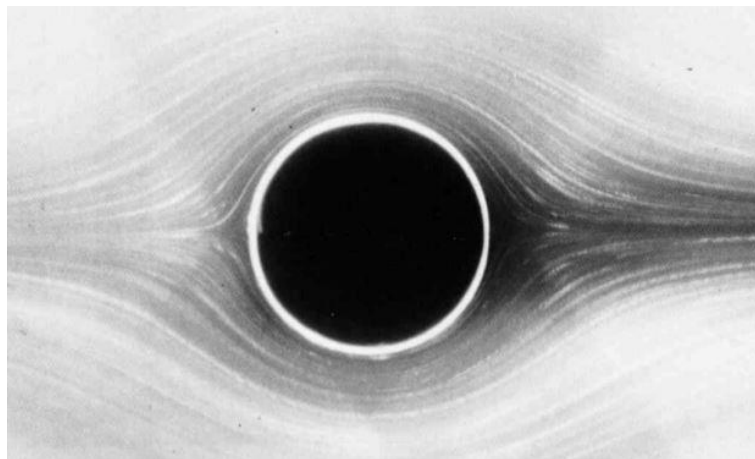
Figure 1.2 Laminar flow past a cylinder at *Re= 0.16*

At *Re* between 5 and 49 the wake of the cylinder is symmetric and steady, characterized by a recirculation region of two symmetrical counter-rotating vortices on each side of the wake (see Figure 1.3 [1]).
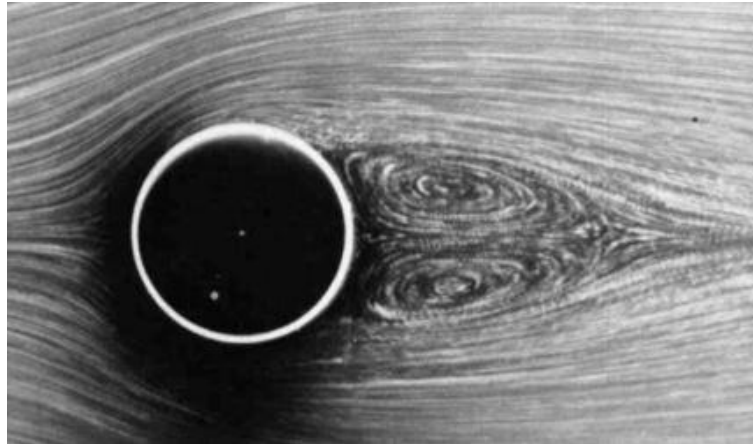
Figure 1.3 Wake past a cylinder at *Re=26*

At *Re* between 49 and 140-194 the recirculation region, often called "bubble", develops instabilities starting from the downstream end of the bubble, giving rise to a laminar vortex shedding. Therefore in this regime a transverse oscillation appears and vortices are shed from the cylinder, losing the symmetry of the flow (as visible in Figure 1.1)

At *Re* between 190 and 260 the flow enters a wake transition regime, in which vortex loops start to originate and transition to turbulence appears in the wake. In this regime streamwise vortex pairs start to form according to the deformation of primary vortices as they are shed. Increasing the *Re* smaller scale vortices start to occur.

At *Re* between 1000 and 200000 the flow enters the shear layer transition regime (also called "sub-critical regime"), in which the instability of the separating shear layers from the sides of the cylinder starts to develop. The boundary layer, which is laminar over the front, eventually separates and breaks up into turbulent wake (see Figure 1.4 and Figure 1.5 [1]), in which it is possible to identify high scale periodic vortices with dimensions of the same order of magnitude belonging to the cylinder diameter.
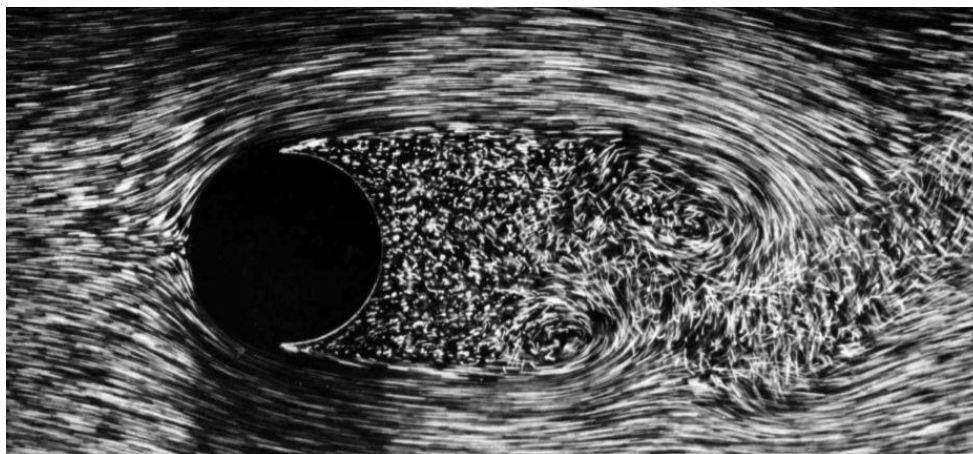
Figure 1.4: Wake past a cylinder at *Re=2000*
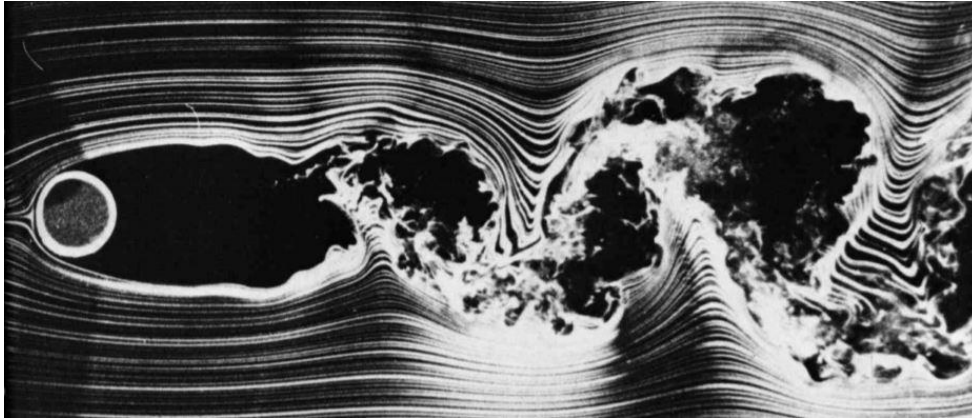
Figure 1.5: Wake past a cylinder at *Re=10000*

As *Re* increases the turbulent transition point in the separating shear layers moves upstream.

At this point, as *Re* increases a separation-reattachment bubble starts to appear, causing the energized boundary layer to separate further downstream. At first, for *Re* higher than 250000, the reattachment happens only on one side of the cylinder (in the so called "asymmetric reattachment regime", or "critical transition regime"); afterwards, at *Re* about $5.3 \cdot 10^5$-$6.5 \cdot 10^5$, the reattachment becomes symmetric ("symmetric reattachment regime", or "supercritical regime") with two separation-reattachment bubbles, one on each side of the cylinder.

At even higher *Re*, beyond 10^6 (called "post-critical regime"), the flow enters the boundary layer transition regime, in which the boundary layer on the surface of the cylinder becomes turbulent. It was assumed that after this point the wake would be fully turbulent without coherent and periodic vortices. Nevertheless, later studies demonstrated the presence of periodic vortex shedding even in this regime [3].

It can be observed clearly that even if the flow behaviour varies according to the Reynold number, the vortex shedding phenomenon is almost always present and it has to be taken into account in every system involving a bluff body immersed in a fluid flow.

To describe the vortex shedding frequency, the Strouhal number is introduced (1.2):

$$St = \frac{fL}{U} \tag{1.2}$$

Where *f* is the frequency of vortex shedding, *L* is the characteristic length (in this case the length related to the diameter of the cylinder *D*). A correlation between the Strouhal number and the Reynolds number has been experimentally demonstrated [4] [5] and it is reported in Figure 1.6 [5].
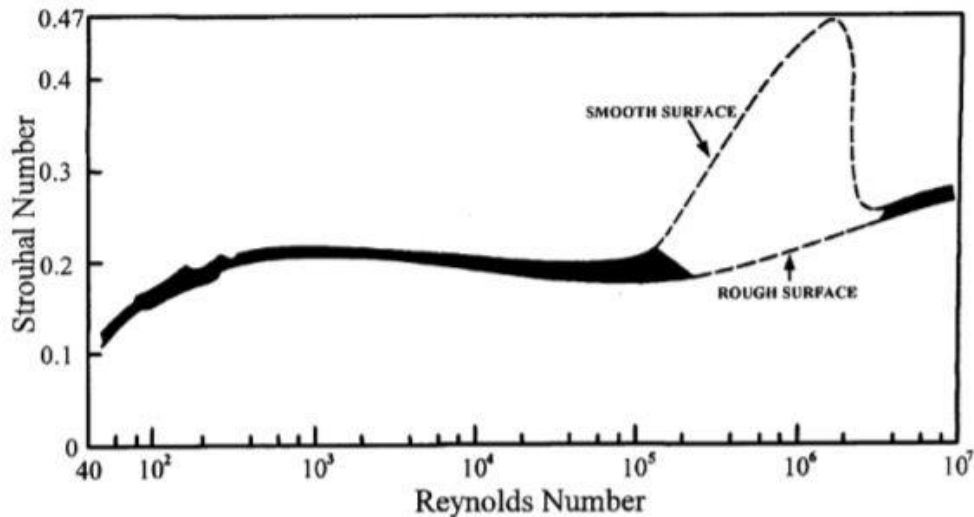
Figure 1.6: Relationship between *St* and *Re*

The vortex shedding phenomenon generates also unsteady fluid forces on the cylinder. In particular the alternating detachment of vortices provokes alternating low-pressure zones on each side of the cylinder. The mentioned low-pressure zone exerts an unsteady cross-flow force (perpendicular to the direction of the flow) with the same frequency as the vortex shedding (the one that appears in the Strouhal number). The amplitude of this cross-flow force varies greatly according to the Reynolds number [4].

If the Strouhal frequency approaches a natural frequency of the flexible body around which the vortex shedding appears, an oscillatory response may occur. Undoubtedly the body oscillations can alter the flow around it. If in this flow-structure coupling a synchronization of vortex shedding and body oscillation happens, then large vibrations can result. This phenomenon is referred to as "lock-in" and it involves vortex induced vibrations compulsorily. Therefore the lock-in condition is used as a criterion to define vortex induced vibrations among other vibrations generated by a fluid flow [6].

It has to be noted that also the streamwise force is unsteady, but with a frequency about twice the cross-flow one, due to the alternating low pressure zones. Therefore other than the above mentioned transverse lock-in, also an in-line lock-in may occur (in the same way as the transverse one, but in the streamwise direction).

The aim of this thesis is to capture the vortex induced vibration of a thermowell numerically, being a thermowell a cylindrical body immersed in a fluid flow. It seems clear that the first step needed to capture the vibrations adequately is the setup of a CFD model able to predict the vortex shedding phenomenon accurately and then a method to setup the FSI analysis is required. In the next chapter the theoretical background of the tools used to accomplish such task will be presented.

2 Theoretical background

In this chapter the theoretical background of the tools used to perform the FSI analysis will be drawn up. In the first place the theory related to the CFD modeling will be introduced, starting from the Navier-Stokes equations until arriving to the RANS modeling and its closure problem. In the second place the proposed high fidelity FSI approach will be introduced, together with an explanation of the basics of the modal theory, of the modal coordinates formulation and of the modal superposition approach. Then, in order to provide a deeper insight into the used mesh morphing technique, the theory bound to the RBFs will be briefly presented. At the end of the chapter, all the introduced tools will be combined into a complete FSI workflow.

2.1 Navier-Stokes equations and their numerical solutions

In order to capture the vortex shedding phenomenon numerically it is necessary to solve the Navier-Stokes equations (i.e. the equations governing every fluid flow), on a properly defined computational domain.

Navier-Stokes equations correspond to the equations of balance of mass and momentum applied to a fluid system. Assuming a Newtonian fluid with constant viscosity and an incompressible flow (i.e. a flow in which the density can be assumed constant, as for example the flow of a liquid or the flow of a gas at low Mach number), they can be written as follows [7] (2.1 and 2.2):

$$\nabla \cdot \boldsymbol{u} = 0 \tag{2.1}$$

$$\rho\left(\frac{\partial \boldsymbol{u}}{\partial t} + \boldsymbol{u} \cdot \nabla \boldsymbol{u}\right) = -\nabla p + \rho \boldsymbol{F_v} + \mu \nabla^2 \boldsymbol{u} \tag{2.2}$$

Where ρ is the fluid density, $\boldsymbol{u}$ is the velocity vector, p is the fluid pressure, t is time, $\boldsymbol{F_v}$ is the volume forces vector, μ is the fluid dynamic viscosity. The first one is referred to as "continuity equation", the second one as "momentum equation". Together they are able to describe every fluid flow and they contain also the description of vorticity, without the necessity to introduce other equations.

It appears clear that together they constitute a system of non-linear partial differential equations, so the definition of initial conditions and boundary conditions is needed.

It is well known that this system of equations has few analytical solutions, therefore in complex problems a numerical approach is needed. Computational fluid dynamics (CFD) is the discipline that takes into account all the different aspects that come into play when dealing with the numerical solution of the Navier-Stokes equations.

Various types of CFD analysis have to be considered [8]: the first possible approach is to directly solve the Navier-Stokes equations on the whole domain in a so called "direct numerical simulation" (DNS). The problem related to this procedure occurs when at high Reynolds number (encountered in most of the practical applications in the engineering fields) the flow becomes turbulent and due to the mechanism of energy cascade [9] small scale vortices appear.

To explain the energy cascade phenomenon it has to be observed that the Reynolds number can be interpreted as the ratio of the inertial forces to the viscous forces within a fluid subject to relative internal movement. Those two forces correspond respectively to the convective term ($\boldsymbol{u} \cdot \nabla \boldsymbol{u}$) and the diffusive term ($\mu \nabla^2 \boldsymbol{u}$) in the momentum equation. At high Re the convective term becomes dominant and the fluid layers start mixing together, therefore the turbulence sets in and causes the energy to be transferred from the higher scales (at which the energy is introduced in the flow, as for example in the form of primary structures of vortices that shed from an immersed body) to the finer ones until the smallest one, called "Kolmogorov scale". At the Kolmogorov scale the viscosity dominates and the turbulent kinetic energy is dissipated into heat. Under proper assumptions the ratio of the smallest scale to the highest one is in the order of magnitude of $Re^{-3/4}$. The above cited assumptions are rarely true, but what matters in this discussion is that the smallest scale of vortices becomes smaller as Re increases. Moreover what has been said referring to spatial scales can be repeated for the temporal ones, with a ratio of about $Re^{-1/2}$.

The result of this phenomenon shows that to correctly perform a DNS the physical domain has to be discretized into a computational domain fine enough to capture and solve the smallest scales of the turbulent flow. The same procedure has to be followed for the temporal discretization. The issue that arises during this procedure is that the number of grid points in the computational domain becomes huge and the time-step size becomes tiny, resulting in the non-viability of the DNS for most applications due to the enormous computational effort that it requires.

To overcome this limitation other models have been developed, such as the Reynolds averaged Navier-Stokes equations (RANS) and the large eddy simulation (LES). With the RANS approach the Navier-Stokes equations are averaged and only the average flow is solved, on the other hand the fluctuations associated to the vorticity are eliminated and their effect on the average flow is modelled. The result of this averaging is that a gird capable of capturing the smallest scales of vortices is not needed anymore (because they are not solved) and a fine temporal discretization is not necessary either; this is the reason why the RANS approach is the least computationally expensive and the most used one. The LES approach falls between the DNS and the RANS because it is obtained thanks to the application of a spatial filter to the Navier-Stokes equations; in this way the turbulent structures which are larger than the filter are solved, whereas the ones smaller than the filter are modelled. Obviously the spatial and temporal discretizations have to be fine enough to capture the filtered scales; once assumed that, the LES modeling falls between the DNS and the RANS not only conceptually but also from the point of view of computational cost, which tends to be closer to the DNS one as the filter dimension becomes lower.

In Figure 2.1 [10] a visual comparison of the results of the three approaches described above applied to the simulation of a jet flow, is shown. The differences between RANS, LES and DNS are clearly visible: the first one is able to capture only the average flow, the second one captures the higher scale structures and the third one solves all the scales of the flow.
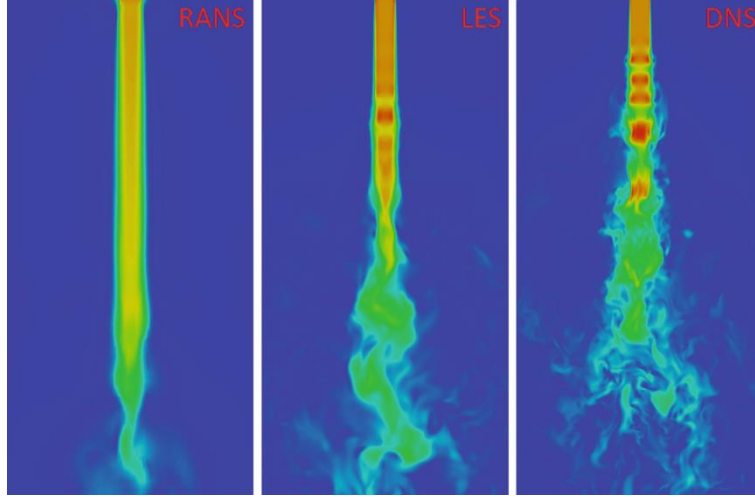
Figure 2.1: Comparison of a RANS, LES and DNS

In various studies [11] [12] [13] the RANS modeling with an adequate turbulence model has demonstrated to be capable of capturing with acceptable accuracy the vortex shedding phenomenon and the associated vortex induced vibrations. It is clear that LES and DNS are able to capture the above cited phenomena too, but the limitations in computational resources and in terms of time availability made them non-viable options for the presented study.

Therefore the unsteady RANS approach was eventually chosen and it will be more accurately described in the next section.

2.2 RANS modeling

In this section the theory behind the RANS modeling will be presented. First of all the RANS equation will be derived starting from the Navier-Stokes equations. In the second step the unsteady term will be introduced into the equations and the closure problem will be investigated. At the end of the chapter a brief recall of the spatial discretization methods, in particular with regard to the finite volume one, will be given.

2.2.1 RANS equations

To derive the RANS equations a time-averaging of the Navier-Stokes equations is implemented [14]. At first the pressure and the velocity fields are decomposed in an average component (averaging with respect to time) plus a fluctuating one (as reported in equations 2.3 and 2.4).

$$\boldsymbol{u}(\boldsymbol{x},t) = <\boldsymbol{u}(\boldsymbol{x},t)> + \boldsymbol{u}'(\boldsymbol{x},t) \qquad (2.3)$$
$$p(\boldsymbol{x},t) = <p(\boldsymbol{x},t)> + p'(\boldsymbol{x},t) \qquad (2.4)$$

Where $\boldsymbol{x}$ is the position vector, $<\boldsymbol{u}>$ and $\boldsymbol{u}'$ are respectively the average and the fluctuating component of the velocity field, $<p>$ and p' represent the same decomposition applied to the pressure field. It has to be noted that the velocity and pressure fields are functions of time and position, the same can be said for their fluctuating

component but not for the average one because it results from a time averaging, hence it can be concluded that it is only a function of position. The time average of the variable $\boldsymbol{u}$ is defined as follows (equation 2.5):

$$< \boldsymbol{u} >= \lim_{T\to\infty} \frac{1}{T} \int_0^T \boldsymbol{u}(\boldsymbol{x}, t)\mathrm{d}t \tag{2.5}$$

Applying this decomposition and then averaging the Navier-Stokes equations (being a matter of fact that the time average of the fluctuations is null and the same can be said for the time derivative of the average component), they can be written as follows (2.6 and 2.7):

$$\frac{\partial <u_i>}{\partial x_i} = 0 \tag{2.6}$$

$$\rho <u_j> \frac{\partial <u_i>}{\partial x_j} = -\frac{\partial <p>}{\partial x_i} + \mu \frac{\partial^2 <u_i>}{\partial x_j^2} - \rho \frac{\partial <u_i'u_j'>}{\partial x_j} \tag{2.7}$$

These last two equations (referred to as "RANS equations") are written using the repeated index notation, with the indices varying between 1 and 3 and identifying the three components of the vector they refer to. The volume forces action has been ignored, being not relevant for this discussion. Now the unknowns that these equations are solved for, are the average pressure and velocity fields. However it can be observed the presence of an additional term: the average of the product of the fluctuations, known as "Reynolds stress tensor" and defined as follows (2.8):

$$R_{ij} = -\rho <u_i'u_j'> \tag{2.8}$$

With the pair of indices i and j pointing to a component of the tensor $\widetilde{\boldsymbol{R}}$.

In order to obtain equations containing only the average velocity and the average pressure, the closure of the RANS equations is needed and it is accomplished by modeling the Reynolds stress term as a function of the average flow, removing any reference to the fluctuating component of the velocity.

Before dealing with the closure problem, it has to be observed that in equation 2.7 the non-stationary term is absent, therefore large scale periodicity phenomena (like vortex shedding) can't be modelled with a simple RANS approach.

That is the reason why the unsteady RANS (URANS) model was developed.

2.2.2 URANS equations

The main difference between RANS and URANS is that in this second approach the time derivative of the average velocity is included (in the momentum equation), despite the fact that it is formally independent of time. There are two main arguments [14] adopted to justify the retention of this term: one is based on the appeal to ergodicity of turbulent flows; the other is associated with time scales actually needed to obtain a reasonably accurate average.

23

The first argument is based on the ergodic hypothesis implying that time averaging is equal to ensemble averaging.

The ensemble average of N realizations of the variable $\boldsymbol{u}$ is defined as follows (equation 2.9):

$$\langle \boldsymbol{u}(\boldsymbol{x},t) \rangle = \frac{1}{N} \sum_{k=1}^{N} \boldsymbol{u}^{(k)}(\boldsymbol{x},t) \tag{2.9}$$

It appears clear that the ensemble average of a quantity is time dependent. Following the same procedure as above (see subsection 2.2.1), the ensemble averaged Navier-Stokes momentum equation can be written as below (equation 2.10):

$$\rho \frac{\partial \langle u_i \rangle}{\partial t} + \rho \langle u_j \rangle \frac{\partial \langle u_i \rangle}{\partial x_j} = -\frac{\partial \langle p \rangle}{\partial x_i} + \mu \frac{\partial^2 \langle u_i \rangle}{\partial x_j^2} - \rho \frac{\partial \langle u_i' u_j' \rangle}{\partial x_j} \tag{2.10}$$

But if ensemble averaging is equivalent to time averaging then the 2.10 can be written as follows (2.11):

$$\rho \frac{\partial <u_i>}{\partial t} + \rho <u_j> \frac{\partial <u_i>}{\partial x_j} = -\frac{\partial <p>}{\partial x_i} + \mu \frac{\partial^2 <u_i>}{\partial x_j^2} - \rho \frac{\partial <u_i' u_j'>}{\partial x_j} \tag{2.11}$$

The problem concerning this argument is that the hypothesis behind the ergodic hypothesis are not satisfied: the first hypothesis is that the flow has to be stationary, whereas not all the turbulent flows considered in practical applications are stationary; the second one is about the formal limit $T \to \infty$, that has to be observed in the time averaging process implied in the definition of ergodic theorems. The consequence of what just said is that the time dependence of the ensemble-averaged equations cannot be used to deduce time dependence of the time-averaged equations.

The second argument relies on the hypothesis that the considered flow has at least two widely-separated time scales, one much greater than the other (i.e. the first associated to large-scale fluid motions and the second to turbulent fluctuations). Therefore the Reynolds average can be defined in terms of a generic time scale T contained between the two scales cited above and far enough from both of them, as follows (2.12):

$$<\boldsymbol{u}> = \frac{1}{T} \int_0^T \boldsymbol{u}(\boldsymbol{x},t) \mathrm{d}t \tag{2.12}$$

Hence now $<\boldsymbol{u}>$ depends on time with respect to the slower time scale and the turbulent fluctuations have been averaged. By substituting this definition of time average to the one proposed earlier, it is possible to derive again the URANS equation 2.11.

Even this argument has its own flows: most turbulent flows contain far more than two time scales and the time scale T used to time-average is not well defined. Despite that, this is the most commonly-used justification for retaining the time-derivative in the URANS equations.

Once that the time-dependence of the equations has been solved, what is still left is the closure problem.

2.2.3 Turbulence modeling

Physically the fluctuations in the velocity field are an effect of turbulence, therefore the Reynolds stresses represent the effect of the stochastic turbulent motion on the average flow.

Simplifying to the extreme, turbulence creates vortices that mix the flow, diffusing the momentum in the same way the molecular diffusion does through the pressure gradient and the viscous diffusion which are the two components of the stress tensor. Hence the extra term in the RANS equations can be interpreted as an additional stress tensor due to turbulence, which is the reason why it is called "Reynolds stress tensor". It seems clear that, at this point, the closure problem is translated into the definition of an adequate turbulence model.

The Reynolds stresses can be obtained either from a constitutive relation (similar to the one used to derive from the stress tensor his two components, namely the pressure gradient and the diffusive term in the Navier-Stokes equations) or by solving modelled transport equations for the Reynolds stresses [15]. The first approach is known as first-order, eddy-viscosity modeling, meanwhile the second approach describes second-order or differential Reynolds stress models.

In various studies [11] [12] [13] the SST k-ω turbulence model has demonstrated to be capable of capturing with acceptable accuracy the vortex shedding phenomenon and the associated vortex induced vibrations. For these reasons it has been chosen in this application too and will be explained more in depth.

SST k-ω model is one of the eddy-viscosity models, which are based on the Boussinesq analogy between molecular and turbulent transport. In these models the Reynolds stresses are obtained from the following equation (2.13) [15]:

$$-\rho < u_i'u_j' > = -\frac{2}{3}\rho k\delta_{ij} + 2\mu_t S_{ij} \tag{2.13}$$

Where k is the turbulent kinetic energy (defined as $u_{i,i}'^2/2$), δ_{ij} is the Kronecker delta, μ_t is the turbulent viscosity, S_{ij} is the i,j component of the mean strain rate tensor defined as follows (2.14):

$$S_{ij} = \frac{1}{2}\left(\frac{\partial < u_i >}{\partial x_j} + \frac{\partial < u_j >}{\partial x_i}\right) \tag{2.14}$$

It has to be specified that whereas the dynamic viscosity is a physical property of the fluid, on the other hand the turbulent viscosity is a property of the flow. In this way the unknown fluctuations have been expressed as a function of turbulent kinetic energy and turbulent viscosity, that happen to be the new unknowns.

To obtain these two quantities several eddy viscosity models have been developed and classified in terms of number of transport equations solved in addition to the RANS equations:

- Zero-equation models: Mixing length, Cebeci-Smith, Baldwin-Lomax, etc.;
- One-equation models: Wolfstein, Baldwin-Barth, Spalart-Allmaras, k-model, etc.;
- Two-equations models: k-ε, k-ω, k-τ, k-L, etc.;
- Three-equations models: k-ε-A;

- Four-equations models: v2-f model.

Shear-stress transport (SST) k-ω is a two-equations eddy-viscosity model developed to blend the robust and accurate formulation of the k-ω model in the near-wall region with the free-stream independence of the k-ε model in the far field [16].

The standard k-ε is a semi-empirical model based on transport equations for turbulent kinetic energy and its dissipation rate, referred to as ε. The model transport equation for k is derived from the exact equation, whereas the one for ε is obtained using physical reasoning (see equations 2.15 and 2.16):

$$\frac{\partial(\rho k)}{\partial t} + \frac{\partial(\rho k <u_i>)}{\partial x_i} = \frac{\partial}{\partial x_j}\left[\left(\mu + \frac{\mu_t}{\sigma_k}\right)\frac{\partial k}{\partial x_j}\right] + G_k + G_b - \rho\varepsilon - Y_M + S_k \tag{2.15}$$

$$\frac{\partial(\rho\varepsilon)}{\partial t} + \frac{\partial(\rho\varepsilon <u_i>)}{\partial x_i} = \frac{\partial}{\partial x_j}\left[\left(\mu + \frac{\mu_t}{\sigma_\varepsilon}\right)\frac{\partial\varepsilon}{\partial x_j}\right] + C_{1\varepsilon}\frac{\varepsilon}{k}(G_k + C_{3\varepsilon}G_b) - C_{2\varepsilon}\rho\frac{\varepsilon^2}{k} + S_\varepsilon \tag{2.16}$$

Where: G_k is the generation of k due to mean velocity gradients; G_b is the generation of k due to buoyancy; Y_M is the contribution of the fluctuating dilatation in compressible turbulence to the dissipation rate; $C_{1\varepsilon}$, $C_{2\varepsilon}$ and $C_{3\varepsilon}$ are constants; σ_k and σ_ε are the turbulent Prandtl number for k and ε; S_k and S_ε are possible additional source terms. G_k, G_b and Y_M can be calculated from other known quantities but they will not be studied in depth in this discussion. $C_{1\varepsilon}$, $C_{2\varepsilon}$, $C_{3\varepsilon}$, σ_k and σ_ε are model constants, with standard accepted values (determined through experimental calibration) that have been found to work fairly well for a wide range of flows.

Once k and ε are determined through the above cited equations, it is possible to combine them to calculate the turbulent viscosity with the following (2.17):

$$\mu_t = \rho C_\mu \frac{k^2}{\varepsilon} \tag{2.17}$$

Where C_μ is a constant with standard accepted value as for the ones above.

It has to be specified that the k-ε model is derived assuming fully turbulent flow, therefore it is only valid for those types of flows.

The standard k-ω is an empirical model based on transport equations for turbulent kinetic energy and the specific dissipation rate, referred to as ω and defined as the ratio of ε to k. The two equations are implemented as follows (2.18 and 2.19):

$$\frac{\partial(\rho k)}{\partial t} + \frac{\partial(\rho k <u_i>)}{\partial x_i} = \frac{\partial}{\partial x_j}\left(\Gamma_k \frac{\partial k}{\partial x_j}\right) + G_k - Y_k + S_k \tag{2.18}$$

$$\frac{\partial(\rho\omega)}{\partial t} + \frac{\partial(\rho\omega <u_i>)}{\partial x_i} = \frac{\partial}{\partial x_j}\left(\Gamma_\omega \frac{\partial\omega}{\partial x_j}\right) + G_\omega - Y_\omega + S_\omega \tag{2.19}$$

Where: G_ω is the generation of ω; Γ_k and Γ_ω represent the effective diffusivity of k and ω; Y_k and Y_ω are the dissipation of k and ω due to turbulence; S_ω is a possible additional source term. All the above terms, apart

from the last one, can be calculated from other known quantities and according to given constants; however they will not be studied in depth in this discussion.

Once k and ω are determined through the above cited equations, it is possible to combine them to calculate the turbulent viscosity with the following (2.20):

$$\mu_t = \alpha^* \frac{\rho k}{\omega} \tag{2.20}$$

Where α^* can be calculated from other known quantities.

As aforementioned the SST k-ω model is a blend of k-ω and k-ε. In order to achieve this the k-ε has been converted into a k-ω formulation, resulting in a model similar to the k-ω except for some refinements: both models are multiplied by a blending function (designed to be one in the near-wall region, activating the standard k-ω, and zero away from the surface, activating the transformed k-ε) and added together; the SST k-ω incorporates a damped cross-diffusion derivative term in the ω equation; the definition of μ_t is modified to account for the transport of the turbulent shear stress; the modeling constants are different from the standard formulation. These refinements make the SST k-ω model more accurate and reliable than the k-ω for many types of flows.

The SST k-ω is implemented as follows (2.21 and 2.22):

$$\frac{\partial(\rho k)}{\partial t} + \frac{\partial(\rho k <u_i>)}{\partial x_i} = \frac{\partial}{\partial x_j}\left(\Gamma_k \frac{\partial k}{\partial x_j}\right) + G_k - Y_k + S_k \tag{2.21}$$

$$\frac{\partial(\rho \omega)}{\partial t} + \frac{\partial(\rho \omega <u_i>)}{\partial x_i} = \frac{\partial}{\partial x_j}\left(\Gamma_\omega \frac{\partial \omega}{\partial x_j}\right) + G_\omega - Y_\omega + D_\omega + S_\omega \tag{2.22}$$

Where D_ω is the cross-diffusion term, that derives from the transformation of the k-ε model into the k-ω formulation. As before stated one of the differences with the standard k-ω lies in the blending functions that appear in the calculation of the different terms (μ_t, α^*, Y_k, Y_ω, D_ω, etc.).

In many studies both k-ε and k-ω formulations revealed to have their own pros and cons [17] [18]. The k-ε is a robust approach and it is optimal for high turbulent flows but it performs poorly in complex flows involving severe pressure gradient, separation, high swirling and strong streamline curvature. Moreover it lacks sensitivity to adverse pressure gradients and is numerically stiff when equations are integrated through the viscous sub-layer, where they are treated with damping functions that have stability issues. On the other hand the k-ω performs better than the k-ε for wall-bounded boundary layer, free shear, and low Reynolds number flows. Moreover it is appropriate for boundary layer flows under adverse pressure gradient and separation, but it requires mesh resolution near the wall, it tends to over-estimate the magnitude of the separation and it is too sensitive to inlet free-stream turbulence properties.

The SST formulation combines the best of the two above mentioned: the use of a k-ω formulation in the inner parts of the boundary layer makes the model usable all the way down to the wall through the viscous sub-layer but it switches to a k-ε formulation away from the wall (where the k-ε is ideal for predicting flow behaviour)

and thereby avoids the common k-ω problem according to which the model is too sensitive to the inlet free-stream turbulence properties. Moreover, by taking into account the transport of turbulent shear stress, it is able to produce accurate predictions of the onset and the magnitude of flow separation under adverse pressure gradients.

It seems clear that the SST k-ω model is the best candidate for the here presented work, as it was also highlighted in the above cited studies.

2.3   Spatial discretization

The introduced equations, namely the URANS equations and the turbulence model equations, have to be solved on the physical domain of interest. Despite the simplification introduced by the averaging process and the turbulence modeling, allowing to solve the equations on a coarser computational domain, the obtained system of non-linear partial differential equations cannot be analytically solved in most practical cases, therefore a numerical solution is needed.

The numerical methods used to solve systems of this kind aim to represent and evaluate the partial differential equations in the form of algebraic equations. The way this can be obtained depends on the chosen method. In the scope of CFD the main used ones are the finite volume method (FVM), the finite element method (FEM) and the finite difference method (FDM). It should be noted that all the cited spatial discretization methods can be used to solve both the Navier-Stokes equations and the URANS equations (coupled with the turbulence model equations). Obviously, as before stated, in the first case a much higher grid resolution is needed but in conclusion the implementation of the methods is the same.

2.3.1   Finite volume method

The commercial CFD code that will be used in this thesis is based on the FVM, therefore a brief recall of the idea behind it will be exposed.

FVM is used to solve equations that can be written in conservative form (as in equation 2.23), like the Navier-Stokes equations, defined on a control volume Ω [8].

$$\frac{\partial u_i}{\partial t} + \nabla \cdot \bar{F}(u_i) = S_u(u_i) \tag{2.23}$$

Where: $\bar{F}$ is a generic vector function of the scalar variable u_i and S_u is a generic source term.

The first step is to integrate equation 2.23 over the control volume Ω, as reported in equation 2.24:

$$\int_\Omega \frac{\partial u_i}{\partial t} + \int_\Omega \nabla \cdot \bar{F}(u_i) = \int_\Omega S_u(u_i) \tag{2.24}$$

Applying the divergence theorem to the second term, it can be written as follows (2.25):

$$\int_{\Omega} \frac{\partial u_i}{\partial t} + \int_{\partial\Omega} \bar{F}(u_i) \cdot \hat{n} = \int_{\Omega} S_u(u_i) \qquad (2.25)$$

Where: $\partial\Omega$ is the boundary of the volume Ω and $\hat{n}$ is its normal.

This latter equation can be written also for a generic control volume Ω_j (also called "cell") obtained through a discretization of the volume Ω (2.26):

$$\int_{\Omega_j} \frac{\partial u_i}{\partial t} + \int_{\partial\Omega_j} \bar{F}(u_i) \cdot \hat{n} = \int_{\Omega_j} S_u(u_i) \qquad (2.26)$$

If a CFD application is considered, the physical domain of interest (Ω) is discretized into a computational domain composed of hexahedron or tetrahedron (Ω_j). Therefore the boundary of the cell consists of six or four faces and the second term in equation 2.26 can be decomposed into six or four components associated to the respective faces. If a generic number of faces for each cell, n_f, is considered, then the 2.26 can be written as follows (2.27):

$$\int_{\Omega_j} \frac{\partial u_i}{\partial t} + \sum_{k=1}^{n_f} \int_{\partial\Omega_{j_k}} \bar{F}(u_i) \cdot \hat{n} = \int_{\Omega_j} S_u(u_i) \qquad (2.27)$$

Now a control point has to be defined for each cell. Different possible approaches can be considered in this specific regard. The one used in the chosen commercial CFD code is the cell-centred control volume, in which the control point is at the centre of the cell. Chosen the control point, a series of approximations is introduced: the variable is assumed to be constant inside the cell (but different from cell to cell) and equal to its value in the cell centre (this is the reason why the computational grid has to be refined where high gradients of the unknown quantities are expected), therefore the source term is constant inside the volume and the vector function $\bar{F}$ is constant on the considered face. Hence all the quantities can be extracted from the integrals.

The time derivative can be approximated with a finite difference method in time. Usually the vector function $\bar{F}$ is gradient; if this is the case, the scalar product with the normal vector can be interpreted as a directional derivative and it can be approximated with a finite difference scheme in space, using the values of the variable associated to the centre of the surrounding cells.

By doing this, the starting partial differential equation can be written as an algebraic equation. Applying this procedure to all the cells, a system of coupled algebraic equations is obtained and it can be solved with a method of choice. Once the system is solved, the value of the variable u_i is known at discrete locations in the domain (centres of the cells).

The above described is one possible implementation of the FVM: many variations exist but the underlying idea remains the same.

2.4 High fidelity FSI

The FSI approach used in this thesis is based on the modal theory [19] [20]: the structural deformation can be thought as a linear superimposition of the modal shapes of the body itself, so that by importing the modal shapes in the CFD solver with a mesh morphing tool, the numerical grid can be made implicitly elastic.

In this section the theory related to the proposed FSI approach will be explained. At first the modal theory will be addressed, then the modal coordinates formulation will be introduced and applied in order to derive the modal superposition method used for the proposed FSI approach. Ultimately, the basics of the radial basis functions will be given, being the theory behind the used morphing tool.

2.4.1   Modal analysis

In structural dynamics a modal analysis aims to calculate the structural modes, which are a set of inherent properties of a body consequences of its geometry, material composition and working boundary conditions. Each mode is defined by a modal frequency and is characterized by a modal damping and shape.

In specific, the modal frequencies are the frequencies at which the structure would tend to vibrate naturally when subjected to a disturbance and the modal shapes are the patterns of the motions of the structure at each natural frequency.

The number of modes of a body is equal to the number of its degrees of freedom, which are infinite in the case of continuum structure but a finite amount of them can be found if the structure is discretized for a finite elements method (FEM) analysis. Structural modes define how a structure reacts to a static or dynamic loading (under the hypothesis of linearity), therefore they can be used in FSI analysis.

For a generic n-degrees-of-freedom system (for example n masses virtually positioned on the nodes of the mesh for a FEM structural analysis), the second order differential system of equations of motion can be written in matrix form as (2.28) [21]:

$$[M]\ddot{y} + [C]\dot{y} + [K]y = Q \tag{2.28}$$

Where: $[M]$ is the mass matrix, $[C]$ is the damping matrix, $[K]$ is the stiffness matrix, Q is the external forces vector (that may vary in time), y is the generalized coordinates vector. From the point of view of a FEM structural analysis: $\ddot{y}$, $\dot{y}$ and y are respectively the nodal acceleration, velocity and displacement vectors; $[M]$, $[K]$ and $[C]$ are respectively the structural mass, damping and stiffness matrices; and Q is the vector of forces applied to the masses positioned on the nodes.

The modal analysis aims to calculate the modes of a structure seen as a conservative system, i.e. without gain or dissipation of energy. This implies that the system is subjected to neither damping nor external forces (i.e. free and undamped vibrations). Under this hypothesis the equation of motion can be written as a homogeneous system of equations (2.29):

$$[M]\ddot{y} + [K]y = 0 \tag{2.29}$$

Fundamental in the study of vibrations are the synchronous motions, defined as the solutions of this system in which all the coordinates have the same time dependence. Therefore in synchronous motion the structure assumes a fixed-shape displacement pattern and only its amplitude can change. Mathematically this type of motion can be represented by (2.30):

$$y_j(t) = v_j g(t) \quad j=1,2,..,n \tag{2.30}$$

Where v_j are constant amplitudes and $g(t)$ is a function of time, the same for all the coordinates.

Using the 2.30, it can be observed that from the 2.29 descends an eigenvalue problem that can be written as follows (2.31):

$$[K]v = \omega_n^2[M]v \tag{2.31}$$

Where the eigenvectors v are the modal shapes and the eigenvalues ω_n are the circular natural frequencies (from which the modal natural frequencies can be derived using $\omega_n = 2\pi f_n$). If n is the dimension of the system, under appropriate hypothesis the eigenvalue problem has n solutions, with each solution consisting of a modal shape and its natural frequency.

It is well known that the eigenvectors are not univocally determined: whereas the ratio between any two of its components is fixed, the magnitude of the vector cannot be defined in a categorical way. It follows that the shape of the natural modes is unique, as opposed to the amplitude.

To make each eigenvector unique, the respective magnitude has to be assigned. This process is known as "normalization" and the resulting eigenvectors are referred to as normal modes. A very convenient normalization is done with respect to masses, meaning that each mode has a unit modal mass, as follows for the i-th mode (2.32):

$$v_i^T[M]v_i = 1 \tag{2.32}$$

Which results also in (2.33):

$$v_i^T[K]v_i = \omega_{n,i}^2 \tag{2.33}$$

2.4.2   Modal coordinates formulation

An important characteristic of the above introduced eigenvectors is that they are orthogonal with respect to both stiffness and mass matrices. Mathematically (2.34 and 2.35):

$$v_j^T[M]v_i = 0 \quad i \neq j \tag{2.34}$$

$$v_j^T[K]v_i = 0 \quad i \neq j \tag{2.35}$$

Therefore the eigenvectors are linearly independent.

This last characteristic suggests to introduce a new reference system in which the equations can be uncoupled so that each contribution of a mode to the total structure deformation is isolated [20].

In this view the modal matrix is introduced, with its columns equal to the normalized eigenvectors (2.36):

$$[v] = [v_1 v_2 \dots v_n] \tag{2.36}$$

For which, considering the 2.32 and the 2.34, the following relationship is valid (2.37):

$$[v]^T [M][v] = [I] \tag{2.37}$$

Where $[I]$ is the identity matrix. For the stiffness matrix, relying on the 2.33 and the 2.35, the following definition is introduced (2.38):

$$[\Omega] = [v]^T [K][v] = \begin{pmatrix} \omega_{n,1}^2 & \cdots & 0 \\ \vdots & \ddots & \vdots \\ 0 & \cdots & \omega_{n,n}^2 \end{pmatrix} \tag{2.38}$$

$[\Omega]$ is known as "spectral matrix" and it has the eigenvalues on its diagonal and zero in all the other positions.

The modal matrix is used to define the modal vector coordinates as follows (2.39):

$$q = [v]^{-1} y \tag{2.39}$$

By substituting the definition 2.39 in the 2.28, pre-multiplying by $[v]^T$ both terms and retaining the 2.37 and the 2.38, the following equation is obtained (2.40):

$$[I]\ddot{q} + [v]^T [C][v]\dot{q} + [\Omega]q = [v]^T Q \tag{2.40}$$

To uncouple the equations in this last system, the matrix $[v]$ is required to make the damping matrix diagonal. This can be done if the damping matrix can be expressed as a linear combination of the mass and stiffness matrices, as reported in the following relationship (2.41):

$$[C] = a[M] + b[K] \tag{2.41}$$

Following this approach, each equation of the system 2.40 can be written as follows (2.42):

$$m_{ii}\ddot{q}_i + c_{ii}\dot{q}_i + k_{ii}q_i = F_i(t) \tag{2.42}$$

Where: [m], [c] and [k] are the matrices resulting from the aforementioned substitutions, respectively referred to as modal mass, modal damping and modal stiffness matrices; the same goes for F, defined modal forces vector. For the sake of convenience the 2.42 is usually expressed as (2.43):

$$\ddot{q}_i + 2\varsigma_i \omega_{n,i}\dot{q}_i + \omega_{n,i}^2 q_i = \frac{F_i(t)}{m_{ii}} \tag{2.43}$$

Where $\omega_{n,i}$ is the rotational natural frequency (that can be written also as $\omega_{n,i} = \sqrt{\frac{k_{ii}}{m_{ii}}}$) and ς_i is the damping factor (defined as $\varsigma_i = \frac{c_{ii}}{2m_{ii}\omega_{n,i}}$).

From the 2.43 it appears clear that each mode acts as a single-degree-of-freedom dynamic system and the overall system response can be calculated as a linear superimposition of each mode response, allowing to take into account only a subset of structural modes in the FSI analysis.

2.4.3 Static FSI using modal superposition

If the deformation velocity is higher than the velocity of loads application, the FSI phenomenon can be considered as static and the 2.43 can be simplified as follows (2.44):

$$\omega_{n,i}^2 q_i = \frac{F_i}{m_{ii}}$$

(2.44)

Or (2.45):

$$q_i = \frac{F_i}{k_{ii}}$$

(2.45)

It has to be observed that the modal mass m_{ii} is equal to one if the modes are normalized with respect to the mass. The modal force F_i can be derived from the CFD loads (integrating the structural loads weighted by the eigenvectors) and it is related to pressure and shear stresses acting on the structure.

At this point, proceeding backward and taking into account the 2.45 and the 2.39, the nodal displacement vector can be expressed as follows (2.46):

$$y = \sum_{i=1}^{n} v_i q_i = \sum_{i=1}^{n} v_i \frac{F_i}{k_{ii}}$$

(2.46)

Once the nodal displacement vector is known, the whole deformation of the structure in steady state condition is determined using this linear combination of the selected number of modes weighted by their modal coordinates.

As was hinted before, the continuous structure object of the FSI analysis has to be discretized into a mesh (i.e. a computational grid) to derive, with an apposite FEM modal analysis, its natural frequencies and modal shapes. When the structure is discretized, it can be seen as a system of interconnected masses virtually positioned on the nodes of the mesh, each of them having the motion given by the resolution of equation 2.28. Therefore the discrete system has a finite number of masses and degrees-of-freedom (differently from the continuous one, having infinite degrees-of-freedom and modes), and consequently it has finite vibration characteristics.

Moreover beyond a certain frequency, the natural modes are not excited. This statement can be explained observing that in static cases the structure behaves as a low-pass filter, being modes at lower frequency more important in the structural response (because they have the highest energy levels and are, then, physically prominent). Therefore it is possible to calculate and use a limited number of the lowest-frequency modes of

the structure. This operation is known as "modes truncation" and the minimum number of modes to retain in order to perform an accurate FSI analysis can be found considering their modal participation factor.

2.4.4   Unsteady FSI using modal superposition

If the deformation velocity is comparable or lower than the velocity of loads application or, more in general, the physical phenomenon studied through the FSI analysis cannot be considered as static, the entire 2.43 has to be considered. In this case the solution is the following (2.47):

$$
q(t) = e^{-\varsigma\omega_n t}\left[q_0\cos(\omega_d t) + \frac{\dot{q}_0 + \varsigma\omega_n q_0}{\omega_d}\sin(\omega_d t)\right] +
$$
$$
+ e^{-\varsigma\omega_n t}\left\{\frac{1}{m\omega_d}\int_0^t e^{-\frac{b(t-\tau)}{2m}} f(\tau)\sin[\omega_d(t-\tau)]d\tau\right\}
\tag{2.47}
$$

Where: the solution has been written omitting the indices, but it has to be seen as relative to the considered modal coordinate; ω_d is the damped circular frequency, defined as $\omega_d = \omega_n\sqrt{1-\varsigma^2}$; q_0 and $\dot{q}_0$ are the boundary conditions, respectively initial modal coordinate and initial modal velocity.

The formulation of the integral in the 2.47, known as "Duhamel integral", assumes that the reaction of the system subjected to a force $f(\tau)$ can be expressed as the summation of the reactions of the system to the single impulses constituting the total force. If the acting force F can be considered constant within every time-step of integration, the 2.47 can be written as (2.48):

$$
q(t) = e^{-\varsigma\omega_n t}\left[q_0\cos(\omega_d t) + \frac{\dot{q}_0 + \varsigma\omega_n q_0}{\omega_d}\sin(\omega_d t)\right] +
$$
$$
+ e^{-\varsigma\omega_n t}\left\{\frac{F}{\omega_d}\left[\frac{4\omega_d}{\varsigma^2\omega_n^2 + 4\omega_d^2} - e^{-\varsigma\omega_n t}\frac{2\varsigma\omega_n\sin(\omega_d t) + 4\omega_d\cos(\omega_d t)}{\varsigma^2\omega_n^2 + 4\omega_d^2}\right]\right\}
\tag{2.48}
$$

This solution can be adopted to update every modal coordinate in a time marching algorithm. At this point the nodal displacement vector can be calculated as in the static case (2.49), with the only difference that in this case the modal coordinates used as weights are time-dependent.

$$
\mathbf{y} = \sum_{i=1}^n \mathbf{v}_i q_i(t)
\tag{2.49}
$$

As for the static case it is possible to calculate and use a limited number of the modes of the structure, but in this case the number of retained modes is defined on the basis of excited frequencies.

2.5   Radial basis functions

The mesh morphing tool used in this work is based on the radial basis functions (RBFs). Therefore in this section a recall of the basic theory behind the RBF will be given.

2.5.1 Mesh morphing

As previously highlighted, in an FSI approach like the one presented in this thesis, the numerical grid is made implicitly elastic. This becomes necessary as the fluid dynamics equations are solved on a given computational grid and the grid points have to be moved to follow the deformation of the immersed structure.

To accomplish this task a mesh morpher is needed: a tool capable of modifying a given mesh without changing its topology [20]. The starting mesh is the result of the discretization of the physical domain of interest (necessary to solve the equations numerically) and it is obtained through a series of operations aiming to generate a grid of appropriate quality and able to capture the studied phenomenon. It appears clear that any mesh distortion introduces a reduction of the mesh quality, therefore the morpher has to minimize this effect still allowing for significant modification of the shapes.

As previously stated the mesh morphing method adopted in this thesis hinges on the use of a system of radial basis functions with the aim to produce a solution for the mesh movement, from a set of source points and their displacements. This approach allows to generate surface shape changes and volume mesh smoothing. Moreover, in the morphing tool a smoother capable of reducing volume mesh distortion and preserve an adequate mesh quality is implemented.

It is unquestionable that a morphing approach allows to generate shape modifications directly in the solving stage of the CFD analysis instead of re-generating the mesh, saving a lot of human and CPU time. When thinking about the amount of times that a shape modification occurs during an FSI analysis, the advantages of the mesh morphing approach are evident.

2.5.2 RBFs based technique

The RBF technique allows to exactly control surfaces locally and to manage deforming volumes thanks to its meshless nature.

RBFs are mathematical functions able to interpolate everywhere in the space a function defined at discrete points, giving the exact value at original points. Therefore after generating a set of source points with an associated displacement, RBFs are used to interpolate, on a distance basis, the scalar information known at the source points on the domain in which the functions are not zero valued.

The quality and the behaviour of the interpolation depends on the function and on the kind of chosen basis function: RBFs can be classified depending on the type of support they guarantee (i.e. the domain in which the function is not zero), that can be local (referred to as "compact support") or global. Some of the most common radial functions with global support are shown in Table 2.1; in Table 2.2 typical functions with compact support are reported [19] [20].

Name	Abbreviation	$\phi(r)$
Polyharmonic spline	PHS	r^n, n odd
Thin plate spline	TPS	$r^n\log(r)$, n even
Multiquadric biharmonics	MQB	$\sqrt{a^2 + (\epsilon r)^2}$
Inverse multiquadric biharmonics	IMQB	$\dfrac{1}{\sqrt{a^2 + (\epsilon r)^2}}$
Quadric biharmonics	QB	$1 + (\epsilon r)^2$
Inverse quadric biharmonics	IQB	$\dfrac{1}{1 + (\epsilon r)^2}$
Gaussian biharmonics	GS	$e^{-\epsilon r^2}$

Table 2.1: RBF with global support

Name	Abbreviation	$\phi(r) = f(\xi), \xi \leq 1, \xi = \dfrac{r}{R_{sup}}$
Wendland C^0	C0	$(1 - \epsilon\xi)^2$
Wendland C^2	C2	$(1 - \epsilon\xi)^4(4\epsilon\xi + 1)$
Wendland C^4	C4	$(1 - \epsilon\xi)^6\left(\dfrac{35}{3}\epsilon\xi^2 + 6\epsilon\xi + 1\right)$

Table 2.2: RBF with compact support

RBFs can be defined in an n-dimensions space and are function of the distance that, in the case of morphing, can be assumed as the Euclidean norm of the distance between two points in the space.

The above mentioned interpolation function is composed of the RBF ϕ and of a polynomial term h, whose degree depends on the chosen basis. This polynomial term is added to assure uniqueness of the problem and polynomial precision, allowing to prescribe rigid body translations exactly. If m is the number of source points, the interpolation function can be written as follows (2.50):

$$s(\boldsymbol{x}) = \sum_{i=1}^{m} \gamma_i \phi\big(\lVert \boldsymbol{x} - \boldsymbol{x}_{k_i} \rVert\big) + h(\boldsymbol{x}) \tag{2.50}$$

Where $\boldsymbol{x}_{k_i}$ is the position vector of the i-th source point.

A radial basis interpolation exists if the coefficients γ and the weights of the polynomial term allow to guarantee the exact function values at the source points and the polynomial term gives zero contributions at source points. Mathematically (2.51 and 2.52):

$$s(\boldsymbol{x}_{k_i}) = g_i, 1 \leq i \leq m \tag{2.51}$$

$$\sum_{i=1}^{m} \gamma_i P(\boldsymbol{x}_{k_i}) = 0 \tag{2.52}$$

Where: g_i is the known value of the function at the i-th source point; the 2.52 has to be written for all polynomials P with a degree less than or equal to that of polynomial h. The minimal degree of polynomial h depends on the chosen RBF.

A unique interpolation solution exists if the basis function is a conditionally positive definite function. If the basis functions are conditionally positive definite of order less than or equal to two, a linear polynomial h can be used (2.53):

$$h(x) = \beta_1 + \beta_2 x_1 + \beta_3 x_2 + \cdots + \beta_{n+1} x_n \tag{2.53}$$

Where, as before stated, n is the number of dimensions of the space in which the RBF is defined (three if it is referred to the physical space) and, therefore, the x_i are the components of the position vector. Using a linear polynomial the exact recover of the rigid body translations is guaranteed.

The values for the coefficients γ of the RBF and the weights β of the linear polynomial h can be obtained by solving the system (2.54):

$$\begin{bmatrix} A & P \\ P^T & 0 \end{bmatrix} \begin{pmatrix} \gamma \\ \beta \end{pmatrix} = \begin{pmatrix} g \\ 0 \end{pmatrix} \tag{2.54}$$

Where $[A]$ is the interpolation matrix obtained by calculating all the radial interactions among source points, with the radial distances between them (2.55):

$$A_{ij} = \phi\left(\left\|x_{k_i} - x_{k_j}\right\|\right), 1 \le i \le m, 1 \le j \le m \tag{2.55}$$

$[P]$ is the constraint matrix that results from balancing the polynomial contribution. If the space in which the RBF is defined is the physical one, it contains the coordinates of the source points in the space (2.56):

$$[P] = \begin{bmatrix} 1 & x_{k_1} & y_{k_1} & z_{k_1} \\ 1 & x_{k_2} & y_{k_2} & z_{k_2} \\ \vdots & \vdots & \vdots & \vdots \\ 1 & x_{k_m} & y_{k_m} & z_{k_m} \end{bmatrix} \tag{2.56}$$

It is clear that the RBF interpolation works for scalar fields. For the smoothing problem (in which, formally, a vector field is prescribed) each component of the displacement filed prescribed at the source points is interpolated, once the weights and the coefficients of the system have been obtained through the 2.54 for each component (i.e. the three directions in space x, y and z), as follows (2.57):

$$\begin{cases} s_x(x) = \displaystyle\sum_{i=1}^{m} \gamma_i^x \phi\left(\|x - x_{k_i}\|\right) + \beta_1^x + \beta_2^x x + \beta_3^x y + \beta_4^x z \\ s_y(x) = \displaystyle\sum_{i=1}^{m} \gamma_i^y \phi\left(\|x - x_{k_i}\|\right) + \beta_1^y + \beta_2^y x + \beta_3^y y + \beta_4^y z \\ s_z(x) = \displaystyle\sum_{i=1}^{m} \gamma_i^z \phi\left(\|x - x_{k_i}\|\right) + \beta_1^z + \beta_2^z x + \beta_3^z y + \beta_4^z z \end{cases} \tag{2.57}$$

Summarizing: a linear system is built and then solved to find the system coefficients; once the coefficients have been found, the displacement of a given node of the mesh can be calculated as the superimposition of the

radial contribution of each source point (i.e. a known point in space at which a displacement is assigned); applying the calculated displacement to all the nodes of the mesh, a global mesh deformation is obtained, leaving unaltered the grid topology.

2.6 *Modal FSI workflow*

What has been introduced in this chapter until this point will be now combined into a complete FSI workflow [19], corresponding to the one used in the presented thesis.

Starting from the undeformed configuration, the flexible components of the system are extracted and studied through a structural solver in order to extract the chosen number of modes with a modal analysis. The obtained modal shapes are extracted from the FEM solver and employed by the RBF morpher to generate an RBF solution for each shape. In this step the far field conditions and the rigid surfaces need to be constrained, whereas the FEM results need to be mapped on the deformable surfaces.

The advantage of the RBFs is represented by their meshless nature that allows to directly use the shape variations, calculated using the FEM displacements, to deform the CFD computational grid. What just stated removes the complex mapping between the FEM and CFD displacements.

At this point the RBF solutions, representing the selected modal shapes, are imported directly into the CFD solver. By doing so, the RBF solutions are ready to be used to deform the mesh, making it implicitly elastic. This process is known as "RBF structural modes embedding".

To speed up the mesh morphing step, the deformations associated with each modal shape are stored in memory. This is possible because the structural response and the nodes displacement can be obtained with a simple multiplication (2.58):

$$\boldsymbol{x}_{CFD}(t) = \boldsymbol{x}_{CFD_0} + \sum_{i=0}^{k} q_i(t)\Delta\mathbf{x}_i \tag{2.58}$$

Where: $\boldsymbol{x}_{CFD_0}$ is the vector of undeformed nodal positions in the starting mesh; k is the number of modes taken into account; $q_i(t)$ is the modal coordinate of the i-th mode calculated at time t; $\Delta\mathbf{x}_i$ is the vector of displacements for each node introduced by the i-th modal shape. This means that mesh deformations are obtained by linearly superimposing the action of each modal shape amplified by its modal coordinate, previously calculated.

At this point the FSI setup is done and the CFD calculation can begin. The proposed FSI modeling technique falls into the class of weak approaches, because during unsteady analyses the loads are considered frozen during each time-step. Therefore the modal forces employed in the calculation of the modal coordinates with equation 2.48 are computed on the prescribed surfaces (i.e. the deformable ones) by projecting the nodal forces (i.e. fluid pressure and shear computed by the CFD solver) onto the modal shapes. At this point, assuming that

the loads are constant during the considered time-step, the modal coordinates are computed using equation 2.48. Knowing the modal coordinates, the mesh can be updated using equation 2.58 and then the simulation can proceed. This process is re-executed at each time-step until simulation end.
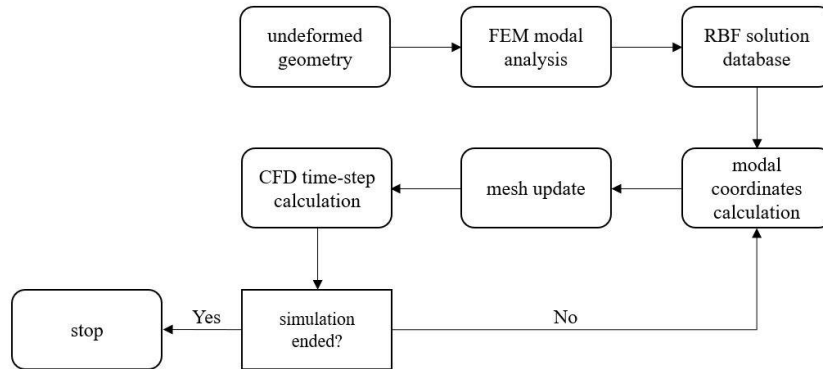
The above described workflow is summarized in Figure 2.2.

Figure 2.2: Unsteady modal superposition FSI workflow

If compared to a traditional two-way FSI approach, this modal superposition FSI method has numerous advantages [19]. First of all the FEM solver can be used just once per simulation at the initialization, thus avoiding data exchange between the two solvers. This latter is clearly a time consuming task and poses problems from the point of view of reliability because transient simulations can last days. A robust method that reduces all the possible liabilities is therefore strongly advised. Moreover, for large models pressure mapping and mesh update can be very time-consuming, making the modal superposition method up to 10-12 times faster than two-way in unsteady analyses.

Apart from having pros, the modal superposition method shows also some cons. The first is that the error introduced by the structural modes embedding and associated with truncation errors has to be considered, especially for steady cases. It can be demonstrated [22] that few modes are needed in order to obtain reliable results. Moreover it has to be taken into account that the modal superposition method can be applied only to linear structures, being the linearity an hypothesis of the modal theory.

Nevertheless, retaining the aforementioned observations, a wide set of problems can be tackled with the modal superposition method: steady FSI analyses, transient simulations with prescribed motions, transient FSI analyses with vibrations excited by the flow, submerged natural modes calculation.

The modal superposition method was successfully employed in various studies covering both transient [19] [23] and static [22] [24] FSI problems, proving its validity.

2.6.1 Used numerical means

The above introduced workflow has been implemented, in the scope of this thesis, in the computer-aided-engineering (CAE) multi-physics platform ANSYS® Workbench™. The modal analysis has been carried out in the FEM solver ANSYS® Mechanical™, whereas the CFD analysis has been conducted in ANSYS® Fluent®. The mesh morphing tool used to set up the modal superposition method for the FSI analysis is RBF Morph™.

Managing the FSI study in a unique platform was quite efficient, because it guaranteed that the position and the units of the numerical models were consistent (necessary for the correct RBF problem setup).

Moreover the mesh morphing tool, RBF Morph, is implemented as an Add-on in Fluent and it has a graphical user interface (GUI) that blends perfectly into Fluent itself, making the setup of the RBF solutions as straightforward as possible.

Other software packages used in the context of this thesis, although to a lesser extent, are ANSYS® ICEM CFD™, ANSYS® CFD-Post™, MATLAB®, SolidWorks® and MeshLab. The contribute of the quoted software to the FSI analysis is not direct, therefore it will be explained in the belonging section.

3 Two-dimensional CFD analysis

Before proceeding with the three-dimensional FSI analysis, a preliminary two-dimensional study (object of this chapter) was conducted in order to define an adequate CFD setup able to capture the vortex shedding phenomenon, a fundamental requirement for the FSI analysis, being the vortex shedding itself the periodic force acting on the thermowell and inducing its vibration.

Despite the fact that a two-dimensional analysis is not able to grasp the three-dimensional phenomena that appear in vortex shedding (by definition every turbulent phenomenon is three-dimensional), it can be used anyway as a preliminary tool to identify a first CFD setup that will be refined in a later three-dimensional study.

The testing conditions chosen for the 2-D analysis consist of an air flow at Re=50000. This value of the Reynolds number falls inside the sub-critical regime of the vortex shedding phenomenon, which is characterized by a very large spectrum of applications, including the one analysed in this thesis. Therefore, as it is in the same regime, it was considered an appropriate testing condition for the proposed study.

To use the 2-D CFD analysis as a preliminary setup for the 3-D FSI study, it was performed with a diameter of the cylinder of 16.764 mm, corresponding to the diameter of the thermowell object of this thesis.

Starting from the chosen diameter of the cylinder, the 2-D geometry was created: to allow an appropriate development of the fluid dynamics of the system the computational domain had to be big enough, therefore it was created as a rectangle with a length of about 68 diameters and a width of about 27 diameters, positioning the circle (i.e. the cylinder in 2-D) at about 25 diameters from the inlet and in the middle of the width. The resulting geometry is shown in Figure 3.1, with the dimensions in millimetres.
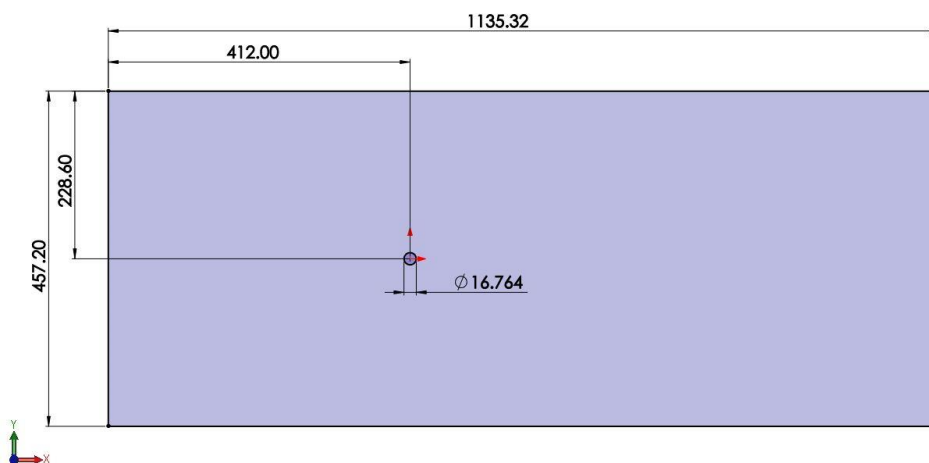

Figure 3.1: 2-D geometry

The above mentioned dimensions were chosen in order to: guarantee the development of the free-stream condition at the inlet (positioned on the left of Figure 3.1); avoid the interactions between the wake of the

41

cylinder and the walls (up and down in Figure 3.1); guarantee the development of the wake behind the cylinder, leaving enough space for the generation of the Von Kármán vortex street.

3.1   2-D computational grid

The afore introduced geometry has been discretized into a computational domain (i.e. a grid) through ANSYS® ICEM CFD™. The obtained mesh is structured, multiblock and composed of quadrilaterals.

The multiblock approach allowed the generation of a structured mesh and the adoption of the appropriate mesh refinements where needed, for example in the wake of the cylinder in which a good mesh resolution is necessary to adequately capture the shed vortices and the wake itself. Moreover it enabled the generation of high quality cells.

The mesh is structured for the known advantages in terms of accuracy and efficiency in calculation, data storage and exchange.

The thickness of the first layer of cells near the cylinder wall has been chosen to obtain an y^+ (non-dimensional wall distance) lower than one, in order to solve the wall boundary layer. By having an $y^+<1$ the first cell is positioned in the viscous sublayer, allowing for a complete description of the boundary layer and for the mesh resolution near the wall needed to implement the SST k-ω turbulence model.

After the first layer at the wall, the thickness of the cells grows with a factor of about 1.2. This allows for a smooth growth of the cells, avoiding rough changes in their dimensions, which is a known source of errors during computation.

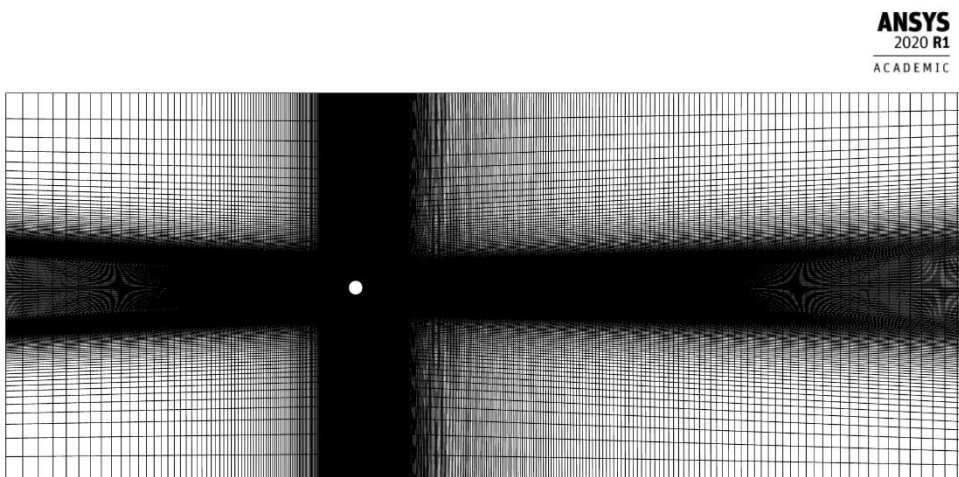The obtained structured mesh, composed of 110722 cells, is shown in Figure 3.2.

Figure 3.2: 2-D grid

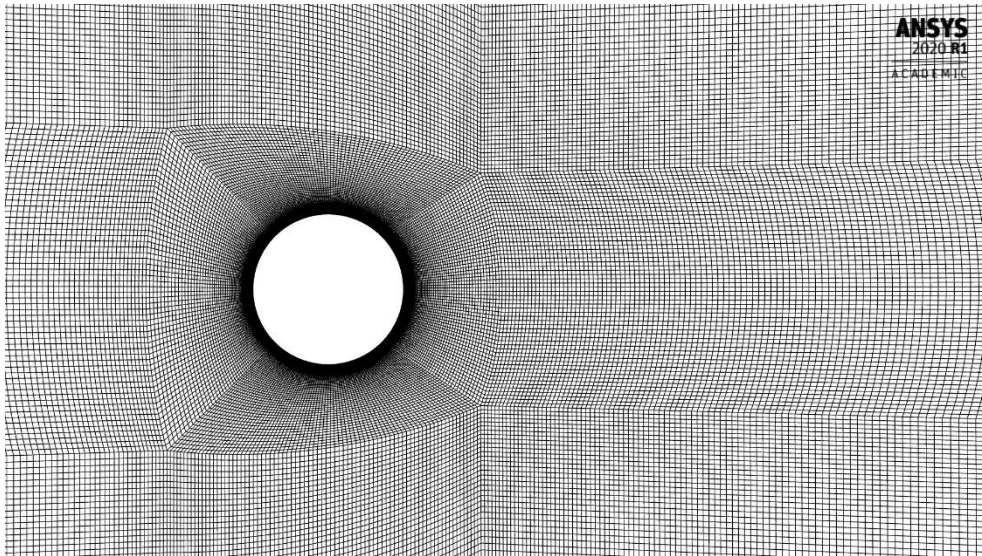In Figure 3.3 a detail of the mesh around the cylinder is visible.

Figure 3.3: 2-D grid, detail around the cylinder

In Figure 3.4 the resolution of the mesh near the wall can be appreciated.
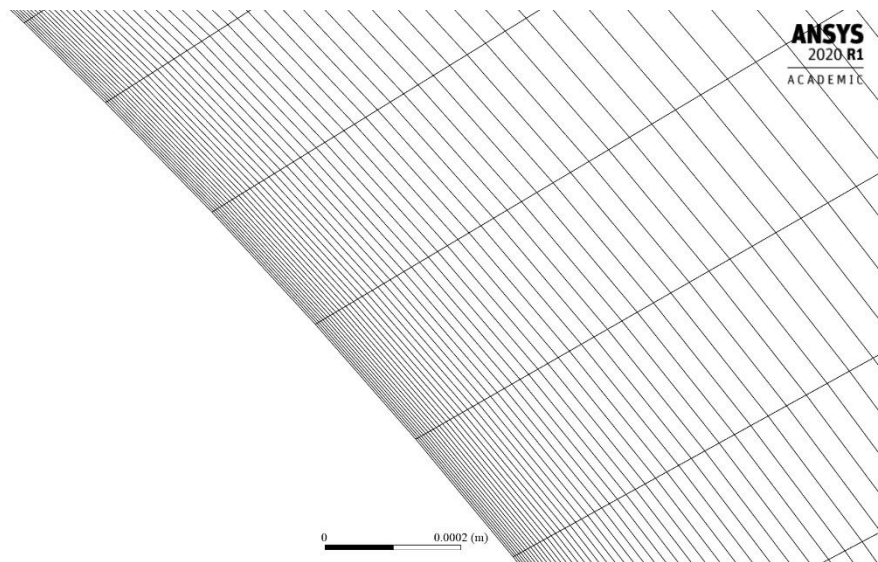

Figure 3.4: 2-D grid, detail near the wall

Inside Fluent a mesh check and a quality evaluation were carried out: the mesh check did not report any failure; the quality evaluation reported a minimum orthogonal quality of 0.782 and a maximum cell squish index of 0.218, both in the high quality range. Therefore the mesh was accepted and the CFD setup was performed.

3.2   2-D CFD setup

In order to adopt RBF Morph as the morphing tool in the proposed FSI method, a three-dimensional CFD solver has to be implemented. Obviously a 3-D solver requires a volume mesh (i.e. a three-dimensional computational grid); therefore, aiming to keep a bi-dimensional solution, the above introduced two-dimensional grid has been extruded in the third dimension for one metre, keeping only one cell in the thickness.

Hence a volume mesh composed of a single planar layer of volumetric cells with a unitary height is obtained and shown in two views in Figure 3.5 and Figure 3.6.
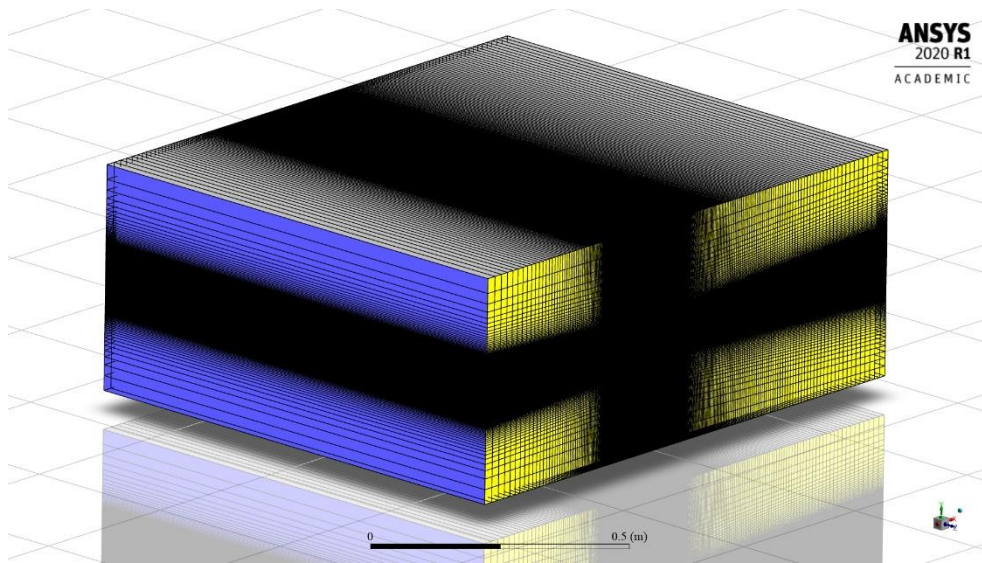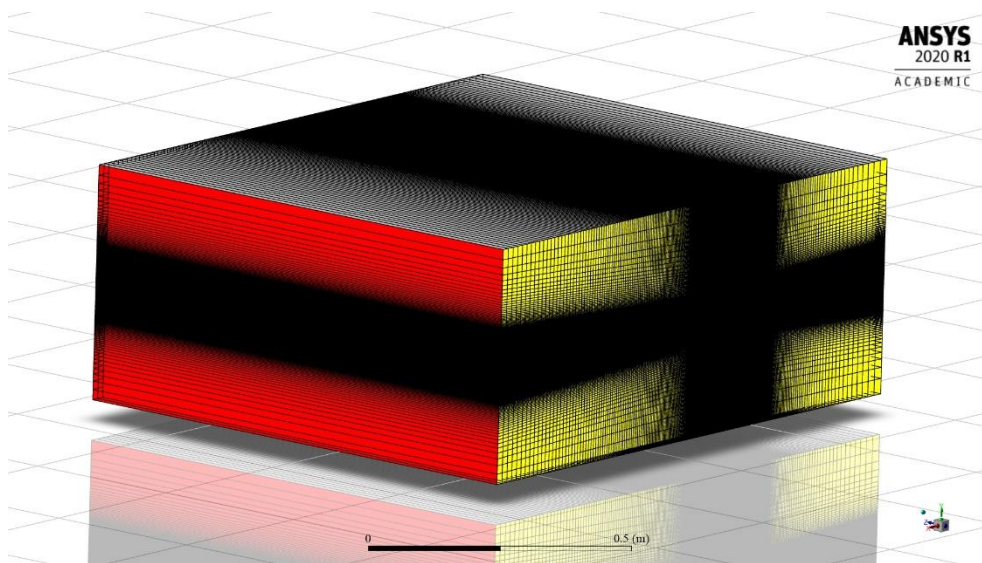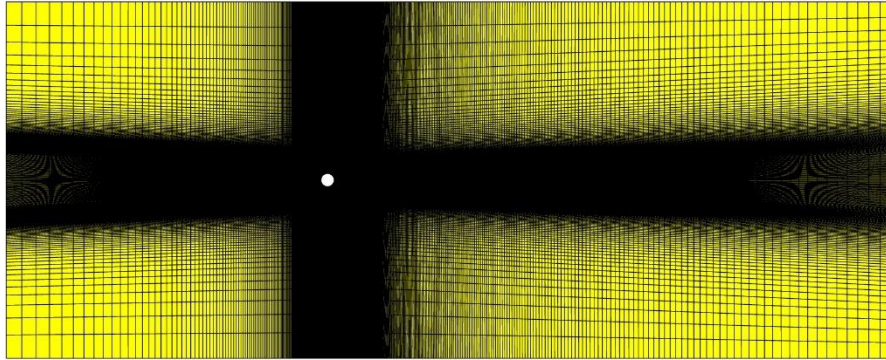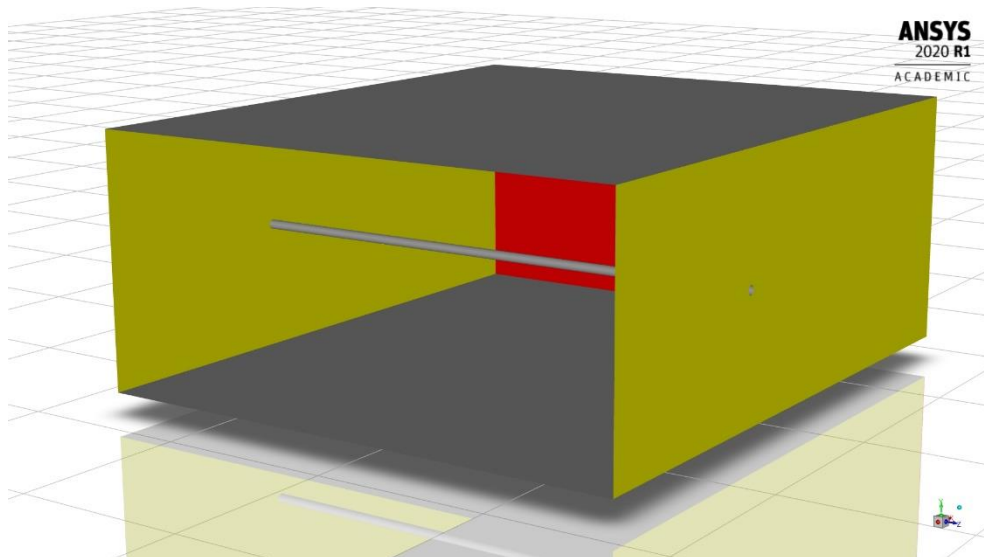
Figure 3.5: 3-D grid, first view

Figure 3.6: 3-D grid, second view

Obviously, if viewed from the top, the grid appears the same as in the pure 2-D case (see Figure 3.7). The extruded cylinder and its positioning inside the domain are visible in Figure 3.8.

Figure 3.7: 3-D grid, top view

Figure 3.8: 3-D grid, extruded cylinder

Once defined the mesh, the setup of the CFD analysis will be now described. It has to be specified that the presented CFD setup is the result of an iterative process that aimed to achieve an accurate and fast solution of the examined case.

As before mentioned the considered fluid is air in standard condition, therefore its density is assumed to be 1.225 kg/m^3 and its dynamic viscosity 1.7894·10^{-5} kg/(m·s). The inlet velocity of the fluid was set to be 44 m/s, resulting in a Reynolds number of about 50000 as before stated.

In the introduced conditions the Mach number is 0.12, therefore the flow can be assumed incompressible. This observation simplifies the calculation, allowing the implementation of a pressure-based solver. Moreover the air density can be assumed constant and the energy equation can be ignored in the modeling process.

Being the vortex shedding an unsteady phenomenon, a transient analysis was implemented.

As stated in chapter 2, an URANS approach is adopted with the SST k-ω turbulence model. The model constants were left with the default values and some available options were enabled: low-*Re* corrections, curvature correction (to sensitize the model to the effects of streamline curvature) with constant and unitary C_{curv} parameter as by default, production Kato-Launder and production limiter (to limit the production term in the turbulence equations avoiding the build-up of turbulent kinetic energy in the stagnation regions, a known problem of the two-equations turbulence models), intermittency transition model (enabled even if the transition was expected in the wake).

A velocity-inlet boundary condition was set to the inlet (blue surface in Figure 3.5), with a 44 m/s velocity in the positive x direction (the reference frame is visible in the bottom-right corner of Figure 3.5) and zero initial gauge pressure. The turbulence at the inlet was specified through a unitary intermittency, a 5% turbulence intensity and the hydraulic diameter of the inlet section.

At the outlet a pressure-outlet was set (red surface in Figure 3.6) with zero gauge pressure and the same turbulence specifications used at the inlet, in case of reverse flow.

Two symmetry conditions were specified for the two yellow surfaces appearing in Figure 3.5 and Figure 3.6 (i.e. the 2-D extruded grid) to enforce the two-dimensionality of the flow.

The cylinder was set as a no slip wall. The top and bottom surfaces (grey in Figure 3.5 and Figure 3.6) were set as zero-shear walls, to model them as free slip walls. This latter condition is needed to ensure that the computational boundary does not affect the flow, in the sense that there is no boundary layer forming from those surfaces.

As far as it concerns solution schemes: the SIMPLE pressure-velocity coupling method was adopted (considered sufficient because the flow is incompressible and at low *Re*), the second order was used for pressure, the second order upwind was adopted for momentum and turbulence parameters, the least squares cell based for gradient (this latter choice was made mainly for the FSI study, where the inclination of the cells is likely increased with the deformation of the mesh). The chosen transient formulation was the first order implicit with a fixed time advancement. The time-step size and the number of internal iterations are the results of a convergence study that will be presented in the next section.

The under-relaxation factors were left as by default.

3.3 *Time-step size*

The time-step size (Δt) and the number of internal iterations are the main parameters influencing the results of the simulations in terms of vortex shedding phenomenology and evolution of the fluid forces acting on the cylinder, therefore an accurate convergence study on those parameters was carried out.

In order to have a better control on the solution process and on the time advancement, the number of internal iterations was set constant, deactivating any computer-controlled convergence condition.

The target of the convergence study was to find the largest time-step size (with the lowest number of internal iterations) capable of adequately capturing the studied phenomenon, with the aim to determine the best compromise between solution accuracy and computational effort.

The fluid forces acting on the cylinder were evaluated in terms of drag coefficient and lift coefficient, defined as follows (3.1 and 3.2 respectively):

$$C_d = \frac{F_d}{\frac{1}{2}\rho U^2 S} \tag{3.1}$$

$$C_l = \frac{F_l}{\frac{1}{2}\rho U^2 S} \tag{3.2}$$

Where: F_d and F_l are the drag and lift forces (i.e. the forcers in the streamwise and cross-flow direction respectively), ρ is the fluid density and S is the frontal area of the cylinder (i.e. diameter times height).

The investigated configurations are summarized in Table 3.1.

Time-step size [s]	Number of internal iterations
$2 \cdot 10^{-4}$	20
$1 \cdot 10^{-4}$	20
$7.5 \cdot 10^{-5}$	30
$5 \cdot 10^{-5}$	30
$2.5 \cdot 10^{-5}$	30
$1 \cdot 10^{-5}$	30
$7.5 \cdot 10^{-6}$	30
$5 \cdot 10^{-6}$	30
$2.5 \cdot 10^{-6}$	30
$1 \cdot 10^{-6}$	30

Table 3.1: Investigated time-step sizes

The simulated flow-time was selected as a compromise between the achievement of a dynamic steady state and a reasonable computation time, ranging between 0.095 s and 0.03 s.

3.4 2-D analysis results

For ease of discussion, the results gathered from only some of the above mentioned configurations will be exposed.

In Figure 3.9 and Figure 3.10 the temporal evolution of the drag and the lift coefficients with a time-step size of $1\cdot10^{-4}$ s and 20 internal iterations is reported.

In Figure 3.11, for the same configuration, the contours of the turbulent kinetic energy after 0.0662 s are shown.
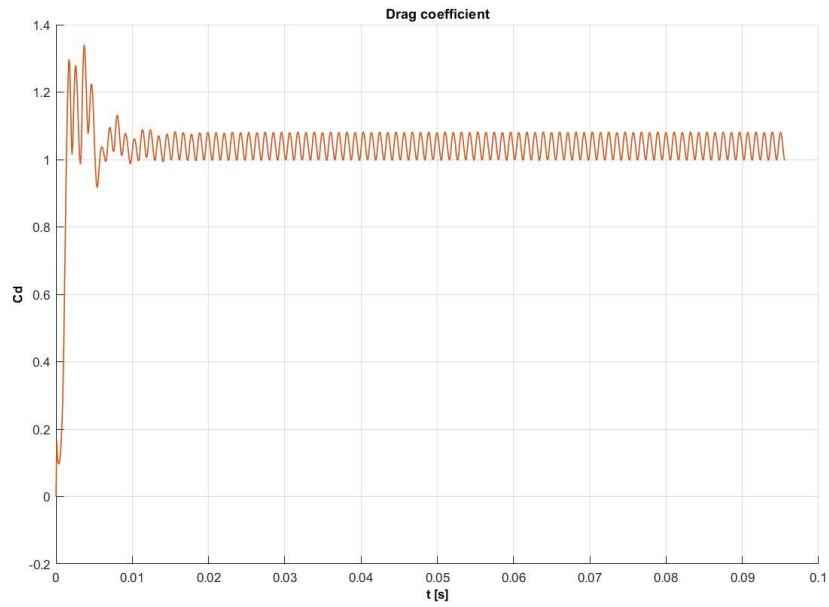

Figure 3.9: Drag coefficient temporal evolution ($\Delta t=1\cdot10^{-4}$ s)
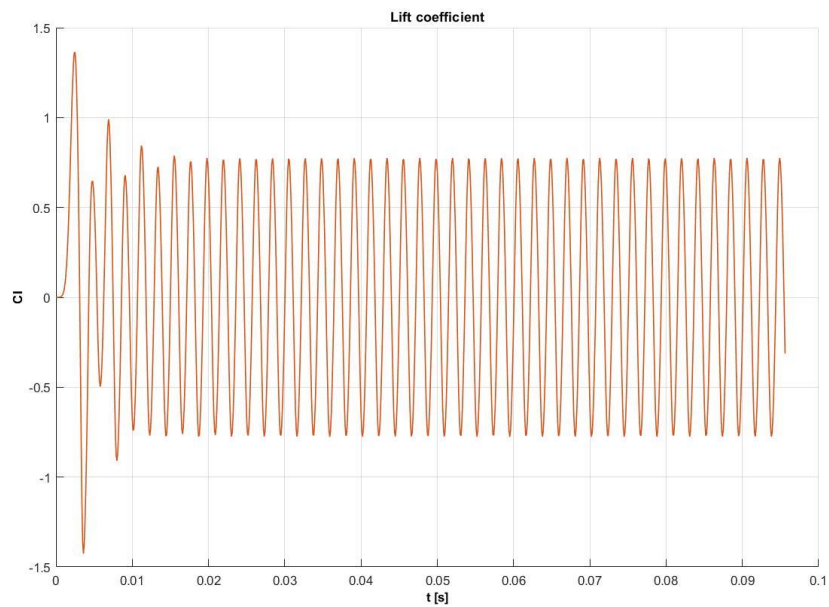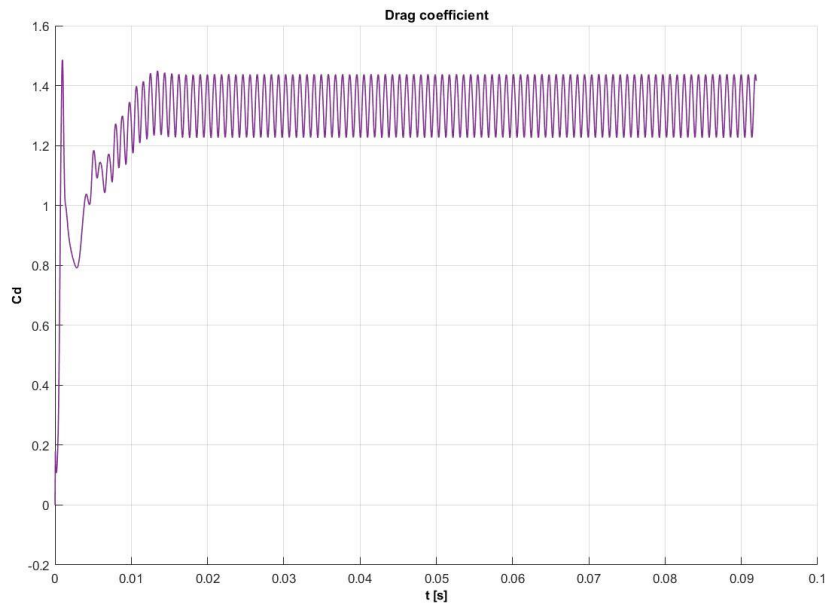

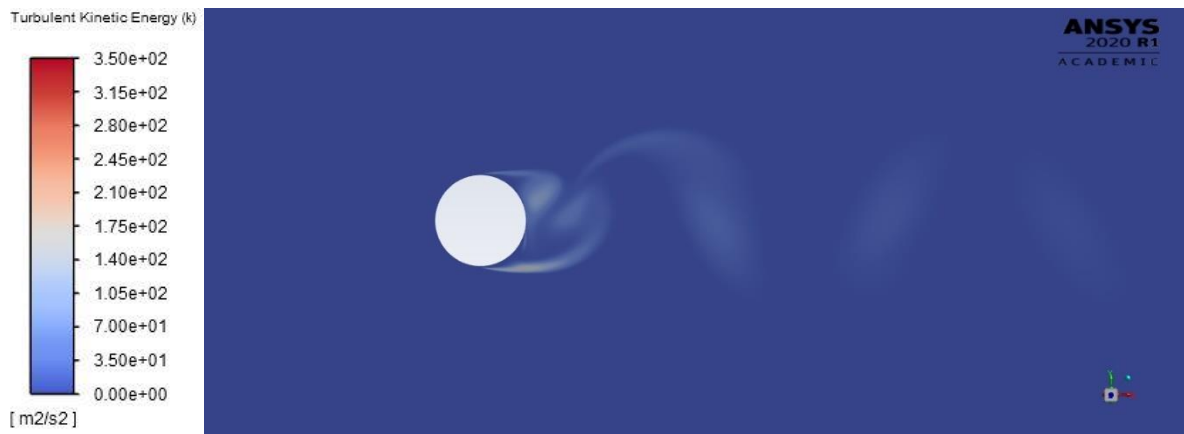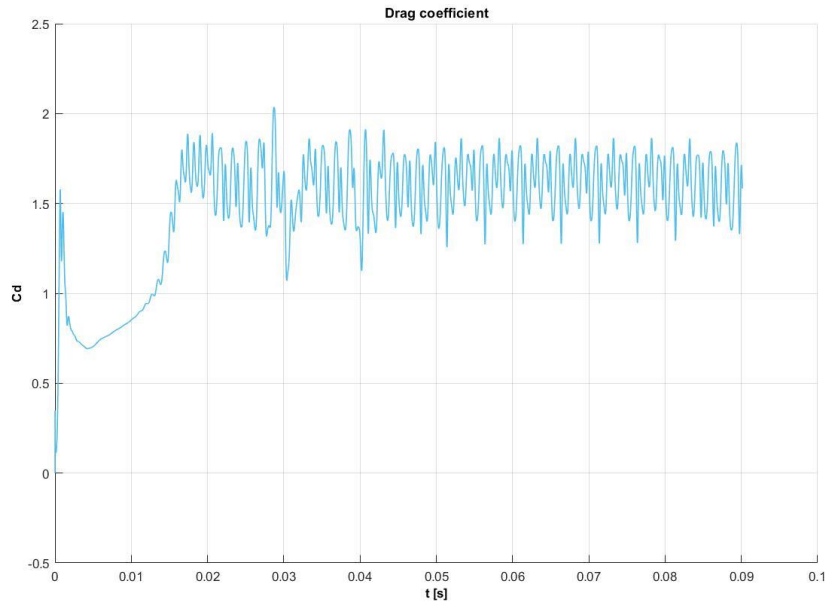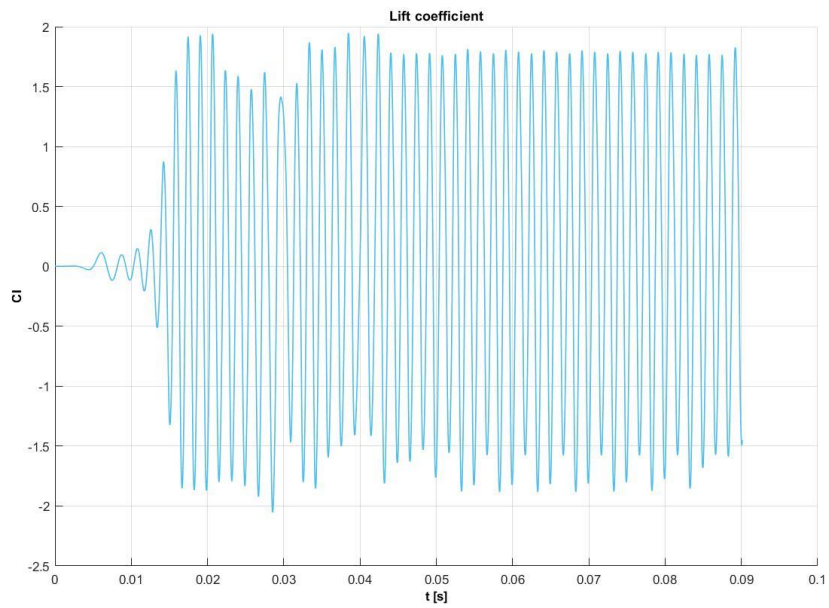**Figure 3.10: Lift coefficient temporal evolution ($\Delta t=1\cdot10^{-4}$ s)**

Figure 3.11: Turbulent kinetic energy contour plot ($\Delta t=1\cdot10^{-4}$ s)

From Figure 3.12 to Figure 3.14 the same as for the previous configuration is reported, differing only with regard to a time-step size of $5\cdot10^{-5}$ s and 30 internal iterations.

Figure 3.12: Drag coefficient temporal evolution ($\Delta t=5\cdot10^{-5}$ s)
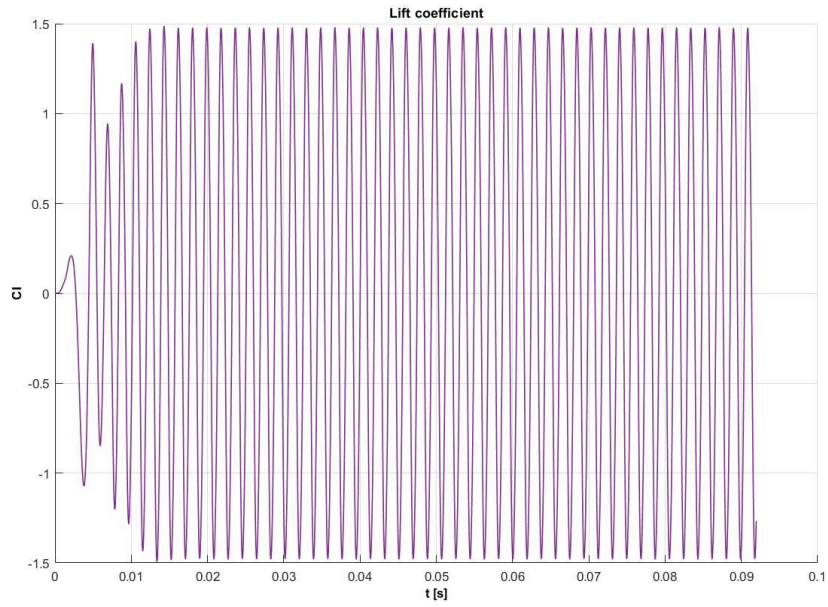
Figure 3.13: Lift coefficient temporal evolution (Δt=5·10^{-5} s)

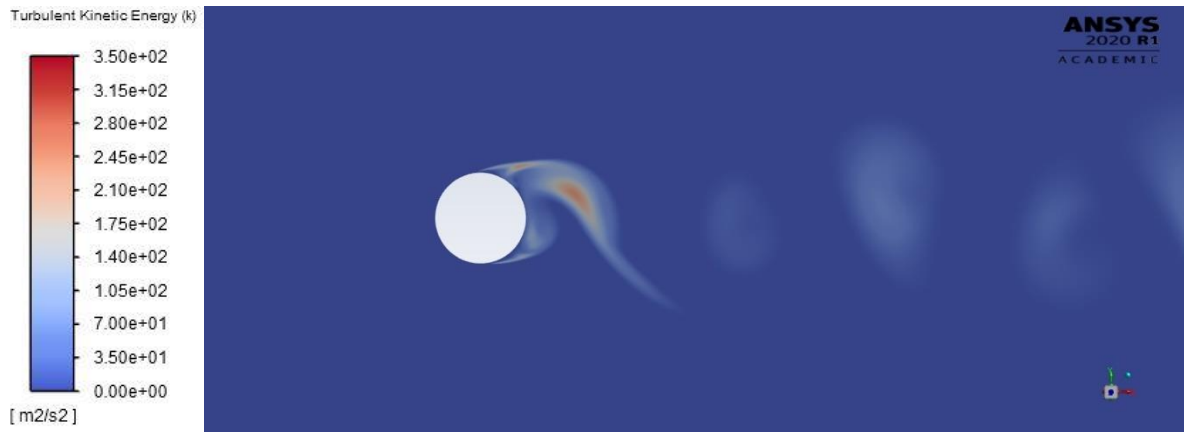**Figure 3.14: Turbulent kinetic energy contour plot (Δt=5·10^{-5} s)**

From Figure 3.15 to Figure 3.17 the same as for the previous configuration is reported, differing in a time-step size of 1·10^{-5} s and 30 internal iterations.

Figure 3.15: Drag coefficient temporal evolution ($\Delta t=1\cdot10^{-5}$ s)

Figure 3.16: Lift coefficient temporal evolution ($\Delta t=1\cdot10^{-5}$ s)

Figure 3.17: Turbulent kinetic energy contour plot ($\Delta t=1\cdot10^{-5}$ s)

From Figure 3.18 to Figure 3.20 the same as for the previous configuration is reported, adopting a time-step size of $5\cdot10^{-6}$ s, 30 internal iterations and a lower simulated flow-time; therefore the contour plot of the turbulent kinetic energy is shown after 0.04318 s.
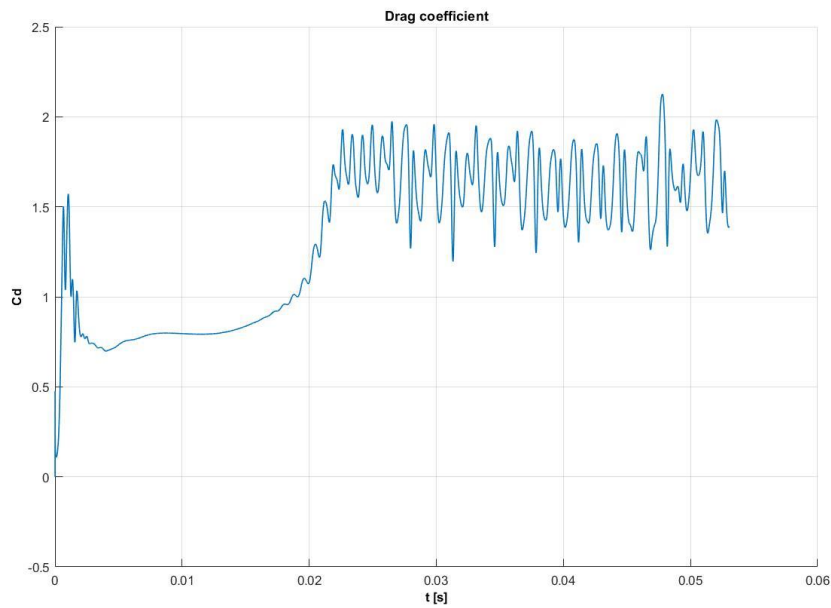

Figure 3.18: Drag coefficient temporal evolution ($\Delta t=5\cdot10^{-6}$ s)
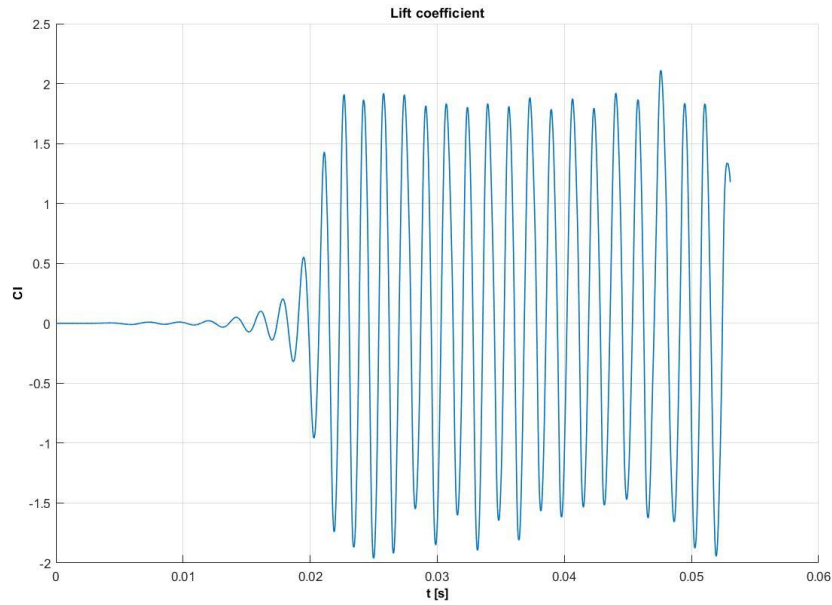
Figure 3.19: Lift coefficient temporal evolution ($\Delta t=5\cdot10^{-6}$ s)
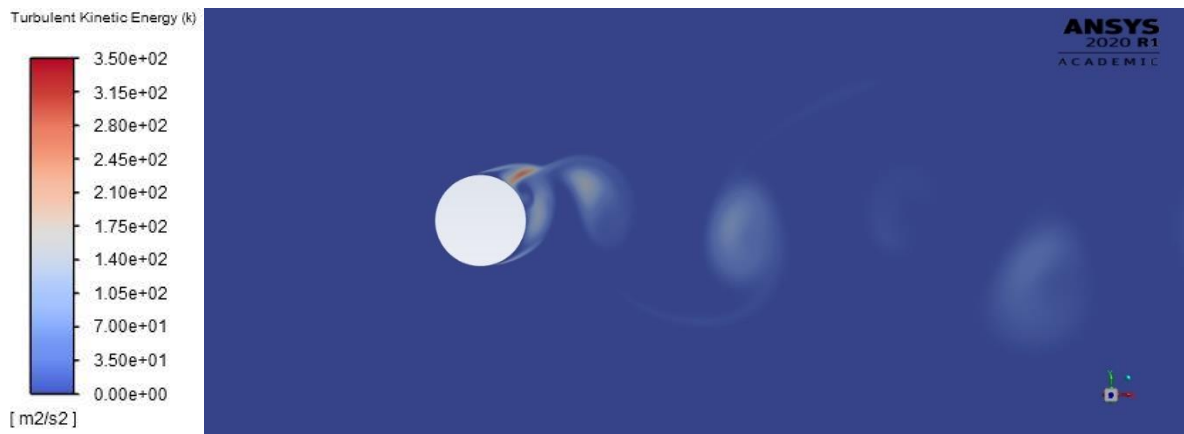

Figure 3.20: Turbulent kinetic energy contour plot ($\Delta t=5\cdot10^{-6}$ s)

From Figure 3.21 to Figure 3.23 the same as for the previous configuration is reported, only differing in a time-step size of $1\cdot10^{-6}$ s, 30 internal iterations and a lower simulated flow-time; therefore the contour plot of the turbulent kinetic energy is shown after 0.0286 s.
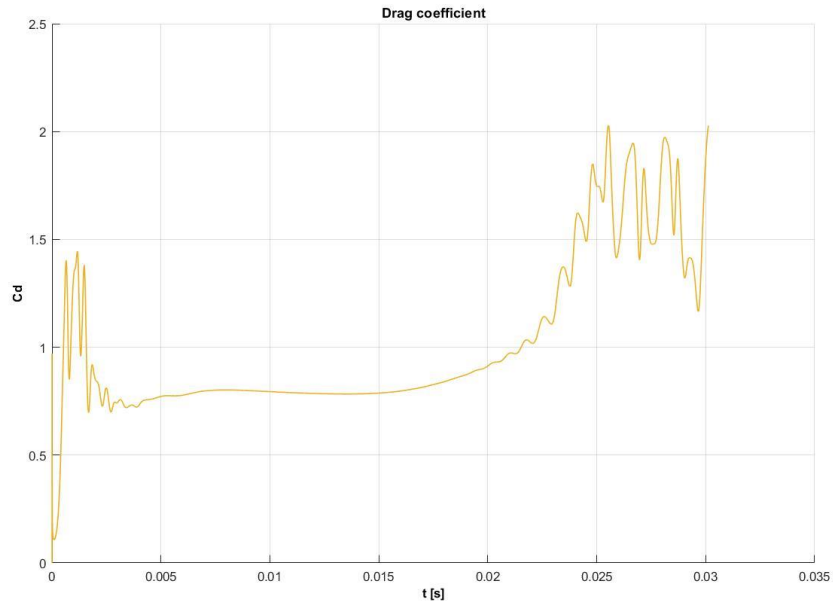
Figure 3.21: Drag coefficient temporal evolution ($\Delta t=1 \cdot 10^{-6}$ s)
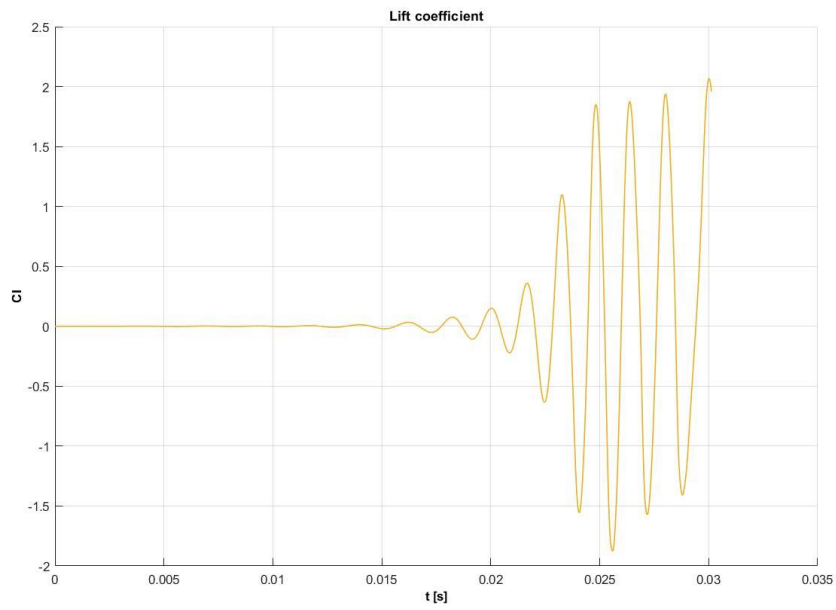

Figure 3.22: Lift coefficient temporal evolution ($\Delta t=1 \cdot 10^{-6}$ s)
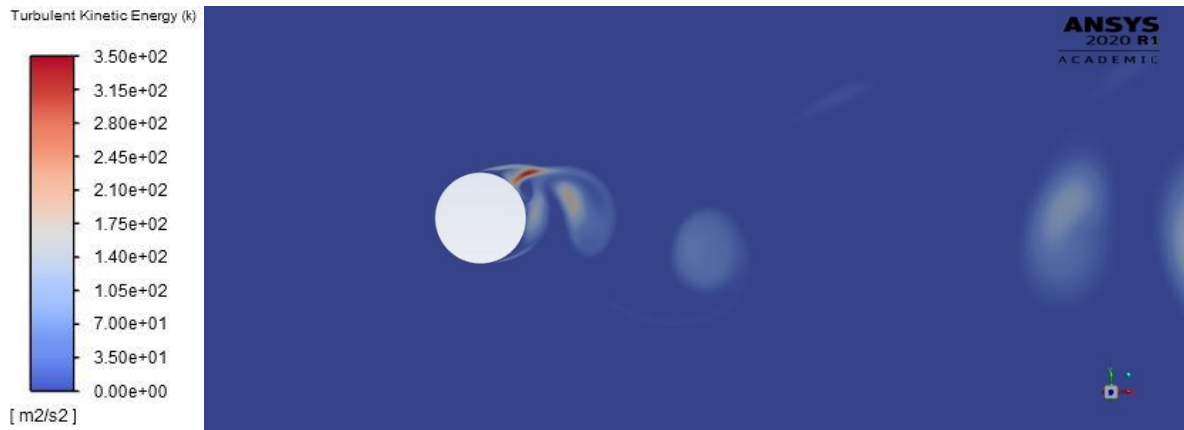
Figure 3.23: Turbulent kinetic energy contour plot ($\Delta t=1\cdot10^{-6}$ s)

It seems clear that by modifying the time-step size, the phenomenology of the vortex street changes remarkably. The same can be said for the temporal evolution of the drag and the lift coefficients, in terms of amplitude and frequency of the oscillations.

Nevertheless, it can be observed that by lowering the time-step size under $1\cdot10^{-5}$ s, the dynamic steady state is more or less the same (in terms of amplitude and frequency of the oscillations of drag and lift coefficients, and also in terms of vortex shedding pattern). Moreover, by taking a look to the monitors inside Fluent, it can be seen that, with a time-step size of $1\cdot10^{-5}$ s and 30 internal iterations, inside each time-step the convergence of the fluid forces is reached and the scaled residual of the continuity equation is reduced to 10^{-5}. These observations lead to the conclusion that to adequately capture the vortex shedding phenomenon in the examined case the maximum allowed time-step size is about $1\cdot10^{-5}$ s.

To verify the last statement, the collected data have been processed into MATLAB®. The *pwelch* function allowed the estimation of the power spectral density of the signal representing the temporal evolution of the lift coefficient.

Using *pwelch* it is possible to obtain the distribution of power spectral density of a given signal as a function of the frequency. Once that the *pwelch* is given the temporal evolution of the lift coefficient, as the input signal, and that consequently the maximum of the computed power spectral density distribution has been taken, it is possible to determine the dominant frequency associated to the lift coefficient temporal evolution. As mentioned in the first chapter, the frequency of the unsteady cross-flow force (i.e. the lift) corresponds to the shedding frequency, therefore it is an essential parameter and it has to be captured with sufficient precision.

The above described procedure was applied to the investigated configurations, skipping the last two because the computed flow-time was not enough to allow a correct implementation of this approach. The results, in terms of frequency and amplitude of the lift coefficient oscillations associated with the different time-step sizes, are shown in Figure 3.24 and Figure 3.25.
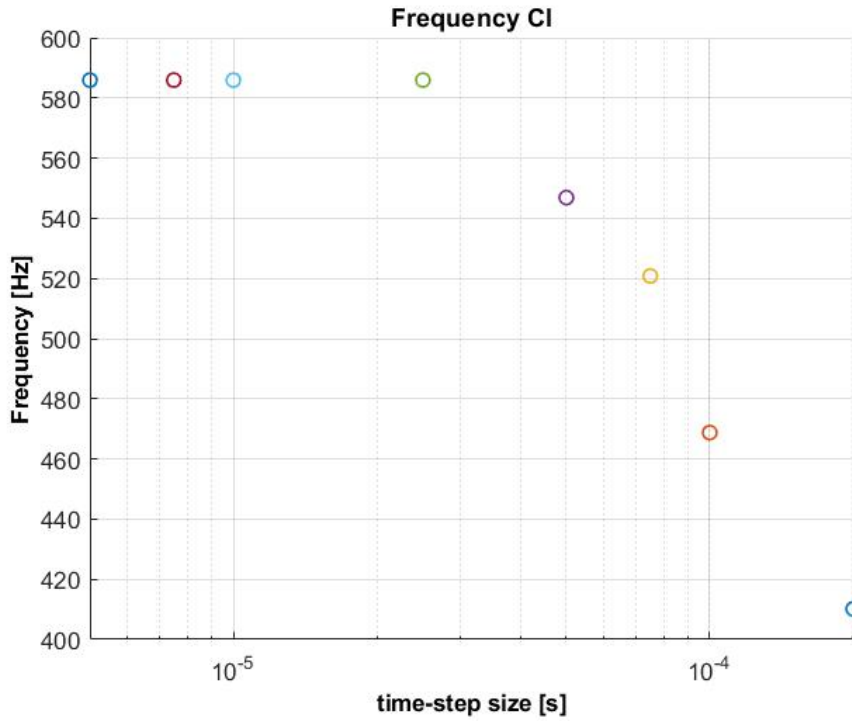
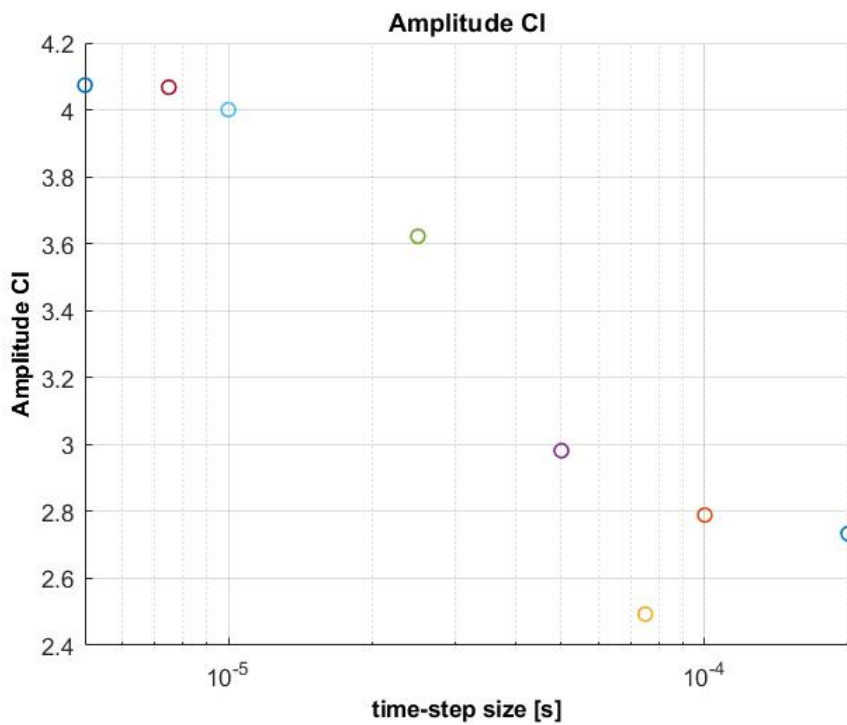**Figure 3.24: Frequency of the lift coefficient**

Figure 3.25: Amplitude of the lift coefficient

It is evident that the above deduced observations regarding the maximum allowed time-step size are confirmed. Moreover it can be observed that, although the last two configurations are not reported, they are not strictly needed, because a time-step size of 10^{-5} s is already sufficient.

At the considered *Re* the expected *St* is about 0.2 (see Figure 1.6), resulting in a vortex shedding frequency of 524.93 Hz (equation 1.2). The obtained value of shedding frequency (for a time-step size of 10^{-5} s or lower) is 585.94 Hz, with an error of -11.62% if compared to the experimental results.

Therefore the obtained results can be considered in a reasonable agreement with the experiments. The presence of some deviation is acceptable and it can be related to different aspects of the presented CFD analysis: a RANS formulation, by definition, will introduce some modeling errors, especially if it is implemented to capture highly unsteady phenomena; a 2-D analysis is not able to fully capture high three-dimensional phenomena like turbulence.

Nevertheless the proposed CFD setup was able to solve with acceptable accuracy the shedding phenomenon both from a qualitative and a quantitative point of view: qualitatively not only the vortex shedding was captured, but it also evolves as expected in the shear layer transition regime (where the simulated *Re* falls); quantitatively the obtained shedding frequency is close to the experimental one.

Hence both the CFD setup and the grid features were considered reliable and applied to the three-dimensional FSI study. Another key result of the 2-D analysis to retain during the setup of the 3-D case is the existence of a maximum time-step size capable of adequately capturing the shedding phenomenon.

4 Vortex induced vibration analysis

In this chapter the vortex induced vibrations of the studied thermowell will be analysed through the above introduced high fidelity FSI approach based on RBF structural mode embedding.

At first the experimental investigation of the considered industrial problem will be presented. Then the geometry of the system under examination will be extrapolated. Starting from the CAD model, the thermowell will be extracted and its modal analysis will be performed. The results of the modal analysis, after a comparison with the analytical ones, will be used to setup the RBF solutions of the modal shapes through a two-step technique. The test of those solutions will point out the necessity of appropriately designed corrective solutions, that will be built and checked. Subsequently the setup for the three-dimensional computational grid generation and for the CFD solution will be described. Afterwards the setup of the FSI calculation will be detailed and the numerical results will be reported. As a part of the numerical results, a parametric study carried out to fine-tune the value of the damping ratio will be exposed.

4.1 *Experimental investigation*

The investigated industrial problem is about the vortex induced vibration of a thermowell immersed in a fluid flow. The case study taken as a reference is presented in a video loaded on the website of Emerson Electric Co. [25], the multinational corporation that owns Rosemount Inc., the manufacturer of the studied thermowell. The above mentioned video was used to gather the input data needed to setup the numerical analysis and the reference experimental results.

The aim of the experiment, whose setup will be detailed in the following, was to evaluate the flow induced vibrations of two possible thermowell designs: the traditional one (cylindrical, shown in Figure 4.1) and the twisted square one (shown in Figure 4.2).

Figure 4.1: Cylindrical thermowell

Figure 4.2: Twisted square thermowell

The two tested thermowells, both with 470.219 mm in length, were equipped with accelerometers in the tip and immersed in a water flow loop evolving inside a 152.4 mm diameter pipe. To evaluate the flow induced vibrations of the two thermowells, the water velocity ranged from 0 m/s to 8.5 m/s. The resulting setup is shown in Figure 4.3.
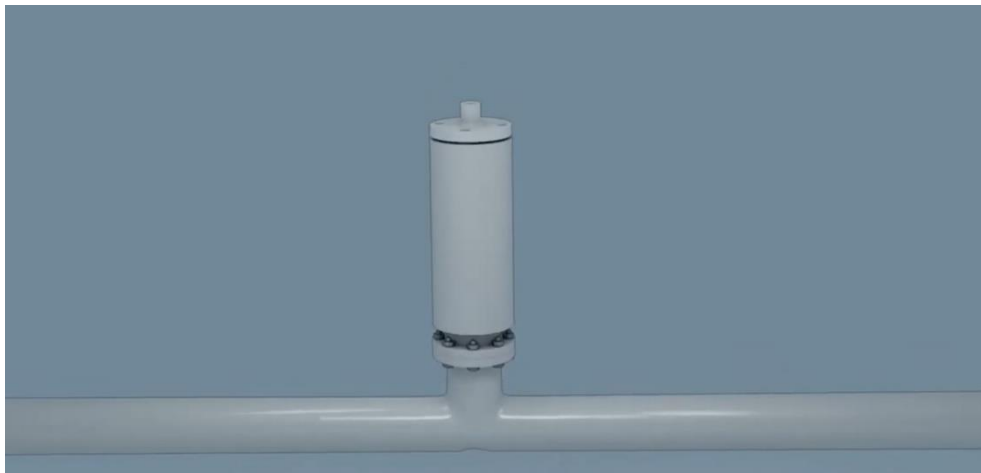

Figure 4.3: Experimental setup

The accelerometer allowed the reconstruction of the evolution of the tip displacement. The gathered results are summarized in Figure 4.4, in terms of the root mean square of the tip displacement as a function of the fluid velocity for the two designs. The higher curve corresponds to the traditional design, whereas the lower one corresponds to the twisted square design.
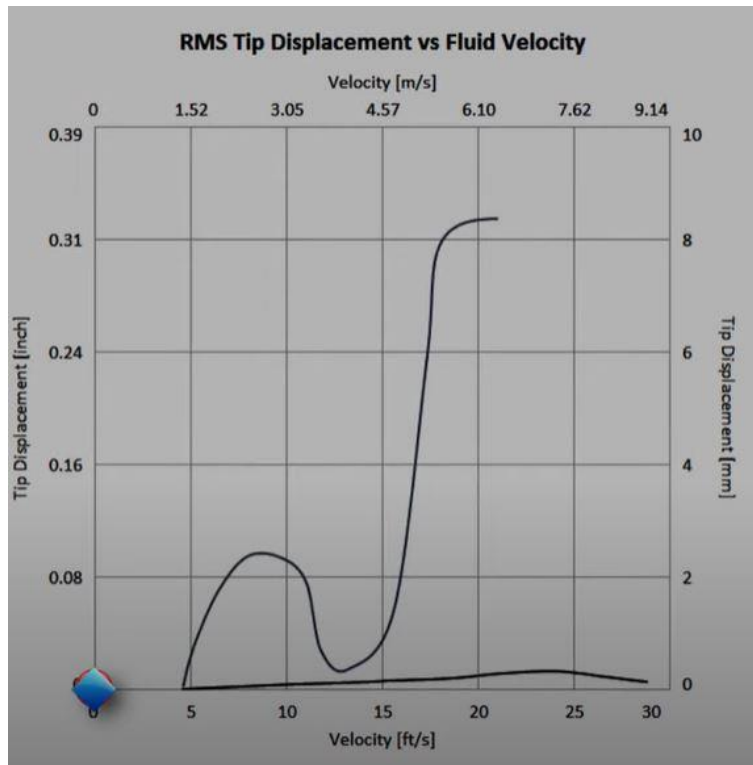
Figure 4.4: Experimental results, RMS tip displacement vs fluid velocity

As far as the traditional thermowell is concerned, the existence of two lock-in regions can be observed: an in-line vibration lock-in region and a transverse vibration lock-in region. In the in-line vibration lock-in region the maximum root mean square tip displacement in the streamwise direction is 2.33 mm, registered with a 2.44 m/s fluid velocity. In the transverse vibration lock-in region the maximum root mean square tip displacement in the cross-flow direction is 8.3 mm, registered with a 6.4 m/s fluid velocity. Exceeded the 6.4 m/s fluid velocity the thermowell broke down.

What just stated is due to the circular cross-section of the thermowell, which allows organized vortices to shed in sheets along the axial length of the stem, as depicted in Figure 4.5. The uniform pressure from the vortices applies alternating forces on the thermowell that are magnified by the VIV (if the shedding frequency approaches a natural frequency of the thermowell or its half, generating the transverse or the in-line vibrations respectively) and eventually lead to the failure.
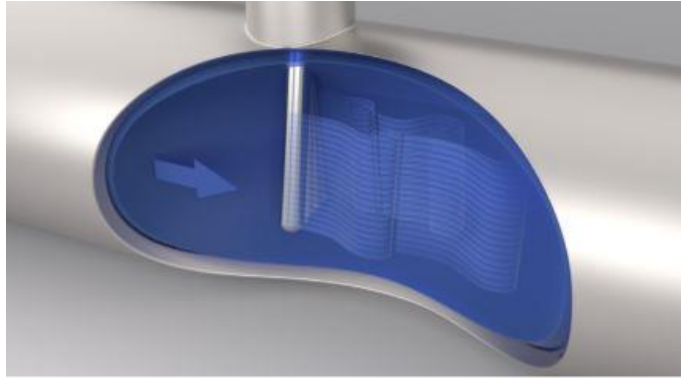
Figure 4.5: Shed vortices, cylindrical thermowell

As far as the twisted square thermowell is concerned, no lock-in regions were found in the tested velocity range, indeed the tip motion amplitude remained at extremely low values throughout all the experiment.

What just mentioned is due to the twisted square's sharp edges and helical profile which provides continuously changing separation points for vortex shedding along the axial length of the stem, as depicted in Figure 4.6. Accordingly, the vortices are forced out of phase, preventing them from becoming synchronized along the span, thus eliminating the VIV.
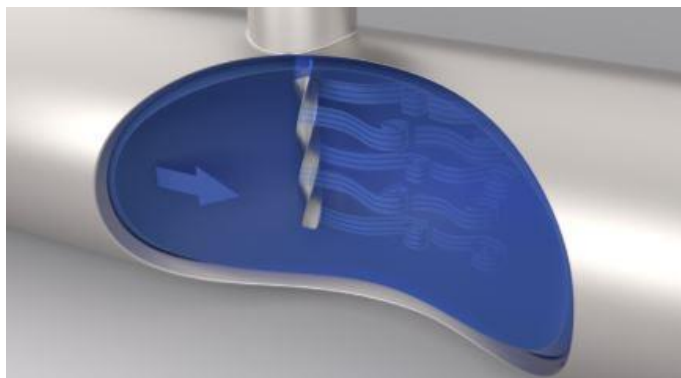

Figure 4.6: Shed vortices, twisted square thermowell

The aim of this thesis is to capture the transverse vibration lock-in region of the cylindrical thermowell numerically.

4.2 *Geometry*

Relying on the above cited video it was possible to determine the geometry of the test setup: it consists of a 152.4 mm diameter pipe, with a 50.8 mm diameter aperture which houses a 470.219 mm long, 16.764 mm diameter cylindrical thermowell. The exposed length of the thermowell is about 143 mm.

In the experimental setup a flow loop was used, with the result that the extent of the computational domain, in terms of simulated length of the pipe, had to be assumed. To guarantee the development of the proper velocity profile in the duct, this one was extended for 412 mm before the thermowell; to leave enough space for the

generation and the evolution of the wake, it was extended for 723.32 mm behind the thermowell. It has to be observed that those dimensions correspond to the ones of the 2-D geometry, as they were able to generate reliable results.

The resulting geometry is shown in a planar view in Figure 4.7, with the dimensions in millimetres, and in an isometric view in Figure 4.8.
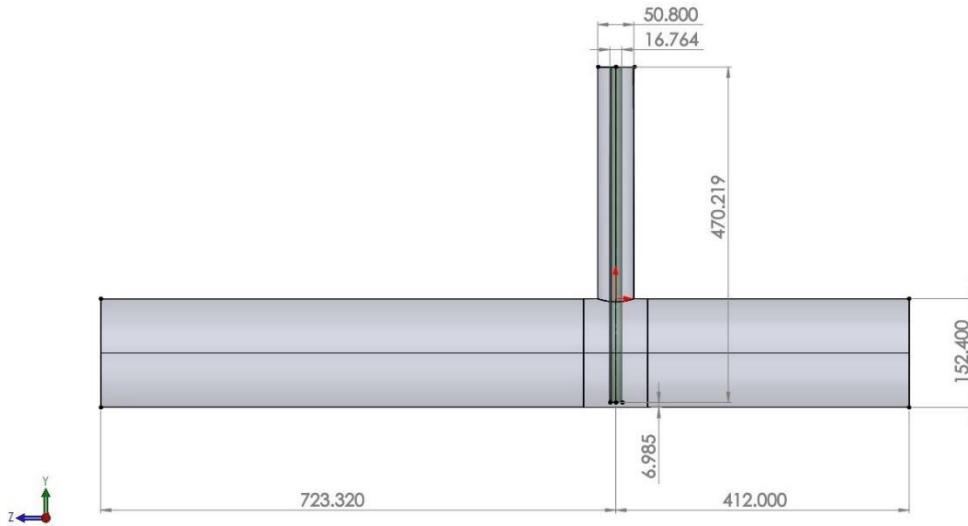
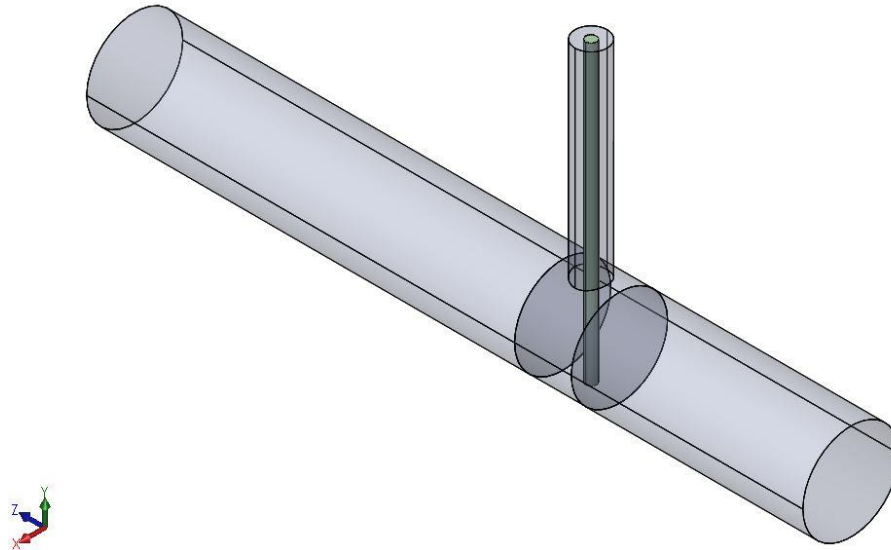**Figure 4.7: Planar view of the analysed system**

Figure 4.8: Isometric view of the system

4.3 *Modal analysis*

The first step needed to setup an FSI analysis based on the modal superposition method is to carry out a modal analysis of the deformable structure. In the presented study, the deformable structure is the thermowell, therefore this latter was extracted from the previously built geometry and imported in ANSYS Mechanical.

From the product data sheet of the thermowells produced by Rosemount [26], it can be seen that the most used material is a 304/304L dual rated steel with a density of 7750 kg/m^3, a Young's modulus of 200 GPa and a Poisson's ratio of 0.3 [27].

4.3.1 FEM model setup

In structural dynamics the general rule of thumb in the discretization process states that the mesh has to correctly represent the distribution of mass and stiffness of the analysed component. Therefore, the implementation of uniform meshes with an adequate sizing to capture the requested modes is typically suggested.

Hence an element size of 2 mm was imposed and the other options were left as by default in the meshing setup. The obtained FEM model, composed of 34456 20-noded hexahedrons for a total of 148675 nodes, is shown in two views in Figure 4.9 and Figure 4.10. As expected, without additional controls the obtained mesh is quite uniform.
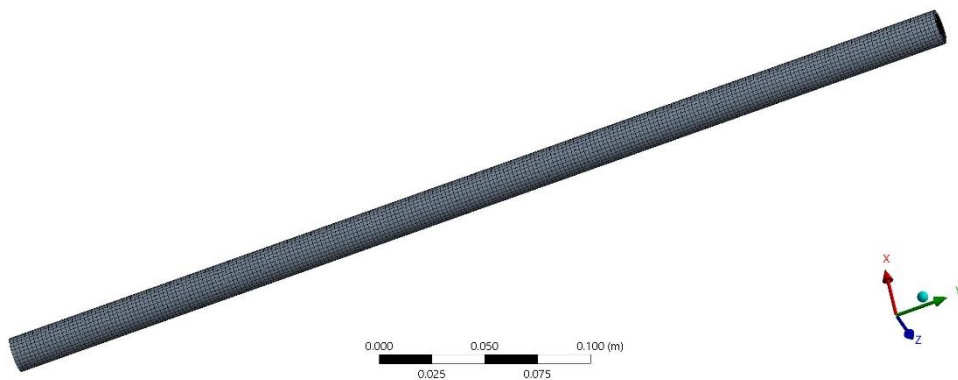

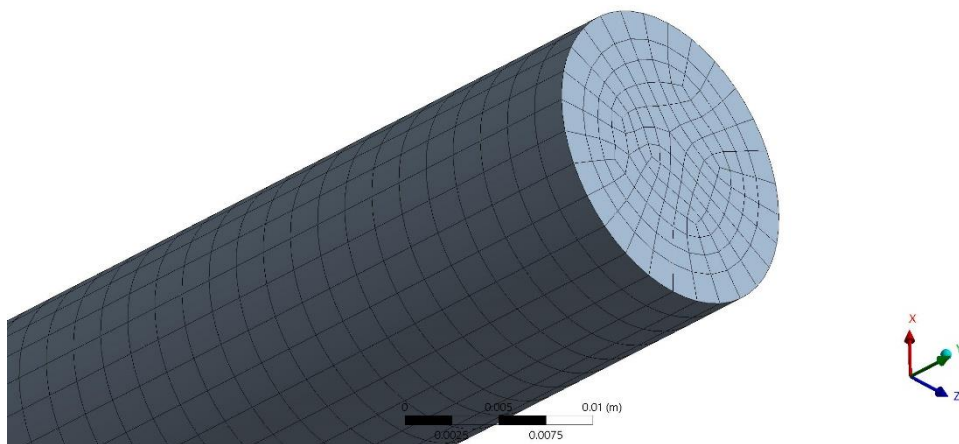**Figure 4.9: FEM model, first view**

Figure 4.10: FEM model, second view

As far as materials properties are concerned the above cited values were employed.

Relating to boundary conditions, the thermowell was considered as a cantilever beam, as in the experimental framework it was flanged and the flange was screwed to the duct; therefore a fixed support condition was assigned to the top of the thermowell and the base was left free to move.

Neither damping nor pre-stress were applied. The choice to not include the damping at this stage was due to the fact that it is already taken into account in the equation 2.48 through the damping ratio ς.

The first twelve modes were extracted, even though only the first six were employed for the FSI study.

4.3.2 Modal analysis results

At first, a mesh convergence study to determine the right sizing for the elements was developed, in order to bring the discretization error down to a neglectable value. The chosen mesh sizing had to fulfil some requirements: the observed values, i.e. the frequencies of the first six modes, had to satisfy the mesh convergence criterion (i.e. a further mesh refinement does not change the obtained results by a considerable amount); due to the perfect symmetry of the circular cross-section, bending modes had to present an algebraic multiplicity of two; the obtained results had to agree with the analytical ones.

The investigated element sizes and the associated number of nodes are shown in Table 4.1.

Element size [m]	Number of nodes
0.01	3070
0.008	4659
0.007	5086
0.005	8520
0.004	17810
0.003	31074
0.002	148675
0.0015	259664

Table 4.1: FEM model investigated element sizes

The results of the mesh convergence study are shown in Table 4.2 and from Figure 4.11 to Figure 4.13.

Number of nodes	Mode 1 frequency [Hz]	Mode 2 frequency [Hz]	Mode 3 frequency [Hz]	Mode 4 frequency [Hz]	Mode 5 frequency [Hz]	Mode 6 frequency [Hz]
3070	53.905	53.940	336.386	336.603	936.172	935.579
4659	53.924	53.939	336.497	336.591	936.142	935.880
5086	53.921	53.948	336.481	336.651	936.302	935.839
8520	53.927	53.930	336.517	336.533	935.972	935.927
17810	53.926	53.931	336.510	336.539	935.986	935.906
31074	53.927	53.928	336.514	336.521	935.934	935.915
148675	53.925	53.925	336.499	336.499	935.872	935.870
259664	53.923	53.923	336.489	336.489	935.843	935.842

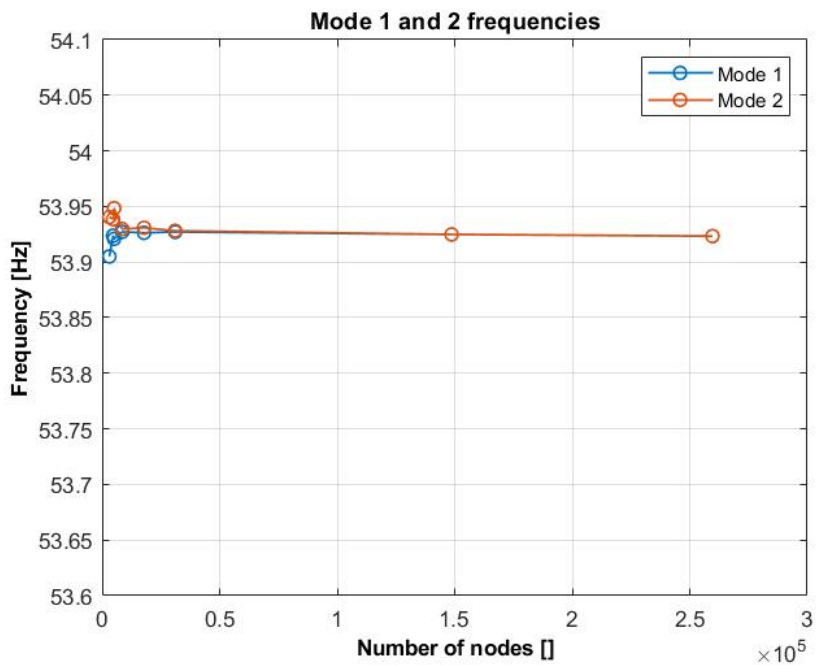**Table 4.2: Mesh convergence study results**

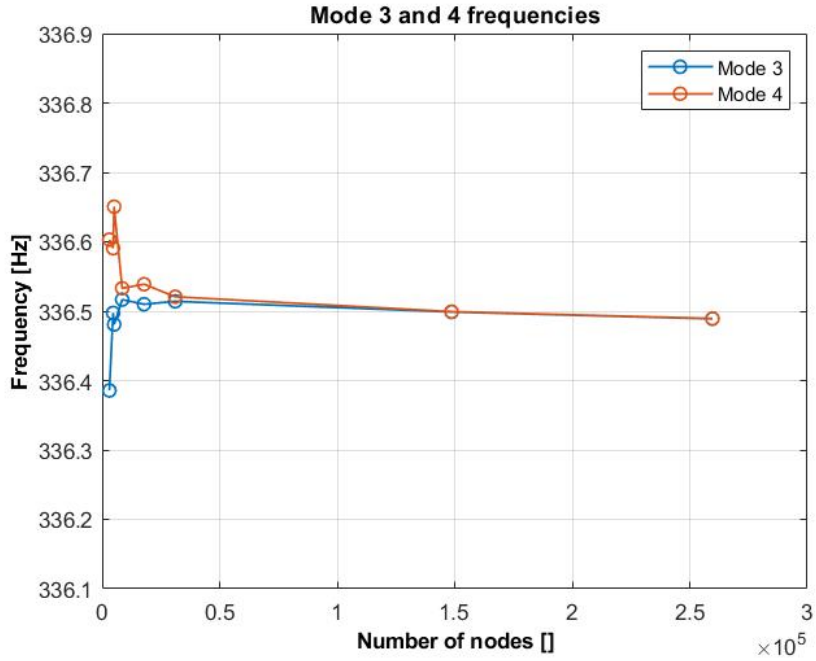**Figure 4.11: Mesh convergence study results, mode 1 and 2**

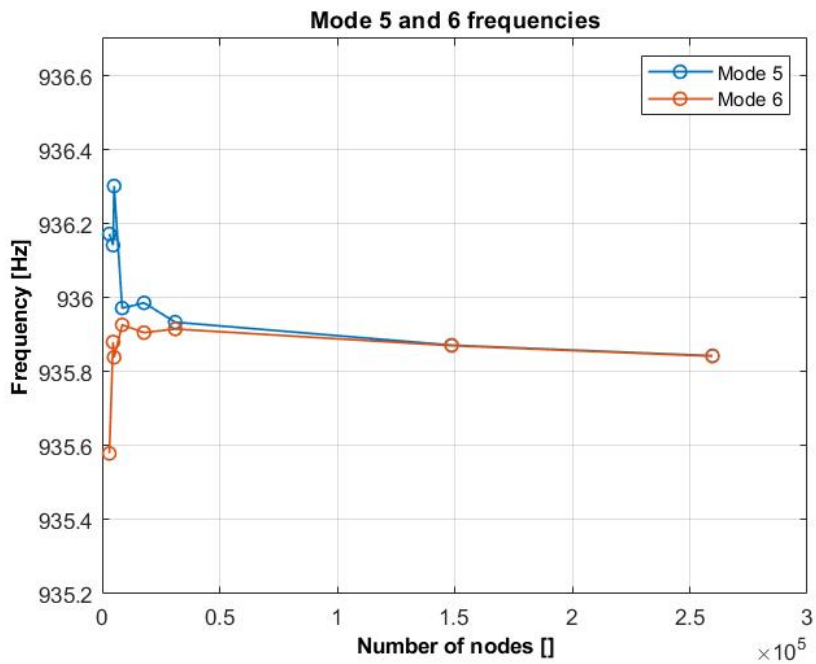**Figure 4.12: Mesh convergence study results, mode 3 and 4**

Figure 4.13: Mesh convergence study results, mode 5 and 6

From the displayed results, it appears clear that the chosen element size of 2 mm satisfies the afore mentioned requirements (the last one will be deepened in the next subsection).

Once ascertained the reliability of the generated mesh, the first six computed natural modal shapes (the ones that will be used in the FSI analysis) are shown from Figure 4.14 to Figure 4.16.
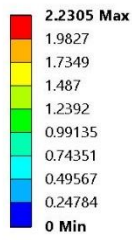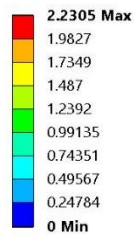
Figure 4.14: First and second modal shapes
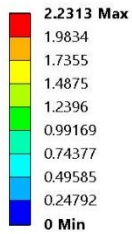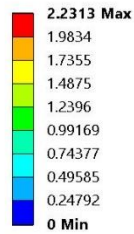
Figure 4.15: Third and fourth modal shapes
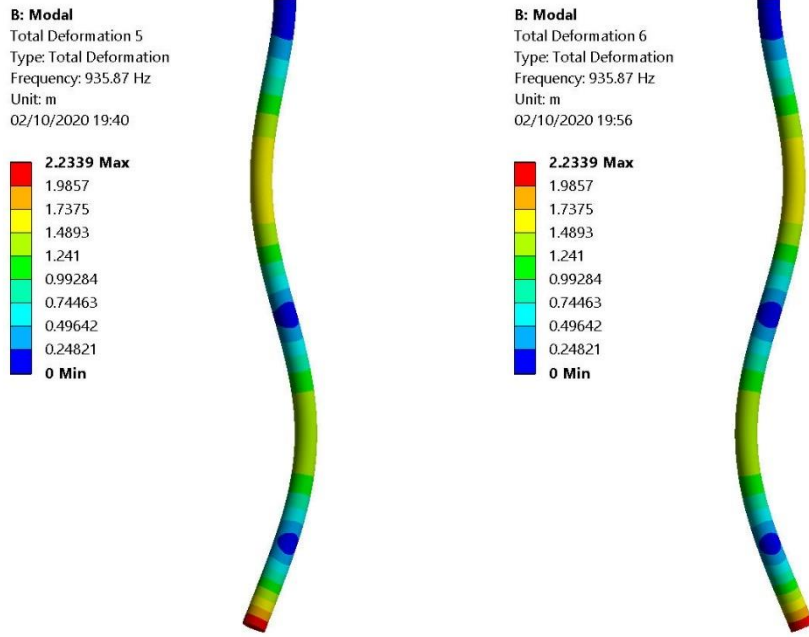
Figure 4.16: Fifth and sixth modal shapes

It has to be specified that the modal shapes are mass normalized, but in order to simplify the visualization the deformations have been scaled down with a factor of $1.2 \cdot 10^{-2}$.

It can be observed that the first six computed natural modes correspond to only three distinct bending modes. This result is due to the to the perfect symmetry of the circular cross-section, that causes an algebraic multiplicity of two of the bending modes. Hence each bending mode is associated with two distinct computed modes, the first characterized by an oscillation in the streamwise direction (the odd ones) and the second characterized by an oscillation in the transverse direction (the even ones), both with the same natural frequency (i.e. the frequency of the associated bending mode).

After performing the modal analysis, the nodal displacements of the external surface mesh of the thermowell for each of the six considered modes (mass normalized) were saved in a format readable by the morpher tool. This task was accomplished using the Modal Extraction ACT extension.

The above mentioned readable format for RBF Morph is a .pts file in which a set of source points is reported. To correctly define a source point in the scope of an RBF solution setup, its coordinates (x, y and z) and displacements (in the x, y and z directions) have to be assigned.

In this application the source points are the nodes of the surface mesh, therefore the ACT extension extracts the nodal coordinates of the starting surface mesh, and the nodal displacements associated to the considered modal shape; then it writes these information in the above mentioned format and repeats this process for all the six modes.

Such data were used to setup the RBF solutions reproducing the structural modes to be applied during the CFD calculation through mesh morphing, as will be explained in the following section.

68

4.3.3 Analytical results

As before stated the thermowell can be considered as a cantilever beam, therefore analytical solutions to the eigenvalue problem exist and so it is worth to implement them in order to validate the obtained results. Without diving into details, the first three bending natural frequencies of a cantilever beam can be written as follows (4.1) [21]:

$$\omega_{n,i} = \alpha_i^2 \sqrt{\frac{EI_B}{\rho A_B L_B^4}} \quad i = 1,2,3 \tag{4.1}$$

Where: E is the Young's Modulus of the material of which the beam is made; I_B is the moment of inertia of the beam cross-section (for a circular cross-section it is given as $I_B = \frac{\pi}{64} D^4$); ρ is the density of the material of which the beam is made; A_B is the area of the beam cross-section (for a circular cross-section it is given as $A_B = \frac{\pi}{4} D^2$); L_B is the length of the beam; α_i is a constant descending from the resolution of the eigenvalue problem and its value depends on the boundary conditions of the considered beam and on the selected natural mode.

For a cantilever beam, the first three constants corresponding to the first three natural modes are 1.8751, 4.6941 and 7.8548. The resulting frequencies and the relative errors of the ones computed with the FEM analysis are shown in Table 4.3 (it has to be specified that each mode has an algebraic multiplicity of two, but only one is reported).

Mode	Analytical natural frequency [Hz]	FEM natural frequency [Hz]	Relative error [%]
1	53.883	53.925	-0.0779
2	337.681	336.499	0.34999
3	945.523	935.872	1.0207

Table 4.3: Natural frequencies, analytical results

From the resolution of the eigenvalue problem, it is possible to derive also the shapes of the first three natural modes for a cantilever beam. They are shown in Figure 4.17 [21].
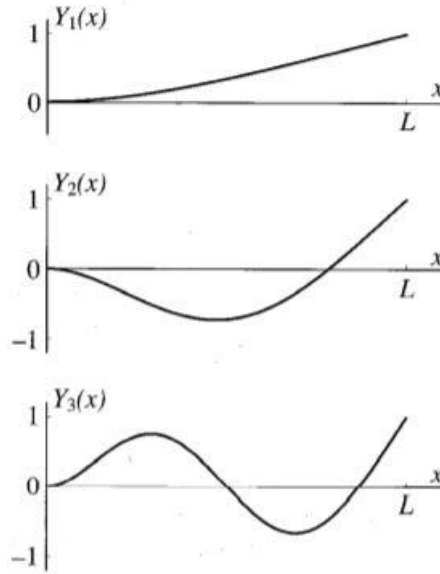
Figure 4.17: First three modal shapes

A good agreement between the analytical and the FEM results, in terms of both the natural frequencies values and the modal shapes, can be clearly observed. On account of what just stated the modal analysis results were considered reliable.

4.4 RBF solutions setup

The basic steps that are typically needed to set up an RBF solution foresee the assignment of the source points displacement and the definition of a delimiting volume (i.e. a domain) to restrict the action of morphing.

In order to generate the RBF solution for each natural mode of the thermowell, a two-step technique was employed [28]. The first step loads the previously generated .pts file corresponding to the considered modal shape. In the second step the first RBF solution is imposed as a motion law to the thermowell surface and a domain encapsulation is introduced to delimit the action of the morphing. The second step aims to finalize the surface morphing and to set the RBF solution for volume mesh smoothing.

In addition to that, a set of corrective RBF solutions had to be employed. To reduce the volume mesh distortion, a shadow area management made up of a translation and a rotation was needed; to recover the cylindricity of the duct, lost by reason of the rotation imposed to the shadow area, an STL-target solution was implemented.

A description of all the employed RBF solutions will be exposed in this section.

4.4.1 First step of the two-step technique

The purpose of the first of the two-step approach is to define a wanted displacement to the surface mesh nodes so that the final position of the surface is not influenced by the remaining set-up of the whole RBF solution.

This task is accomplished importing the source points from the previously generated .pts files into the morpher tool.

The obtained result (related to the odd modes, as the even ones are symmetrical) is shown from Figure 4.18 to Figure 4.20. The red points are the source points in their starting position, whereas the green ones are the source points in their final position, after the assigned displacement.
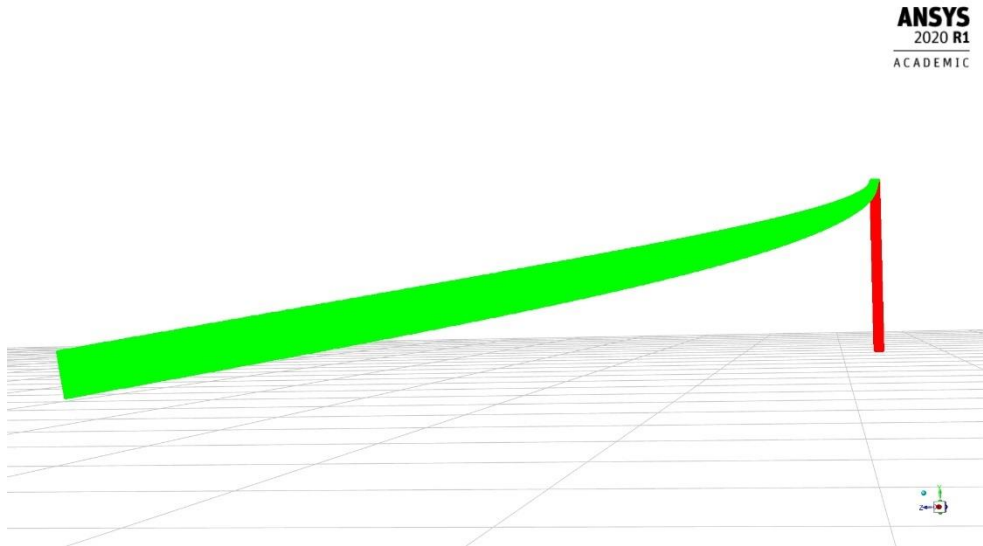

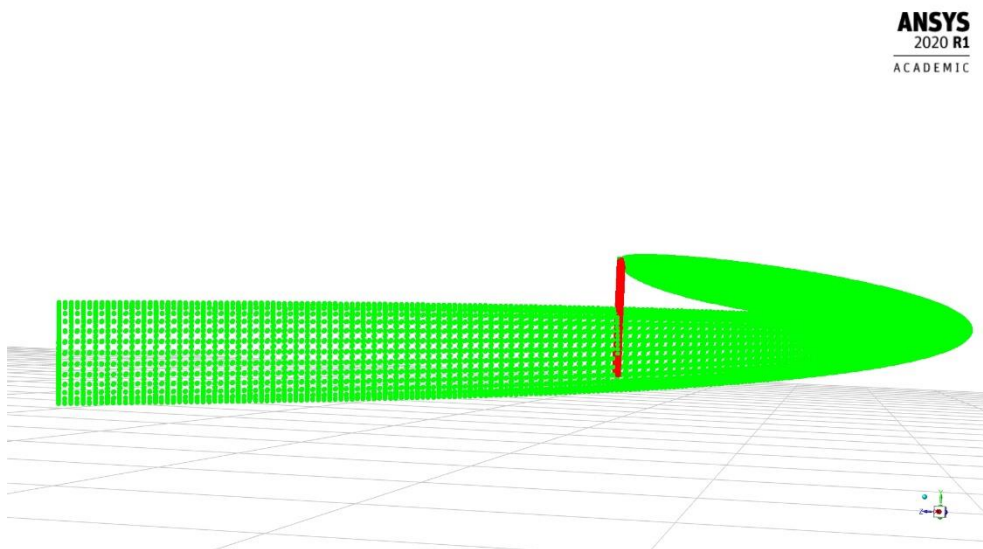**Figure 4.18: First step applied to the first mode**

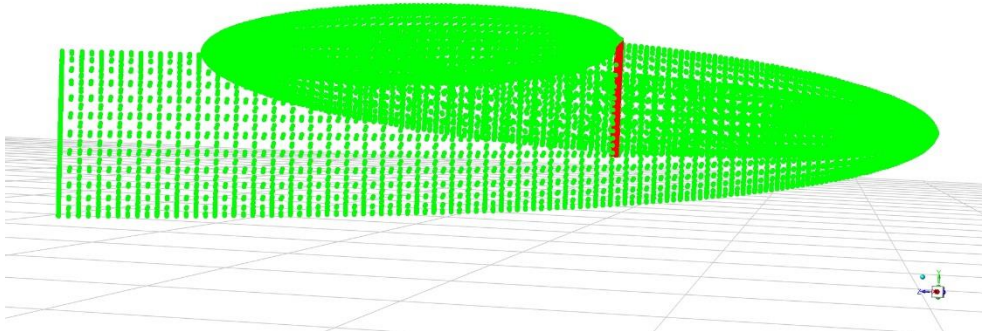**Figure 4.19: First step applied to the third mode**

Figure 4.20: First step applied to the fifth mode

It seems clear that the modal shapes are correctly imported into the morpher, but their amplitude is excessive due to the normalization with respect to the mass. The high amplitude of the modal shapes causes problems during the morphing actions that take place as the FSI computation proceeds. Basically it generates highly distorted cells (that provoke convergence problems within a time-step) and even negative volume ones (that force the calculation to stop). The solution to this problem is implemented in the second step of the two-step procedure and will be explained in the next subsection.

Being the only purpose of the first step to accurately control the surface mesh displacements, no further conditions were imposed.

As far as solver settings are concerned: the Gaussian was the selected RBF, because it has the best performance in terms of computing and guarantees the best quality for the volume mesh; the LCM distance was set to zero, thus the sub-sampling was disabled.

The local correction method (LCM) distance is a sub-sampling spacing used by the solver to reduce the total number of source points. It operates as a sub-sampling but without losing the accuracy of the surfaces, within the solver tolerance. The idea is that once the solution of the RBF problem is performed, some residual error remains at the source points excluded by the sub-sampling; therefore the solver reintroduces some of excluded source points to reduce the error under the solver tolerance (i.e. another solver parameter that defines the order of magnitude of the absolute error which can be found on nodal positions). This process is repeated for a set number of times, defined by the number of refinement steps (another solver parameter). Nevertheless, after the refinement process a residual error still persists and it is removed in the correction stage building-up several local RBF problems, one for each retained point.

It appears clear that the LCM distance is a fundamental solver parameter, as it determines: the size of the RBF problem, the size of the refinement problem, the number and the size of the correction problems. If a low value is used the RBF problem and the refinement problem will be large, whereas the correction stage will be

performed on several small local problems. If a large value is used, the RBF and refinement problems will be small and the correction stage will be large.

In the first step of the two-step procedure, the number of source points was 21293, making the RBF problem not too large and allowing the disabling of the sub-sampling process.

After the resolution of the six RBF problems associated with the six selected natural modes, their solution files are available and will be implemented in the setup of the second step.

4.4.2 Second step of the two-step technique

In the second stage of the two-step technique the RBF solution of the first step is imposed as the motion law to the deformable surfaces and the RBF solution for volume mesh smoothing is set. The setup of the second stage, the same for every mode, will be explained in the following.

A box-shaped domain encapsulation (shown in Figure 4.21) was introduced, in order to delimit the action of the morphing and therefore lowering the time needed to apply it.
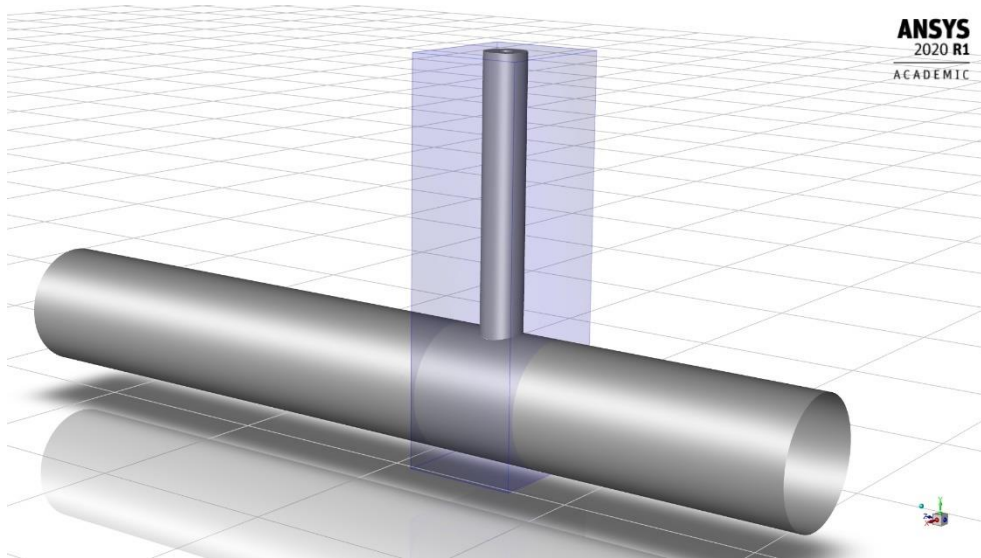

Figure 4.21: Second step domain encapsulation

The inlet, the outlet and the wall surfaces were fixed imposing a null motion to them; whereas the motion law imposed to the thermowell surface was the RBF solution obtained through the first step but amplified with a factor of 0.001.

The 0.001 amplification factor allowed the resolution of the previously mentioned problem, reducing the amplitude of the modal shapes and, therefore, improving the morphing quality. However it has to be considered that the equation 2.48 is derived assuming that the modal shapes are mass normalized and that, by introducing that amplification factor, this hypothesis falls short. This aspect causes further complications, because the modal forces (obtained projecting the nodal forces onto the modal shapes) will be reduced by a factor of 1000

and the mesh movements will have to be applied multiplying the modal coordinates by a factor of 1000. The measures able to solve these issues have been introduced into the function (inside Fluent) that implements the process needed to calculate the modal coordinates starting from the fluid forces and they will be explained later.

As far as solver settings are concerned: the Gaussian was the selected RBF, because it has the best performance in terms of computing and guarantees the best quality for the volume mesh; the LCM distance was set to 0.001 m; the number of refinement steps was set to 4 and the solver tolerance was set to 10^{-6}.

In this instance the number of source points was 76970, therefore the sub-sampling was needed and the other mentioned solver parameters had to be assigned. The value of the LCM distance, the number of refinement steps and the solver tolerance were the result of a trial and error process that aimed to identify a solver configuration capable of ensuring a good morphing quality and a reasonable solving time for the RBF problem. The sub-sampling allowed the reduction of the number of source points to about 42000 for all the six modes.

The result of this setup is shown with regard to the first mode (but the other five are similar), in Figure 4.22 and Figure 4.23, with the same colouring for the source points as before.
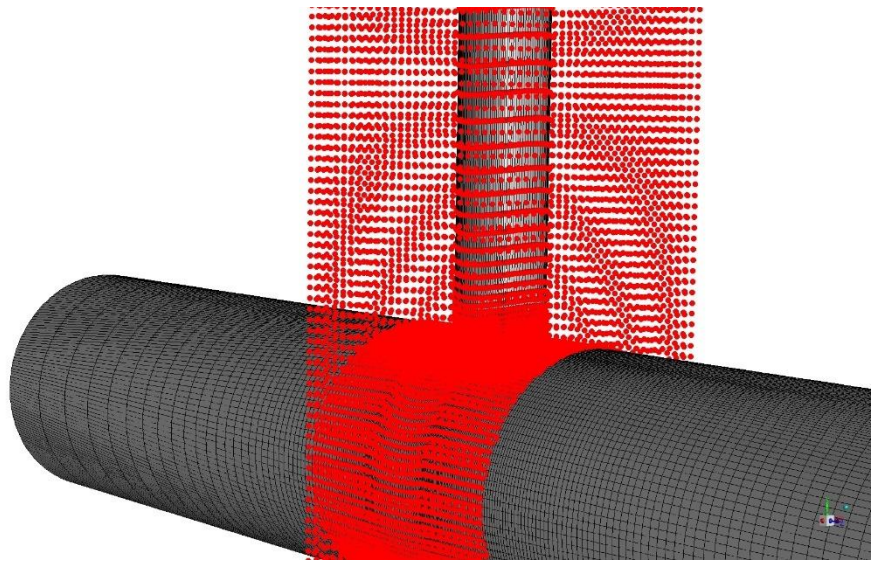

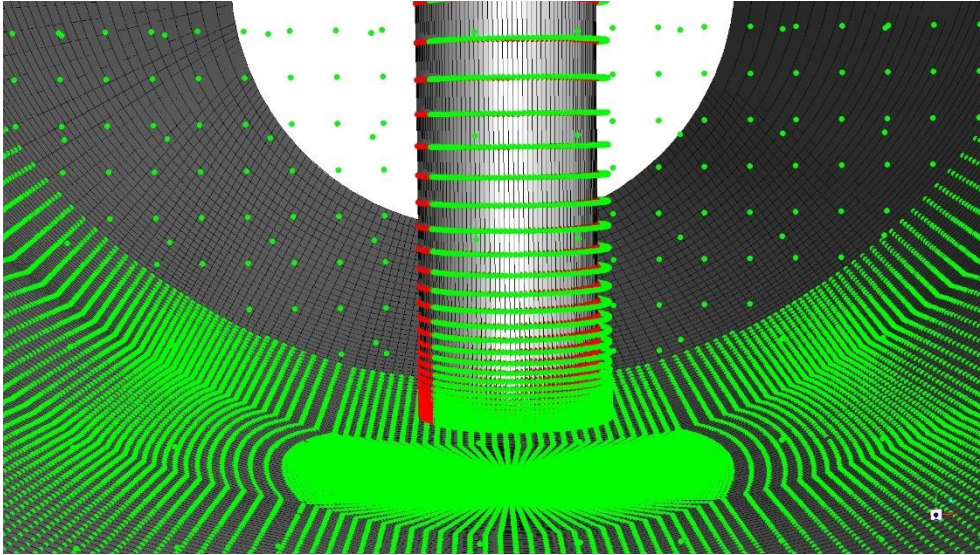**Figure 4.22: Second step applied to the first mode**

Figure 4.23: Second step applied to the first mode, detail around the thermowell

It can be clearly claimed that the above described setup was implemented as expected, consequently the six RBF solutions associated with the six modes were created.

4.4.3   The need for corrective RBF solutions

The proximity of the tip of the thermowell to the boundary of the simulation volume (i.e. the wall of the pipe) caused a challenging problem. In fact combining this proximity to the large displacements that the thermowell was expected to experience due to the vortex induced vibrations, the volume mesh elements would be highly distorted as a consequence of the exposed morphing setup, by reason of the null motion imposed to the duct wall.

It has to be observed that the imposition of the null motion to the nodes on the duct wall was a necessity, because otherwise (without a direct control of the duct surface obtained through the employment of source points on it) the cylindricity of the wall would have been lost.

The starting (undeformed) volume mesh around the tip of the thermowell is shown in Figure 4.24 (obtained through a vertical cutting plane), whereas in Figure 4.25 the volume mesh is shown with an imposed set of modal coordinates that causes a tip displacement of 1.9 mm in the streamwise direction and 7 mm in the transverse direction (corresponding to the maximum obtainable deformation, without corrective RBF solutions and with the wall nodes fixed, before getting divergence in the CFD solver).
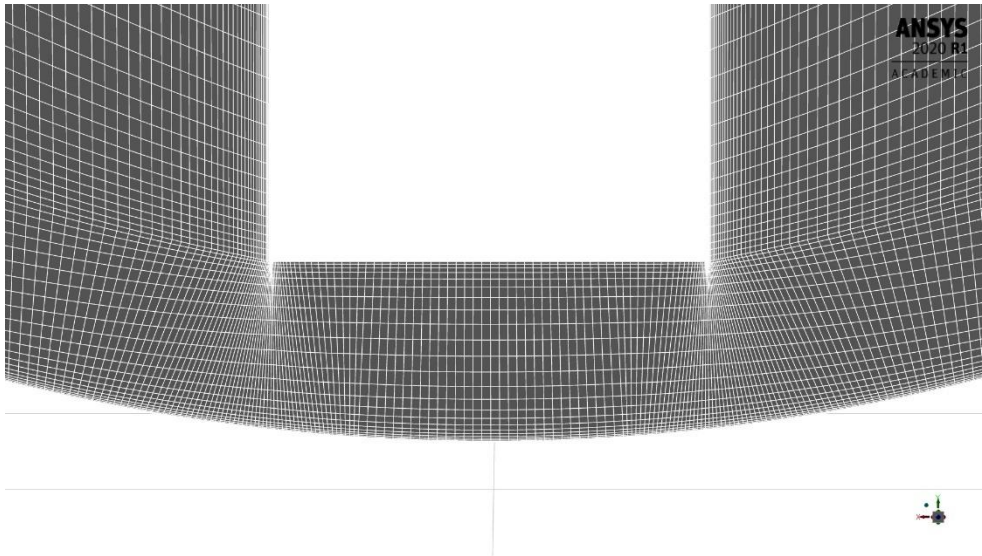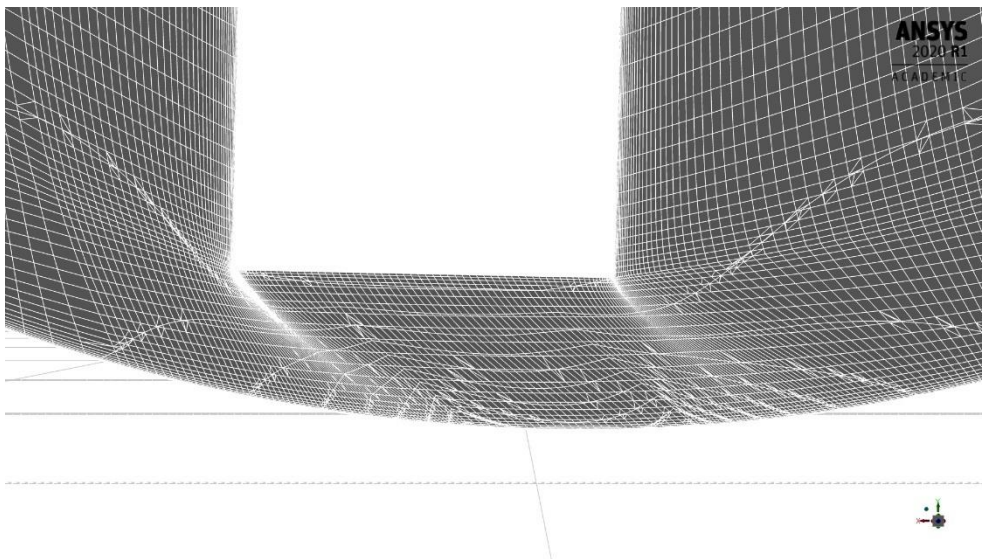
Figure 4.24: Starting mesh around the tip

Figure 4.25: Deformed mesh around the tip

The high mesh distortion after the morphing is clear. Moreover a mesh quality evaluation was carried out: a minimum orthogonal quality of 0.016 and a maximum cell squish index of 0.984 were reported, both in the worst quality range. Indeed, after reaching deformations of this entity, the CFD solver diverged.

This issue was resolved adopting a set of three corrective RBF solutions.

It appears clear, from Figure 4.25, that the main issue lies in the null motion imposed to the wall nodes, therefore the shadow area management was employed [23]. The shadow area is the portion of the duct surface linked to the tip of the thermowell through the structured mesh (i.e. the projection of the tip on the duct). To avoid the high mesh distortion, the surface nodes contained in this area had to follow the tip of the thermowell during the morphing action. This latter task was accomplished assigning to the shadow area an appropriate rotation around the pipe axis and a translation in the direction of the axis itself, in order to always keep it under the tip.

An additional corrective solution, derived from an STL-target, was needed in order to recover the cylindricity of the duct, lost due to the rotation imposed to the shadow area.

The setup of the mentioned corrective solutions will be explained in the following subsections.

4.4.4 Shadow area management

As for the previous solutions, a box-shaped domain encapsulation (shown in Figure 4.26) was introduced, in order to delimit the action of the morphing.
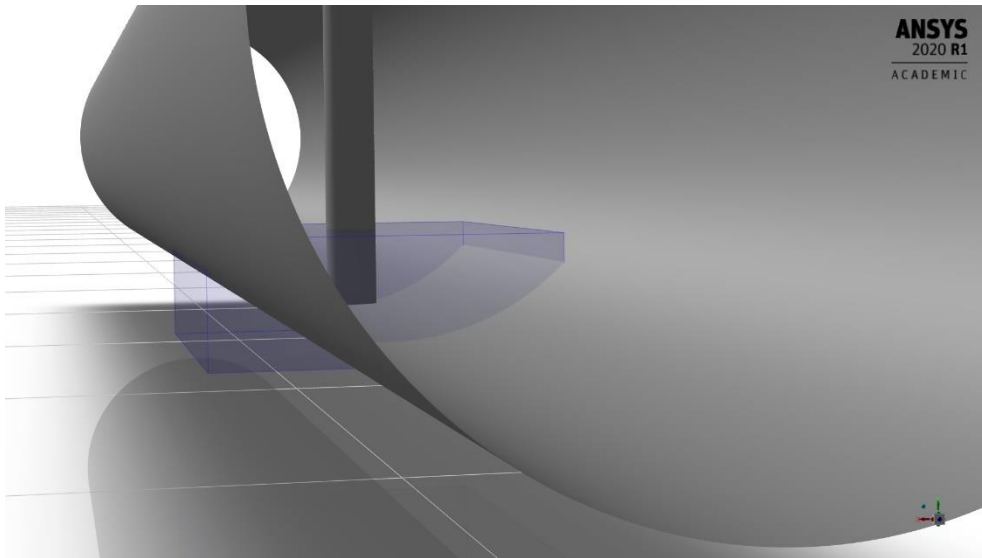

Figure 4.26: Shadow area management domain encapsulation

In order to extract the nodes in the shadow area, a cylinder-shaped selection encapsulation (shown in Figure 4.27) was used.
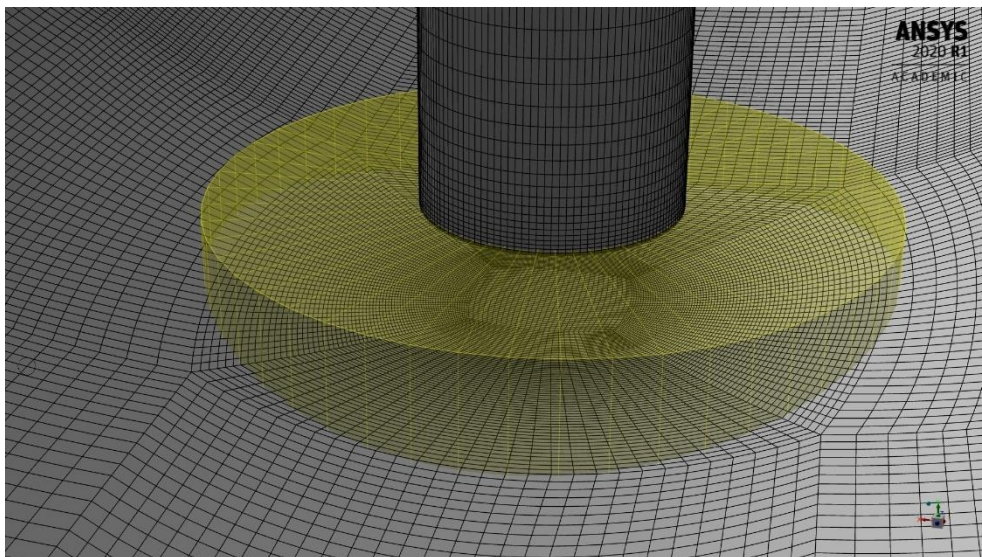

Figure 4.27: Shadow area management selection encapsulation

It has to be specified that the diameter of the selection encapsulation is larger than the one of thermowell, so that a better quality of the morphing is guaranteed when a large displacement is imposed.

As far as assigned motions are concerned, two shadow area management solutions were created: in the first one, a one degree rotation around the pipe axis was imposed to the nodes selected with the encapsulation, whereas in the second one a unitary displacement in the z direction (corresponding to the direction of the pipe axis) was imposed.

A null motion was imposed to the thermowell surface, in order to not interfere with the deformation imposed by the FSI calculation.

A second selection encapsulation was introduced, this time box-shaped, in order to extract a set of buffer nodes (on the duct wall) between the ones moved by the morphing action and the ones fixed due to the proximity with the boundary of the domain encapsulation. This latter set of buffer nodes lies between the selection encapsulation, the yellow one in Figure 4.28, and the domain encapsulation, the blue one.
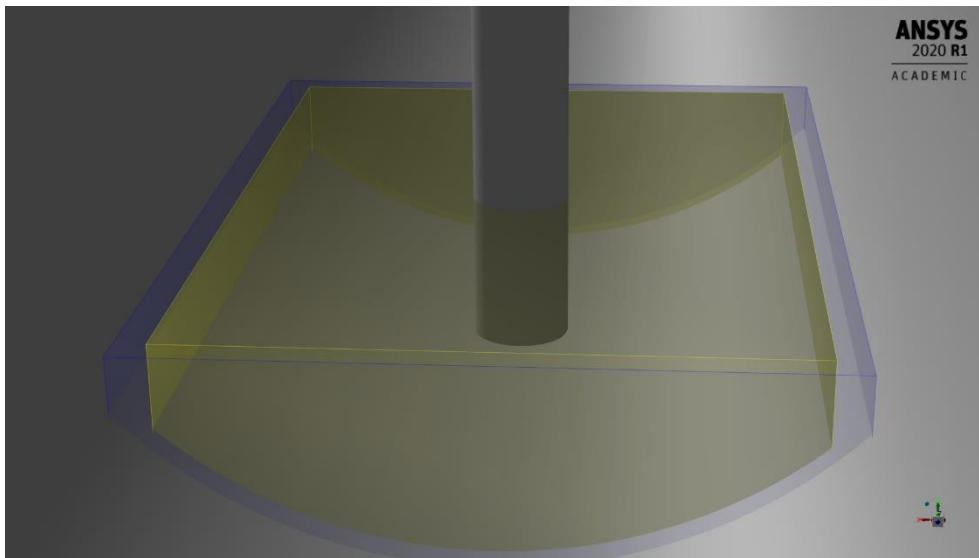
Figure 4.28: Selection of the buffer nodes

A null motion was imposed to those nodes too. The reason for this precaution will be clarified in the next subsection.

As far as solver settings are concerned: the Gaussian was the selected RBF and the LCM distance was set to zero, because the number of source points was 20219, making the RBF problem not too large and allowing the disabling of the sub-sampling process.

The result of this setup with the rotation motion assigned to the shadow area is shown in Figure 4.29, with the same colouring for the source points as before.
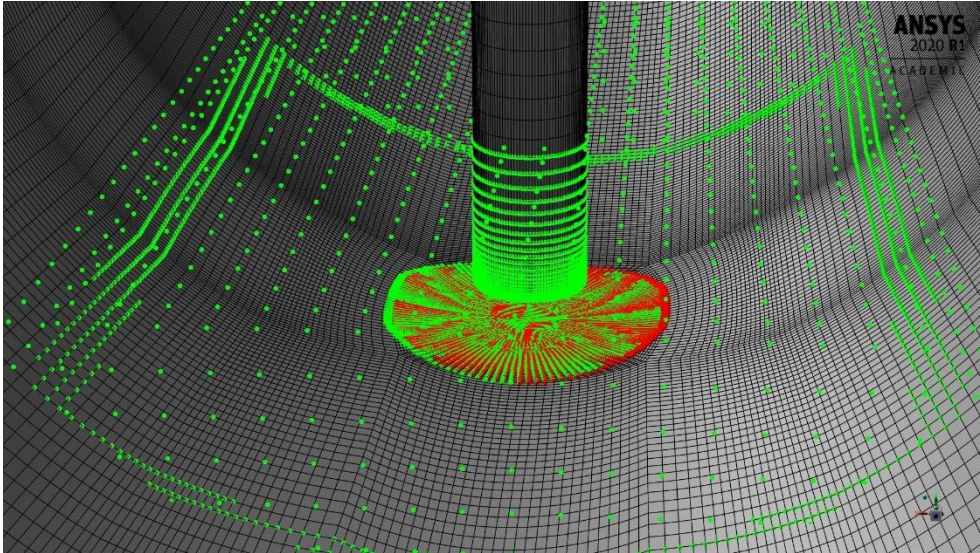
Figure 4.29: Shadow area rotation

It seems clear that the above described setup was implemented as expected, therefore the first two RBF corrective solutions were created.

Although the shadow area rotation was correctly implemented, the absence of source points on the rest of the duct surface caused the loss of direct control on its morphing. This lack of control causes a distortion of the cylindrical surface (i.e. the duct), visible in Figure 4.30 (obtained with a 15° rotation of the shadow area).

Figure 4.30: Cylinder distortion

To solve this issue a third RBF corrective solution, described in the following subsection, had to be implemented.

4.4.5 STL-target-derived corrections

The aim of the last couple of corrections is to solve the issue regarding the duct distortion as a consequence of the shadow area rotation. In order to do so, an RBF solution derived from an STL-target solution was implemented. The approach followed to build such solutions will be described in the following.

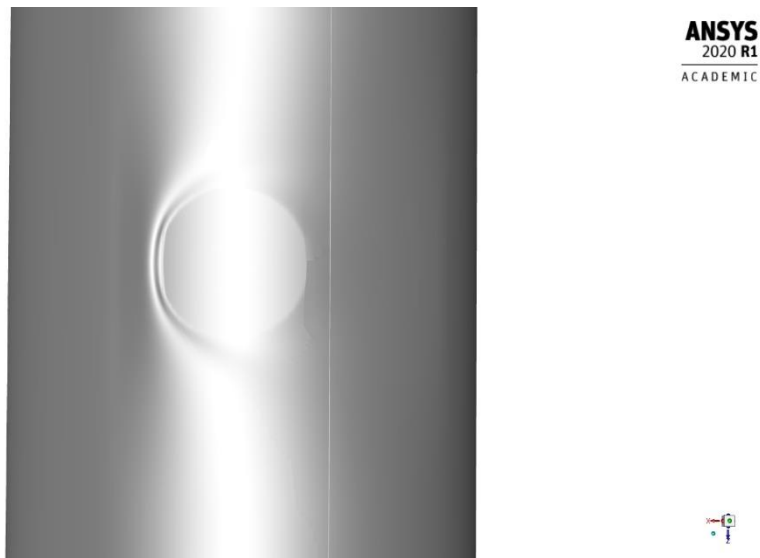The first thing that needs to be done is the choice of a maximum expected rotation of the shadow area during the FSI analysis. From the available experimental results, the maximum expected root mean square of the transverse displacement of the tip is 8.3 mm, corresponding to a 9.6° maximum rotation of the shadow area. To retain a safety factor with respect to this expected value, the chosen maximum rotation was 15° (if a larger rotation occurs, the corrective solution will give wrong results).

This maximum rotation was then applied through an amplification by a factor of 15 of the previously gathered RBF solution. This morphing resulted into the cylinder distortion shown in Figure 4.30.

At this point, on the deformed mesh, the STL-target RBF solution was setup. The domain encapsulation and the selection encapsulation were the same as in Figure 4.28.

An STL-target motion type allowing to project the selected nodes onto a target surface was assigned to the nodes inside the selection encapsulation. In order to assign this kind of motion, an STL file (in ASCII format) has to be given as one of the inputs.

An STL file describes an unstructured triangulated surface by the unit normal and vertices of the triangles using a three-dimensional Cartesian coordinate system. In this instance the STL file had to describe the cylindrical surface needed to be recovered, namely the portion of the duct wall inside the selection encapsulation (i.e. the only portion of the surface mesh allowed to deform as a consequence of the shadow area rotation).

Therefore the surface resulting from the intersection between the duct and the box-shaped selection encapsulation was extracted inside SolidWorks™ (as shown in yellow in Figure 4.31) and converted into an STL file (as shown in Figure 4.32) with the maximum possible resolution.
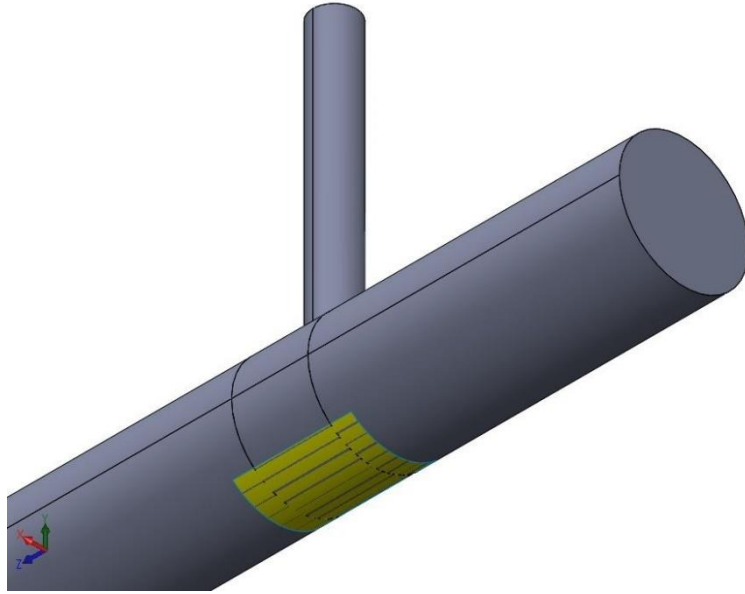
Figure 4.31: Patch extraction

Figure 4.32: STL file extracted through SolidWorks

The projection method of RBF Morph is based on the implicit surface approach: the centroids of the STL file and their normal are used to define the surface. Therefore a uniform distribution of triangles in all the directions is suggested, in order to accurately define the surface and to obtain a high quality projection.

In the obtained STL, the presence of only one triangle in the axial direction causes problems during the projection, therefore a remeshing was needed. This latter task was managed inside MeshLab.

Starting from the STL description extracted through SolidWorks (made of 338 triangles), the "subdivision surfaces: midpoint" filter (a remeshing filter that uniformly refines a mesh, substituting each triangle with four smaller triangles) was applied. In order to reduce the large number of obtained triangles, the "simplification: quadratic edge collapse decimation" filter was used. All the parameters of these filters were fine-tuned in order to obtain an adequate description of the patch. The obtained STL file, made of 34650 uniformly distributed triangles, is shown in Figure 4.33.
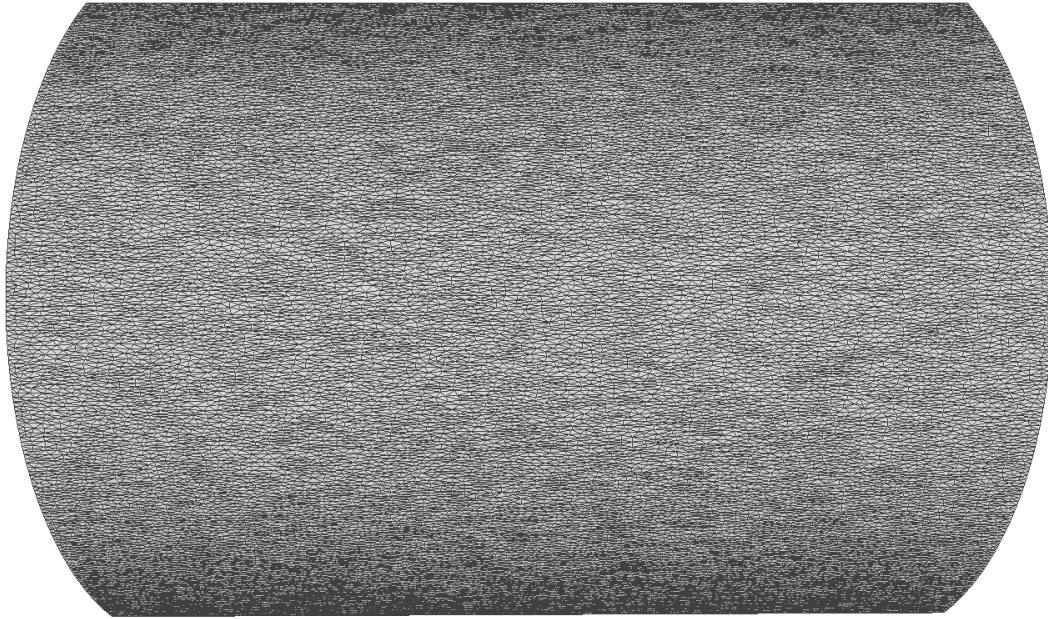
Figure 4.33: Remeshed STL file

This STL file was then imported inside RBF Morph, as shown in yellow in Figure 4.34 (that also underlines the cylinder distortion), and set as the motion law.
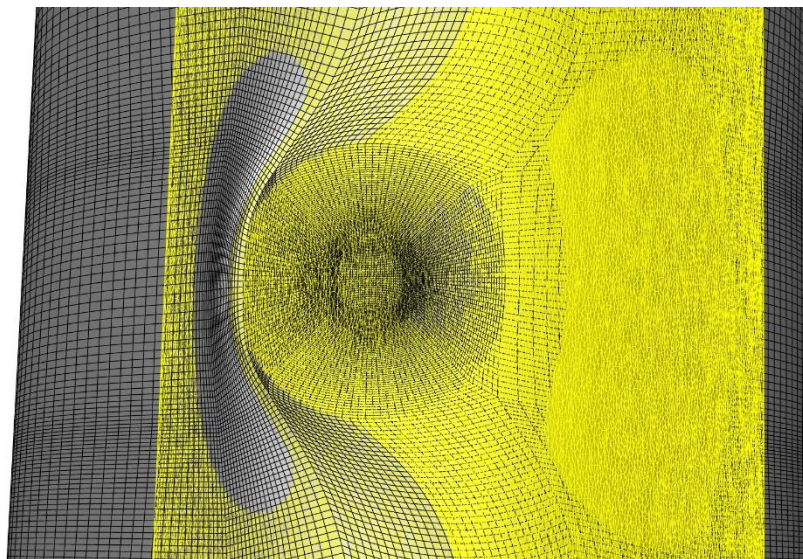
Figure 4.34: STL file imported into RBF Morph

In order to reduce the number of used centroids and to get a regular distribution, a sampling distance of 0.7 mm was imposed but the LCM distance was set to zero.

Here the LCM distance is used in managing large STL models to reduce the projection time, keeping the same quality of the surface. In this application it was not needed and therefore it was set to zero, whereas the sampling distance value was the consequence of a compromise between the size of the projection problem and the fidelity in target surface reproduction.

The last parameter needed to setup the STL-target motion is the "delta offset", that defines the distance from the centroid along the normal at which two points (one in the positive and one in the negative direction) are generated. Those two points, along with the centroid of the triangle, are used to setup the projection problem. The value of the delta offset shall be small enough to avoid clashes at high curvature regions and large enough to properly attract the mesh onto the target surface and so it was set to 1 mm.

This led to the conclusion of the setup of the STL-target motion, after which the calculation of the projection was performed. The result of this calculation was a set of source points, namely the nodes located on the distorted surface, with an associated displacement able to project them onto the target surface (i.e. the undeformed cylinder).

In addition to what just stated, a null motion was imposed to the thermowell surface and to the buffer nodes between the selection encapsulation and the domain encapsulation, as in the previous solution.

As far as solver settings are concerned, the Gaussian was the selected RBF and the LCM distance was set to zero, because the number of source points was 30606, making the RBF problem not too large and allowing the disabling of the sub-sampling process.

The result of this setup is shown in Figure 4.35, with the same colouring for the source points as before.
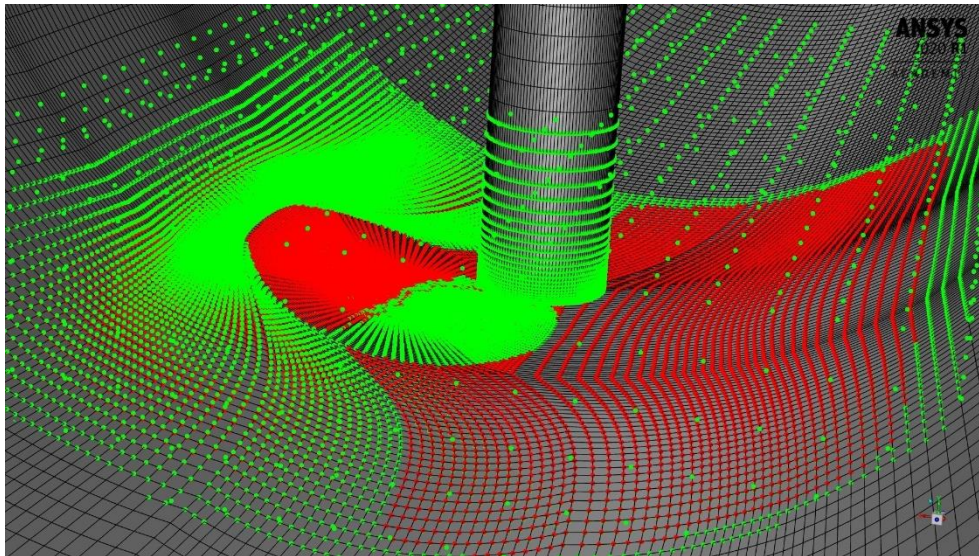
Figure 4.35: STL-target source points

Contrary to what seems to appear, in the shadow area the source points starting and final positions coincide as expected, due to the direct control exerted on those nodes during the shadow rotation.

With regard to the source points on the distorted surface, it seems clear that the projection was implemented as predicted. Therefore the RBF solution was created and applied, resulting in the perfect recovery of the cylindricity of the duct.

It has to be observed that if the rotation of the shadow area is applied with an amplification factor lower than the maximum one, then there is no way in which the implementation of a proportionally amplified STL-target solution could recover the cylindricity of the duct, by cause of the wrong choice of the starting points. Therefore another ploy, explained in the following, had to be used.

To solve this issue, the recovery solution had to be defined starting from the undeformed surface mesh and the only way to obtain such solution was to manually build it using the information gathered until now.

At this point, three meshes are available: the starting one, the distorted one (after the shadow area rotation) and the recovered one (after the STL-target). In order to build the wanted solution, the position of the affected surface nodes in those three meshes had to be extracted.

Without a properly defined named selection inside Fluent, it was not possible to directly extract the wanted nodes from the surface mesh. Accordingly they had to be manually extracted, but without a specific procedure it was impossible to track the position of every single node in each of the three configurations.

Using ANSYS CFD-Post it is possible to export the domain node number (a constant property, different for every node) for each node of a selected surface. By selecting the wall surface a .csv file is generated, in which the list of the nodes belonging to that surface is reported. This latter list relates, for each node, its x, y and z coordinates and its domain node number.

Three of those files were exported, one for each available mesh, and then imported into MATLAB™. Knowing the extent and the position of the domain encapsulation, all the nodes inside it were extracted from the starting mesh.

At this point it was possible to track the position of each node inside the domain encapsulation by looking for its domain node number in the other two exported meshes. Being aware of the successive positions of each node in the three meshes, a new .pts file was written in which the source points were the nodes extracted from the starting surface mesh (inside the domain encapsulation) and their displacement was calculated as the difference between their corresponding position in the recovered mesh and in the distorted mesh.

By doing so it was possible to setup a recovery solution defined starting from the undeformed mesh and with an associated displacement able to recover the portion of the displacement imposed by the rotation of the shadow area that caused the distortion of the cylindrical surface. Therefore, if the rotation of the shadow area is applied with an amplification factor lower than the maximum one, the cylindricity of the duct can be recovered over-imposing this STL-target-derived solution with a proportional amplification factor.

The source points from the previously generated .pts file were imported into the morpher tool and no further conditions were imposed. As far as solver settings are concerned, the Gaussian was the selected RBF and the LCM distance was set to zero, because the number of source points was 21695, making the RBF problem not too large and allowing the disabling of the sub-sampling process.

After checking that the setup was implemented as expected (see Figure 4.36 and Figure 4.37), the RBF solution was generated.
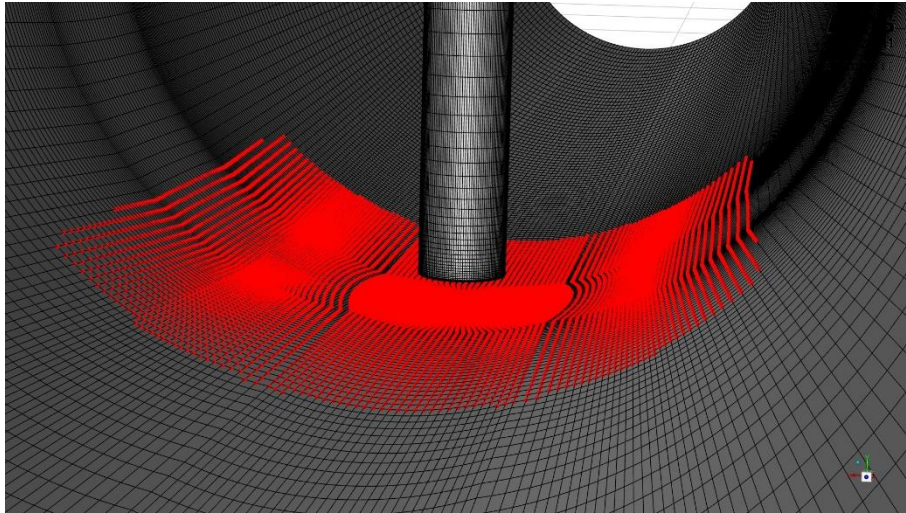

Figure 4.36: STL-target-derived correction, source points starting position
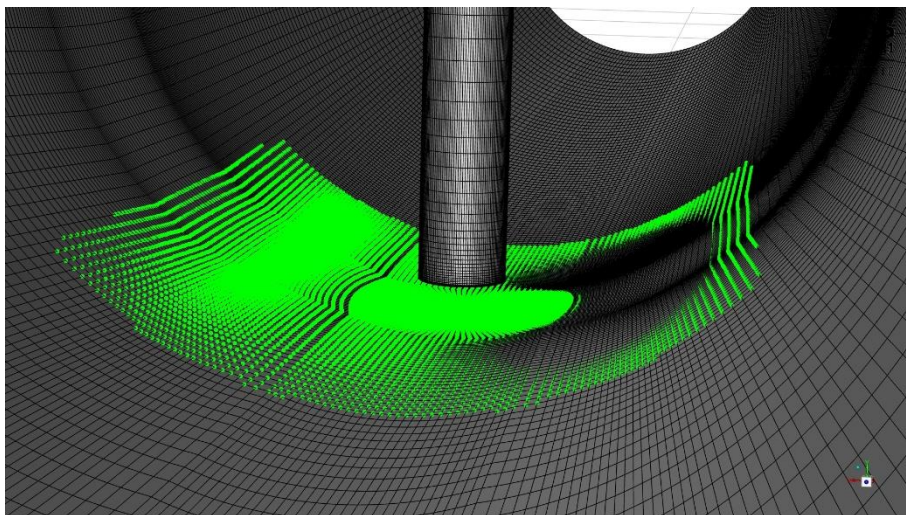

Figure 4.37: STL-target-derived correction, source points final position

It has to be observed that if the shadow rotation is applied with a negative amplification factor (i.e. in the opposite direction), this corrective solution is no longer valid. On account of that a similar corrective solution was built, following the same steps but starting from a -15° maximum rotation.

The previously introduced buffer nodes were needed because during the STL-target morphing some of the nodes were projected outside the domain encapsulation, causing troubles during the process of nodes tracking. Therefore the fixed buffer layer was introduced and the STL-target was applied only to the nodes inside the selection encapsulation; thus, even if during the projection some nodes were moved outside the selection encapsulation, they still remained inside the domain.

4.4.6 Effect of the corrective solutions

The aim of the four corrective solutions is to improve the morphing quality, thus solving the issues highlighted in subsection 4.4.3 and at the end of subsection 4.4.4. In order to check the morphing quality with the addition of the methods of correction, the same set of modal coordinates used in subsection 4.4.3 was imposed and the corrective solutions were properly amplified (how to calculate the amplification factors for the corrective solutions starting from the modal coordinates will be explained in the following).

The morphed volume mesh around the tip of the thermowell is shown in Figure 4.38, whereas the surface mesh is visible in Figure 4.39.

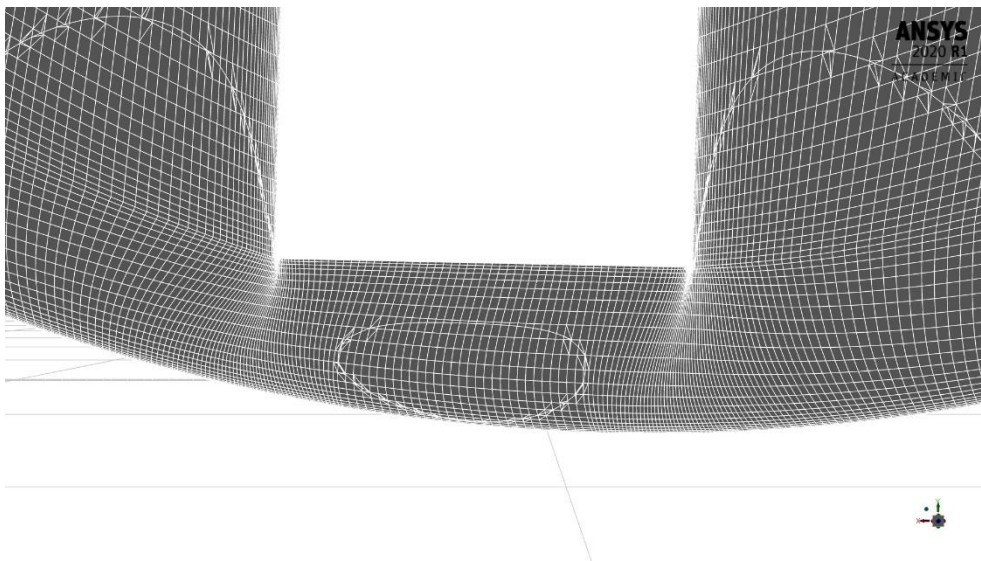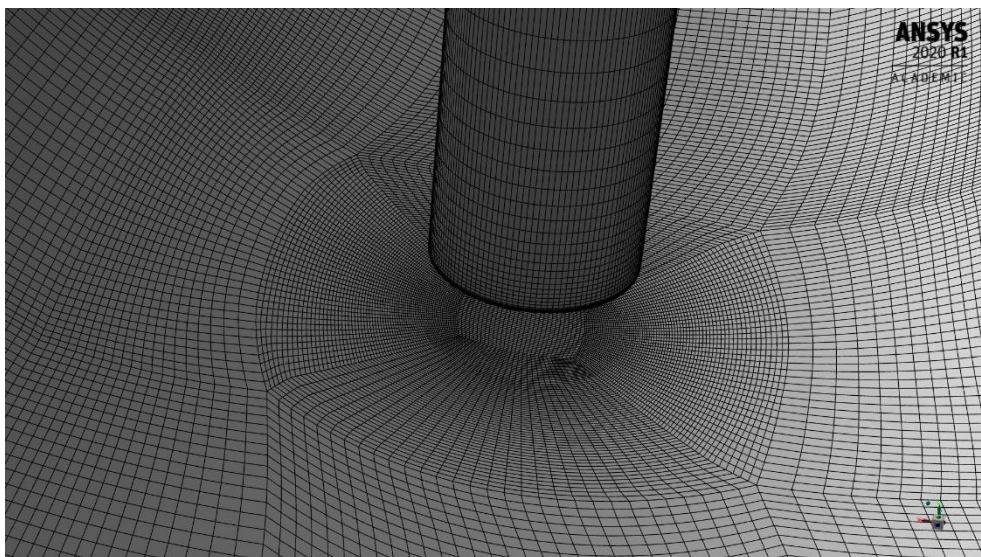**Figure 4.38: Deformed mesh around the tip, with the corrective solutions**

Figure 4.39: Deformed surface mesh, with the corrective solutions

Comparing Figure 4.38 with Figure 4.25, the improvement in morphing quality (lower volume mesh distortion) appears clear. Moreover, the preservation of the cylindricity of the duct and the correct positioning of the shadow area can be also noticed.

Once all the RBF solutions had been checked (in the sense that the cell quality remains satisfactory until reaching the maximum expected tip displacement), it was possible to go ahead with the FSI analysis setup.

4.5   3-D computational grid

The CAD model of the analysed system was generated as described in section 4.2 and then it has been discretized into a computational domain through ANSYS ICEM CFD, using the setup validated in the previously detailed 2-D analysis. The obtained mesh is structured, multiblock and composed of hexahedrons.

The multiblock approach allowed the generation of a structured mesh and the adoption of the appropriate mesh refinements where needed, for example in the wake of the thermowell in which a good mesh resolution is necessary to adequately capture the shed vortices and the wake itself. Moreover, it enabled the generation of high quality cells. The subdivision of the computational domain in blocks is visible in the wireframe shown in Figure 4.40.
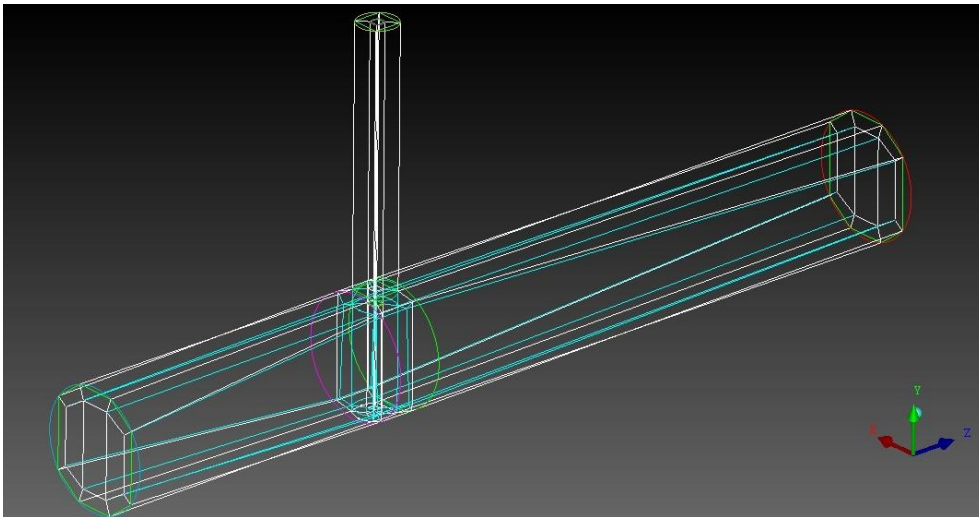

Figure 4.40: Domain subdivision in blocks

The mesh is structured for the known advantages in terms of accuracy and efficiency in calculation, data storage and exchange.

The thickness of the first layer of cells near the walls has been chosen to obtain an y^+ lower than one, in order to solve the wall boundary layer and to implement the SST k-ω turbulence model. After the first layer at the walls, the thickness of the cells grows with a factor of about 1.2. This allows for a smooth growth of the cells, avoiding rough changes in their dimensions.

The obtained structured mesh, composed of 3158640 hexahedral cells, is shown in different views: in Figure 4.41 the volume mesh around the thermowell is displayed in a cross-section perpendicular to the duct axis; in Figure 4.42 the volume mesh is shown in a cross-section containing the two axes, one of the duct and the other of the thermowell; in Figure 4.43 the volume mesh around the thermowell and its resulting surface mesh are

presented; in Figure 4.44 the resulting surface mesh of the pipe is shown; in Figure 4.45 the volume mesh around the thermowell is displayed in a cross-section perpendicular to the thermowell axis; in Figure 4.46 and Figure 4.47 the resolution of the mesh near the walls can be appreciated.
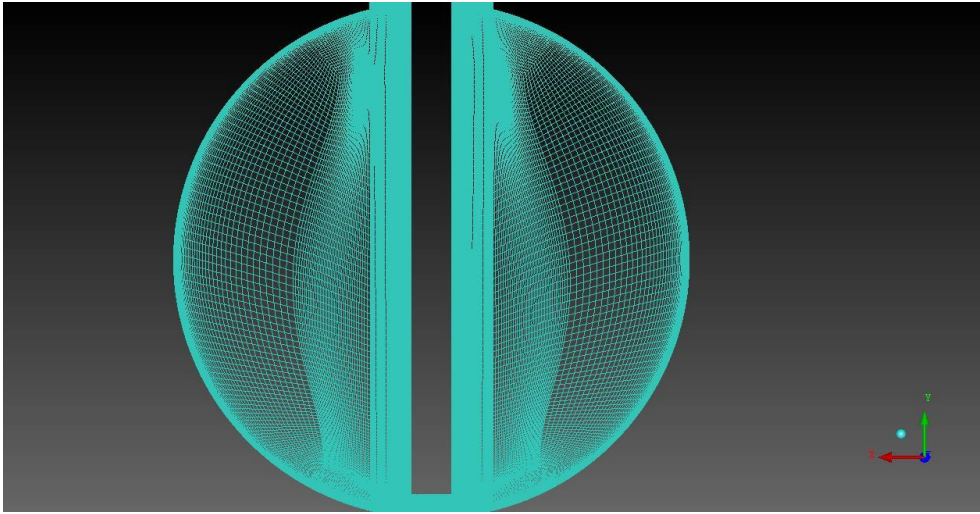
Figure 4.41: Volume mesh, first cross-section
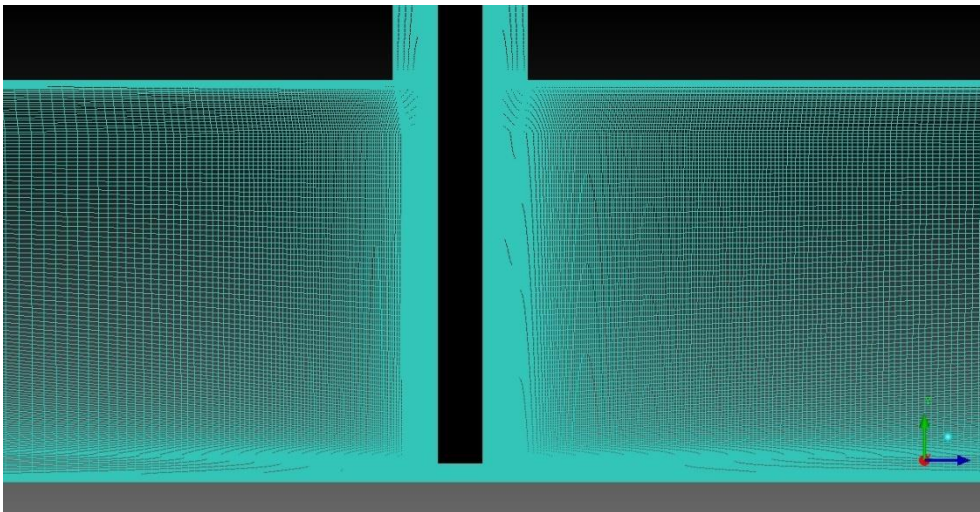
Figure 4.42: Volume mesh, second cross-section
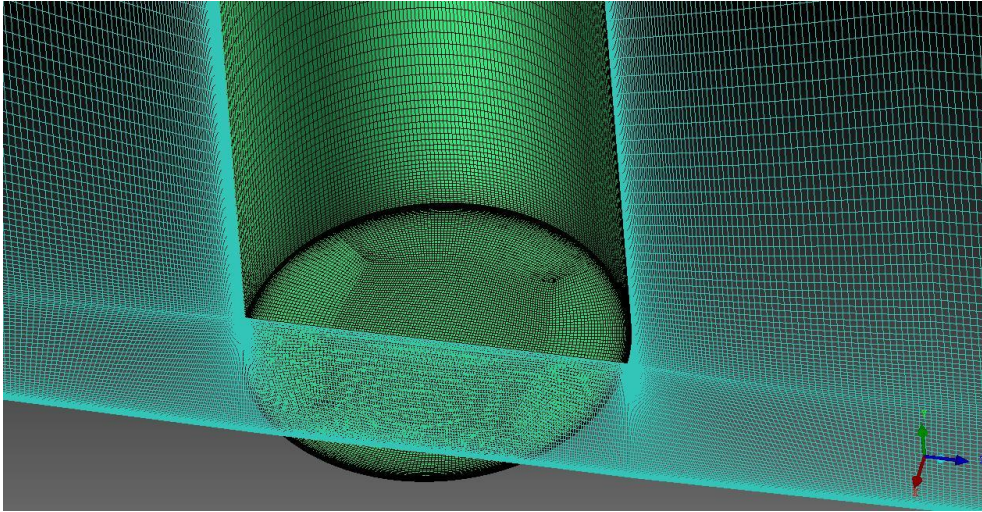
Figure 4.43: Volume mesh and thermowell surface mesh
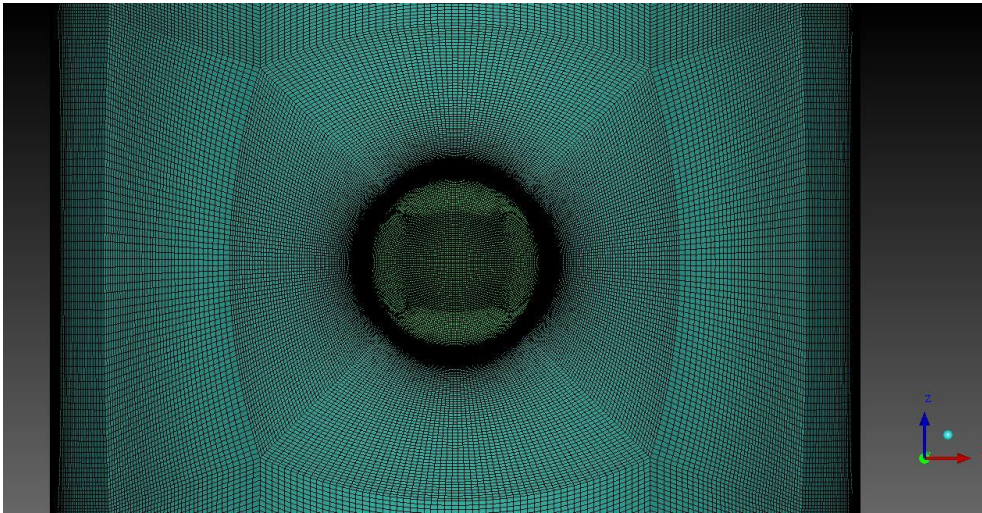
Figure 4.44: Duct surface mesh
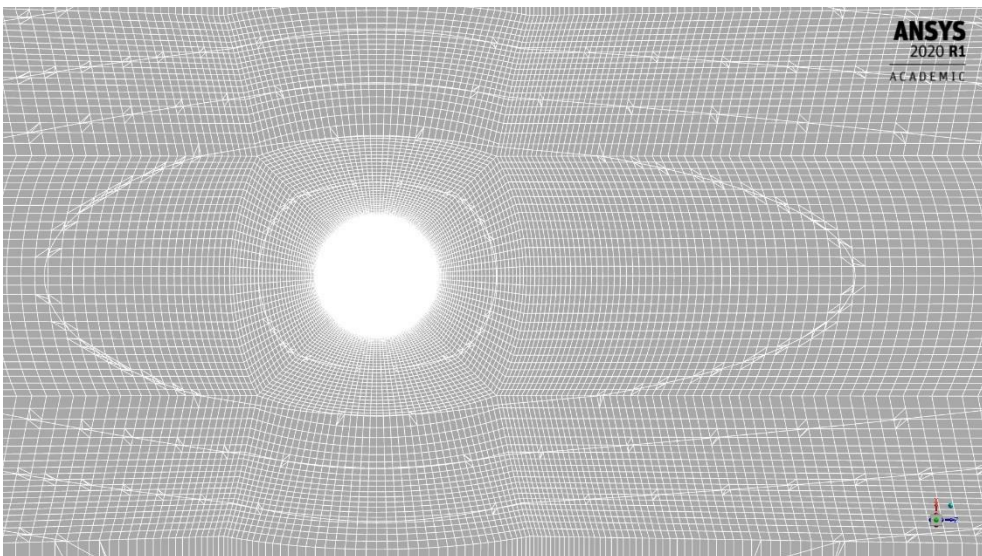
Figure 4.45: Volume mesh, third cross-section
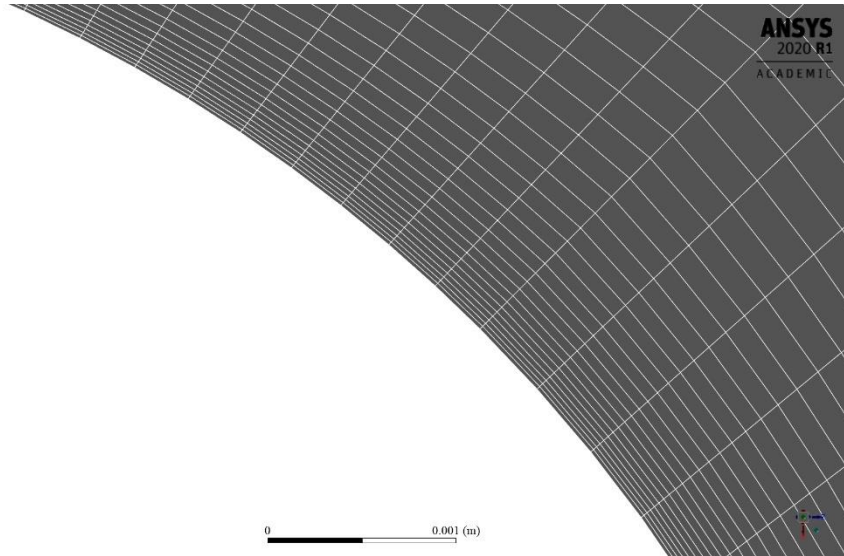
Figure 4.46: Mesh resolution near the thermowell
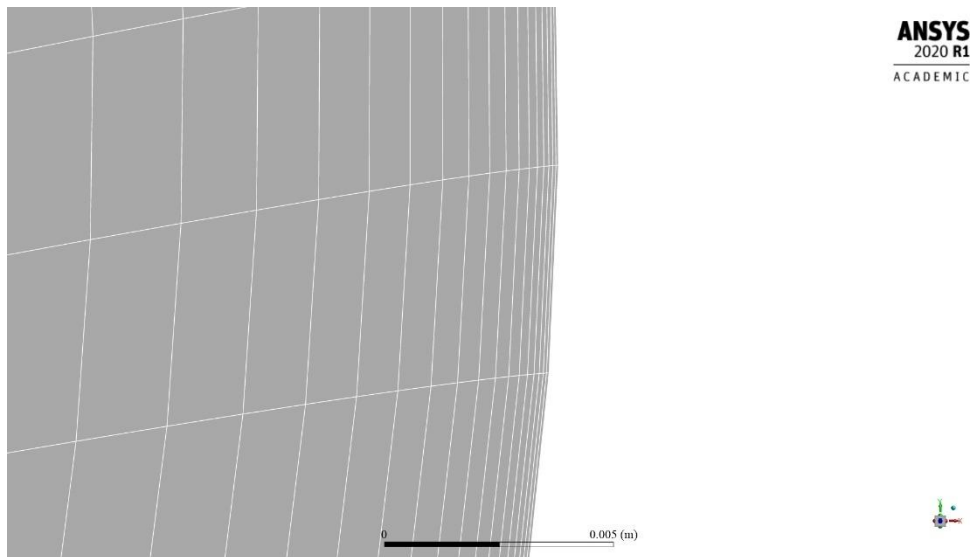
Figure 4.47: Mesh resolution near the pipe wall

Inside ICEM a mesh quality evaluation, using the determinant 2x2x2 criterion, was carried out. The resulting histogram, showing the high quality of the obtained mesh, is reported in Figure 4.48.
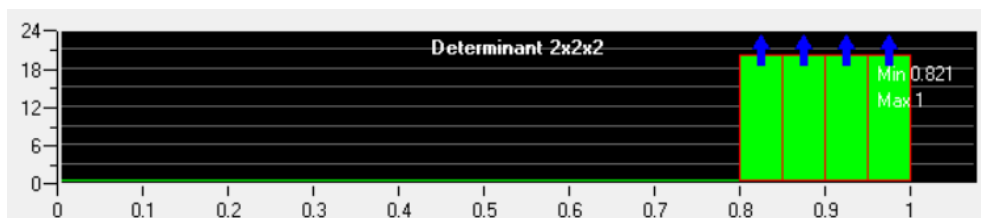
Figure 4.48: Determinant 2x2x2 histogram

4.6 CFD setup

The obtained mesh was imported inside Fluent (see Figure 4.49 and Figure 4.50) and the CFD setup was carried out, following the one validated in the previously detailed 2-D analysis.

Figure 4.49: Imported mesh, first view
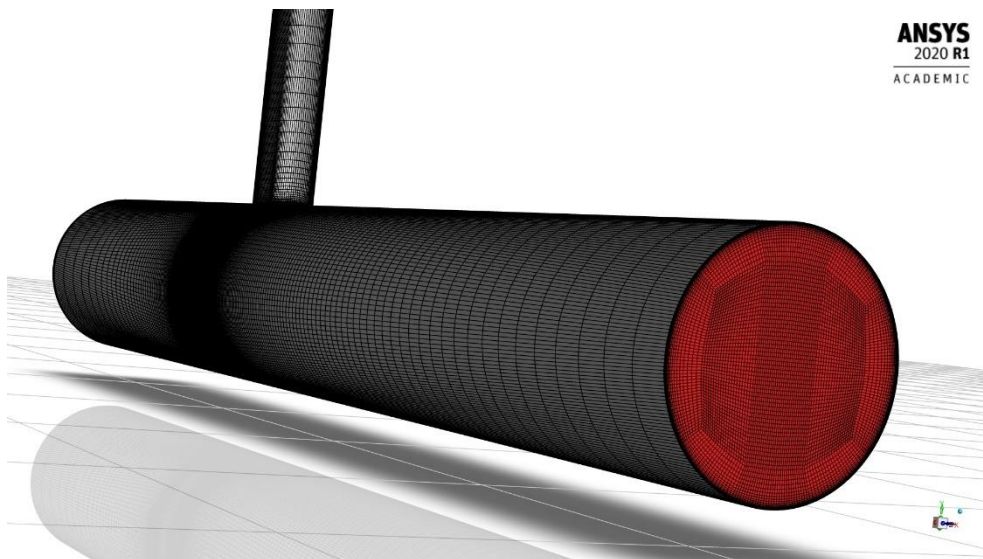
Figure 4.50: Imported mesh, second view

In the experimental setup the thermowell was immersed in a flow of liquid water but none of its properties were specified. Therefore it was considered as standard water at 20°C, thus its density was assumed to be 998 kg/m^3 and its dynamic viscosity 0.001002 kg/(m·s). The aim of the presented work was to simulate the transverse vibration lock-in region that the experimental results located at an inlet velocity of about 6.4 m/s. Therefore such velocity was assumed at the inlet, resulting in a Reynolds number of about 100000 which falls inside the sub-critical regime, as previously stated.

Being the fluid a liquid, the flow can be considered incompressible. Consequently a pressure-based solver was implemented, the water density was assumed to be constant and the energy equation was disabled in the modeling process.

Being the vortex induced vibration an unsteady phenomenon, a transient analysis was implemented.

An URANS approach is adopted with the SST k-ω turbulence model. The model constants were left with the default values and some available options were enabled: low-*Re* corrections, curvature correction with constant and unitary C_{curv} parameter as by default, production Kato-Launder, production limiter and intermittency transition model.

A velocity-inlet boundary condition was set to the inlet (blue surface in Figure 4.49), with a 6.4 m/s velocity normal to the boundary and zero initial gauge pressure. The turbulence at the inlet was specified through a unitary intermittency, a 5% turbulence intensity and the hydraulic diameter of the inlet section (0.1524 m).

At the outlet a pressure-outlet was set (red surface in Figure 4.50) with zero gauge pressure and the same turbulence specifications used at the inlet, in case of reverse flow.

The pipe (i.e. the "wall" surface) and the thermowell were set as no slip walls.

As far as solution schemes are concerned: the SIMPLE pressure-velocity coupling method was adopted (considered sufficient because the flow is incompressible and at low *Re*), the second order for pressure, the second order upwind for momentum and turbulence parameters, the least squares cell based for gradient (because the inclination of the cells is likely increased with the deformation of the mesh). The chosen transient formulation was the first order implicit with a fixed time advancement. The under-relaxation factors were left as by default.

As in the 2-D analysis, the time-step size and the number of internal iterations are the main parameters influencing the results of the simulations in terms of vortex shedding phenomenology and evolution of the fluid forces acting on the thermowell, therefore an accurate study (similar to the 2-D one) to setup those parameters was carried out.

It has to be considered, also, the assumption of constant forces that lies behind equation 2.48 (used to update the values of the modal coordinates): it implies that the chosen time-step size has to be small enough to justify this hypothesis.

Without diving into details, the conclusion of the study was that the best compromise between solution accuracy (meaning that the vortex shedding phenomenon and the vortex induced vibration are adequately captured) and computational effort was a time-step size of 10^{-4} s.

As far as the number of internal iterations is concerned, setting a fixed value was not considered a good idea because during the calculation some degree of cell distortion was introduced by the morphing actions, thus making the convergence slightly more difficult within some of the time-steps. Setting an always sufficient

constant value (based on the "harder" time-steps) would result in an overshoot (in terms of number of iterations) in the "easier" time-steps; instead setting a constant value based on the "easier" time-steps would result in a non-sufficient convergence in the "harder" time-steps. Therefore a computer-controlled convergence criterion was implemented: the chosen checked quantity was the absolute value of the scaled residual of the continuity equation and the threshold value for the convergence was set to 10^{-5}. This latter value was chosen because it guaranteed the convergence of the fluid forces on the thermowell within every time-step and an adequate accuracy of the generated results.

Usually the convergence condition was reached within 20 to 30 iterations, but to keep it safe the maximum number of iterations was set to 100.

4.7 FSI setup

As previously stated, the FSI approach used in this thesis is based on the modal theory and it was carried out through RBF Morph. In order to apply the above introduced RBF solutions, the right amplification factors have to be given to the morpher tool. To accomplish such task a set of functions and commands had to be defined and it will be detailed in the following.

Once the generated Fluent case is loaded, the first step is to define the surfaces object of the morphing actions (in this case the thermowell and the pipe wall), through the TUI command *(define surfaces '(thermowell wall))*.

Then, the names of the RBF solutions used to implement the morphing actions have to be assigned through the TUI command *(define modes '("Mode-1_2step" "Mode-2_2step" "Mode-3_2step" "Mode-4_2step" "Mode-5_2step" "Mode-6_2step" "shadow_tra" "shadow_rot" "stl_target_pos" "stl_target_neg"))*: in which the first six solutions are the second steps of the RBF solutions defining the six considered natural modes; whereas the last four are the corrective solutions (in order: the translation of the shadow area, the rotation of the shadow area, the STL-target-derived correction for the positive rotations, the STL-target-derived correction for the negative rotations).

The frequencies of the natural modes are assigned through the command *(define modal-f '(53.925 53.925 336.5 336.5 935.87 935.87 1 1 1 1))*: where the first six are the frequencies of the six natural modes obtained through the FEM analysis, whereas the last four are random values assigned to the corrective solutions that won't be used during the calculation.

The time-step size, equal to the one used for the CFD analysis, is assigned through the command *(define modal-dt 0.0001)*.

The structural damping, result of an appropriate study that will be exposed later, is assigned through the command *(define zita 0.041)*.

At this point two files are loaded: the executable that handles the unsteady FSI analysis (through the command *(fast-load (open-input-file "modal-transient-zeta-1000.bin") (the-environment)))*) and a scheme function that manages the corrective solutions (through the command *(load "shadow_control_function.scm")*).

The file in which the main data of the FSI analysis will be reported is set through the command *(define filename 'first-FSI-set)*.

At this point all the needed data are set and the *(modal-q-update-init)* command can be issued. This latter command, enabled by the previously loaded executable, initializes the FSI environment: more in details, it opens the RBF Morph library, loads the assigned RBF solutions and assigns a zero initial value to all the modal coordinates and their derivatives.

It has to be observed that after this command is executed, the solutions are stored in memory and thus all the subsequent calls will require virtually no computation time; this allows for transient morphing (needed for the unsteady FSI analysis) with virtually no additional computational costs, if compared to the same transient simulation without morphing.

To finalize the FSI setup, two commands to execute at the end of each time-step are set: *(shadow_control)* and *(modal-q-update)*, in this order. Both are scheme functions defined inside the previously loaded files.

The *(modal-q-update)* command, enabled by the loaded executable, is the core of the modal superposition method. At the end of each time-step it executes the *(rbf-fmorph-forces surfaces)* command (enabled by the RBF Morph library), that calculates the values of the modal forces acting on the assigned surfaces, performing a surface integral of the flow loads at the current time-step on those surfaces and then projecting the loads onto the modal shapes. Once the modal forces are known, the new modal coordinates are computed through the equation 2.48. At this point the mesh is morphed applying the combined effect of the loaded RBF solutions, obtained over-imposing linearly each solution with respect to the baseline configuration with the associated computed modal coordinate as its amplification factor.

As anticipated in subsection 4.4.2, to cope with the 0.001 amplification factor applied to the solution of the first step when it was imposed as the motion law in the subsequent stage, an adjustment to the just described workflow had to be applied: a multiplication by 1000 of the modal forces (to obtain the modal forces referred to the mass-normalized modes, in order to apply the equation 2.48) and of the modal coordinates before the morphing action (because the modal coordinates are referred to the mass-normalized modes, whereas the loaded modal solutions are reduced by a factor of 1000) was imposed.

The *(shadow_control)* command, enabled by the loaded scheme function, computes the amplification factors of the corrective solutions (it has to be specified that the modal coordinates and the amplification factors of the corrective solutions are stored in the same list, with the same order as in the list *modes*). As previously stated, the purpose of the first two corrective solutions is to keep the shadow area always under the tip of the thermowell, therefore their amplification factors have to be calculated as a function of the tip displacement.

The immediately available data during the FSI calculation are the modal coordinates in the current time-step. Therefore, in order to derive the tip displacement, the directional deformations at the tip in the x (transverse) and z (streamwise) directions (the used reference frame is visible in all the figures of this chapter) were extracted from the FEM modal analysis. Their values are reported in Table 4.4.

Mode	x directional deformation [m]	z directional deformation [m]
1	0.98521	2.0004
2	2.0004	-0.98521
3	0.98739	1.992
4	1.992	-0.98739
5	1	1.9736
6	1.9736	-1

Table 4.4: Modal analysis, directional deformations at the tip

This information is introduced in the FSI environment via the loaded scheme function.

The amplification factor for the shadow translation (recalling that it was defined with a unitary displacement in the positive z direction) can be calculated as the sum of the products of the modal coordinates by the z directional deformations associated with each mode, as shown in equation 4.2:

$$Z_{shadow} = \sum_{i=1}^{n_{modes}} q_i A_{z_i} \tag{4.2}$$

Where: Z_{shadow} is the amplification factor for the shadow translation, n_{modes} is the number of considered modes (in this case, six), q_i is the i-th modal coordinate, A_{z_i} is the directional deformation in the z direction of the i-th mode. Obviously Z_{shadow} coincides with the tip displacement in the z direction.

The tip displacement in the x direction can be calculated in the same way, but using the x directional deformations, as shown in equation 4.3:

$$X_{shadow} = \sum_{i=1}^{n_{modes}} q_i A_{x_i} \tag{4.3}$$

Where X_{shadow} is the shadow translation in the x direction that has to be imposed (equal to the tip displacement in the transverse direction) and A_{x_i} is the directional deformation in the x direction of the i-th mode.

Therefore the amplification factor for the shadow rotation (recalling that it was defined with a one degree positive rotation) can be calculated with equation 4.4 (in degrees):

$$\theta_{shadow} = \tan^{-1} \frac{X_{shadow}}{R_{tip}} \tag{4.4}$$

Where: θ_{shadow} is the amplification factor for the shadow rotation and R_{tip} is the distance of the tip of the thermowell from the duct axis (in this case 69.215 mm, another parameter introduced with the loaded scheme function).

As previously stated, the amplification factors of the last two corrective solutions are proportional to the shadow rotation. If the rotation is positive, the amplification factor of the fourth corrective solution (the STL-target-derived one in the case of negative rotation) is zero and the one for the third (the STL-target-derived one in the case of positive rotation) can be calculated as $\frac{\theta_{shadow}}{15}$ (recalling that the maximum expected rotation was 15° and it was used to build the last two corrective solutions); if the rotation is negative, the amplification factor for the third correction is zero and the one for the fourth can be calculated as $-\frac{\theta_{shadow}}{15}$.

It has to be observed that *(shadow_control)* is executed at the end of the time-step, before *(modal-q-update)*. Therefore the first aspect that needs to be noticed is that the overall corrective solution is based on the modal coordinates of the previous time-step, but this is not an issue since the tip displacement does not vary too much from a time-step to the next one, given the fine temporal discretization.

Secondly, the mesh update is done at the end of the execution of *(modal-q-update)*, therefore this latter command would overwrite the previously calculated amplification factors for the corrective solutions. In order to avoid this issue, the last four modal coordinates derivatives and the last four modal forces are enforced to be zero.

With regard to the modal coordinates derivatives, their values from the previous time-step are used inside *(modal-q-update)* to compute the new modal coordinates with equation 2.48 and then they are updated. Hence it is sufficient, in order to eliminate this unwanted contribute, to set the last four modal coordinates derivatives to zero at the end of *(shadow_control)*.

With regard to the modal forces, it has to be kept in mind that *(rbf-fmorph-forces surfaces)* is called inside *(modal-q-update)* before the computation of the new modal coordinates and its output cannot be modified. Therefore it would compute the "modal" forces (the quotation marks are used because the corrective solutions are not modal solutions, they are inserted in the list *modes* just to easily introduce them in the FSI environment) also on the corrective solutions, generating nonsense amplification factors through the equation 2.48. To solve this issue, at the end of *(shadow_control)* the *(rbf-fmorph-forces surfaces)* is called and the "modal" forces on the corrective solutions are computed (obtaining the same values as later inside *(modal-q-update)*, being in the same time-step); then constant modal forces are applied to the corrective solutions (through the list *modal-forces-const*) with values equal to minus the one calculated with *rbf-fmorph-forces*. Therefore, inside *(modal-q-update)*, the resulting "modal" forces on the last four solutions are null, leaving unaffected the amplification factors computed inside *(shadow_control)*.

Lastly, it has to be kept in mind that before the morphing action inside *(modal-q-update)*, the modal coordinates are multiplied by 1000, therefore inside *(shadow_control)* the obtained amplification factors are divided by

1000, due to the fact that they are based on the modal coordinates (that are referred to the mass-normalized modes).

At this point the setup is complete, so that the case can be initialized (in this application an hybrid initialization was used) and the FSI calculation can begin.

4.7.1   Displacement calculation by means of modal coordinates

Once the simulation is completed, the modal coordinates at each time-step are available through the reporting file. In each row of this latter, the first six values are the six computed modal coordinates at the current time-step, whereas the last four are the amplification factors for the corrective solutions divided by 1000.

Reading this file into MATLAB and using equation 4.5, it is possible to compute the three components of the displacement of all the nodes on the surface of the thermowell at each time-step.

$$\Delta x_j = \sum_{i=1}^{n_{modes}} q_i v_{i_{j,x}} \tag{4.5}$$

Where Δx_j is the displacement in the x direction of the j-th node on the FEM surface mesh of the thermowell and $v_{i_{j,x}}$ is the j-th component in the x direction of the i-th modal shape (i.e. the displacement in the x direction of the j-th node of the surface mesh associated to the i-th modal shape, computed through the modal analysis). Similar equations can be written for the y and z displacements.

By taking into account a monitoring node on the tip of the thermowell, the temporal evolution of the tip displacement can be reconstructed.

4.8 Damping ratio

The accuracy of any dynamic solution is dependent on the damping assigned to the model. Usually the overall system damping is defined as a percentage of the critical damping, also called "damping ratio". Without diving into details, its influence on the system response is exemplified in Figure 4.51 [21]. Such diagram refers to a one degree-of-freedom mass-spring-damper system subject to a harmonic excitation and it reports the magnitude of the frequency response as a function of the ratio between the frequency of the harmonic excitation and the natural frequency of the system, with the damping ratio as a parameter. The frequency response is a nondimensional ratio and it is a measure of the system response to the harmonic excitation, a kind of amplification ratio of the excitation.
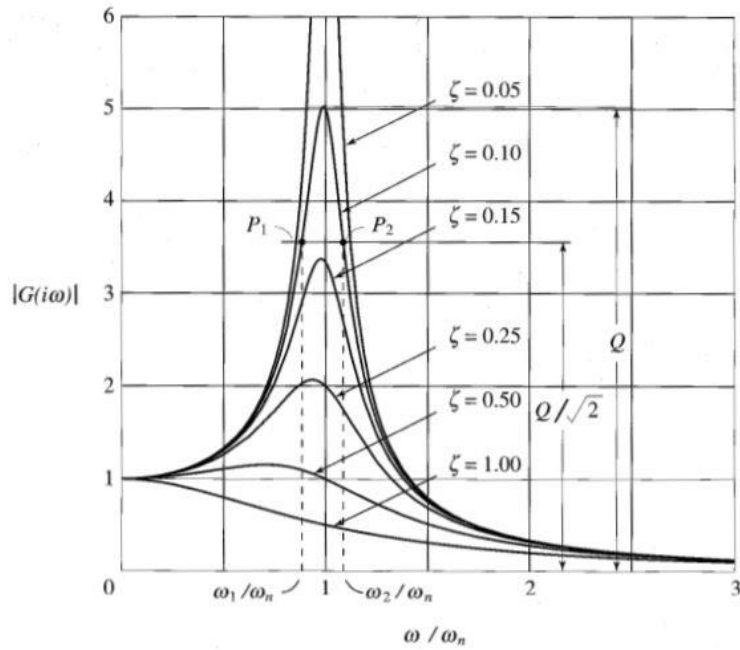
Figure 4.51: Magnitude of the frequency response

It appears clear that the damping has a strong influence on the system response (especially when the system is driven near its natural frequency), reducing the amplitude and shifting the peak to the left with respect to the resonance condition (i.e. driving frequency equal to the natural frequency of the system). A similar behaviour is expected in the considered application (the thermowell can be thought as a mass-spring-damper system subject to the harmonic excitation generated by the vortex shedding), therefore a change in the damping ratio value is expected to generate a change in the vibration amplitude of the thermowell.

In the FSI setup one of the main unknowns is the structural damping ratio, being a property that should be experimentally measured. Since the available experimental data did not report anything about it, some guidance taken from the literature was found to be necessary [29]. Some typical system damping ratios for various types of structures are reported in Table 4.5.

System	Damping ratio
Metals (in elastic range)	<0.01
Continuous metal structures	0.02 to 0.04
Metal structure with joints	0.03 to 0.07
Aluminium / steel transmission lines	≈0.0004
Small diameter piping systems	0.01 to 0.02
Large diameter piping systems	0.02 to 0.03
Auto shock absorbers	≈0.3
Rubber	≈0.05

Table 4.5: Typical damping ratios

The studied thermowell is a metal structure screwed to a flange, which in turn is screwed to a pipe. Knowing that all the interfaces contribute to an increase of the structural damping, it makes sense to assume that the thermowell damping ratio falls in the 0.01 to 0.07 range, even if there is no way to univocally determine it at this stage.

Therefore a parametric study to fine-tune the damping ratio was carried out. The aim of this study was to find a value of the damping ratio, located in the above mentioned range, able to reproduce the experimental results (namely the 8.3 mm maximum root mean square transverse displacement of the tip).

From this point onwards all the simulations ran on a HPC cluster owned by the University, equipped with 250 GB of RAM and four Intel® Xeon® Gold 6152 CPUs, each of them featuring 22 cores @ 2.1 GHz. Out of the overall 88 cores, 30 were used to run the simulations.

The idea of the parametric study was to perform a set of simulations with the same setup described until this point, changing only the damping ratio from one to another. For each run the simulated flow-time had to be enough to reach a dynamic steady state.

The first chosen value was the lower limit of the above mentioned range, 0.01. The simulation ran until 0.2705 s and then diverged. The obtained temporal evolution of the transverse tip displacement is shown in Figure 4.52.
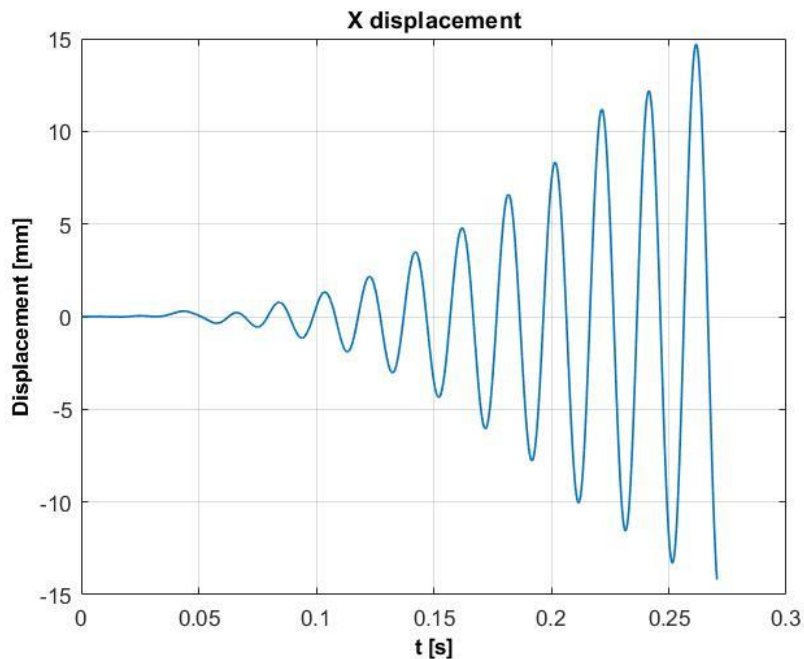

Figure 4.52: Transverse tip displacement, $\varsigma=0.01$

At the end of the simulation the transverse displacement of the tip was -14.19 mm, resulting in a substantial volume mesh distortion that caused the divergence. Figure 4.53 (corresponding to the last time-step) shows what has just been said: it is possible to appreciate the high mesh distortion and the mass imbalance (i.e. the residual of the continuity equation) building up from the distorted cells and then causing the divergence.
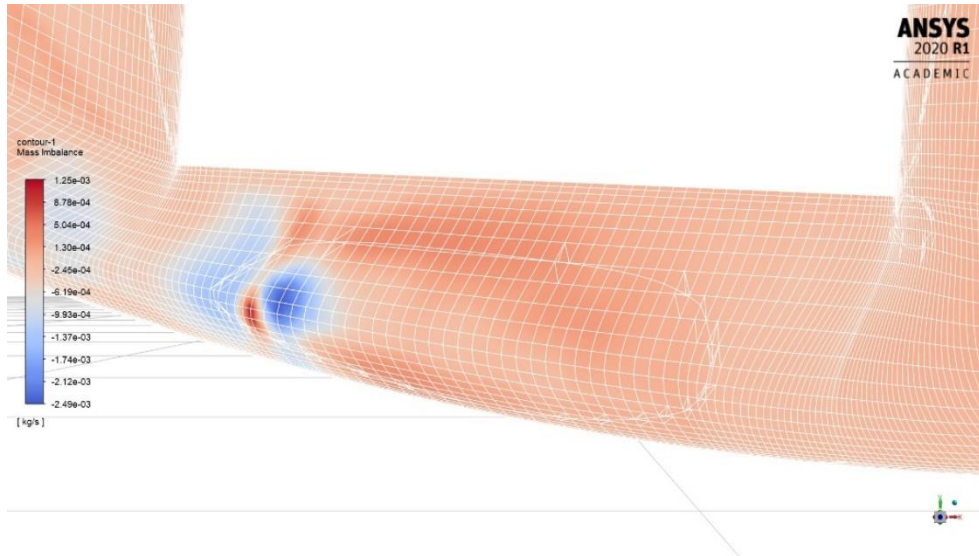
Figure 4.53: Contours of the mass imbalance, end of the simulation, *ς=0.01*

It appears clear that the mesh distortion is due to the superimposition of the volume mesh movements imposed by the tip displacement and by the shadow area rotation, causing the visible s-pattern.

On the other hand, it has to be considered that the wanted maximum RMS transverse tip displacement is 8.3 mm, therefore such large tip movements are not expected when the right damping ratio is applied; hence the RBF solutions were still considered reliable (also because they worked just fine until those extreme displacements, as expected from what stated in subsection 4.4.6).

Moreover, it has to be observed that, despite the divergence of the CFD solver, the proposed FSI setup is able to capture the vortex induced vibration, confirming its validity.

The successive tested value was 0.02 and it led to similar results: the simulation ran until 0.331 s and then diverged. The obtained temporal evolution of the transverse tip displacement is shown in Figure 4.54.
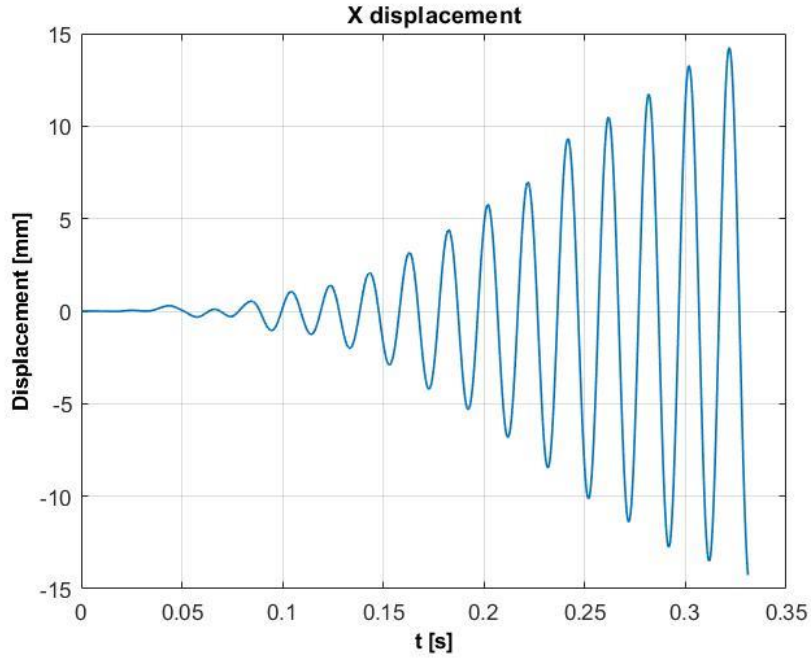
Figure 4.54: Transverse tip displacement, $\varsigma=0.02$

Then a 0.05 damping ratio was tested. This time the simulation did not diverge, therefore it ran until a dynamic steady state was reached and it was stopped at a flow-time of about 0.9 s, after about 5 days of computation. The obtained temporal evolution of the transverse tip displacement is shown in Figure 4.55 and the associated maximum RMS transverse tip displacement is 7.3 mm. It has to be observed that this maximum is associated to an isolated peak; if only the dynamic steady state is considered, the maximum RMS transverse tip displacement is 6.45 mm.
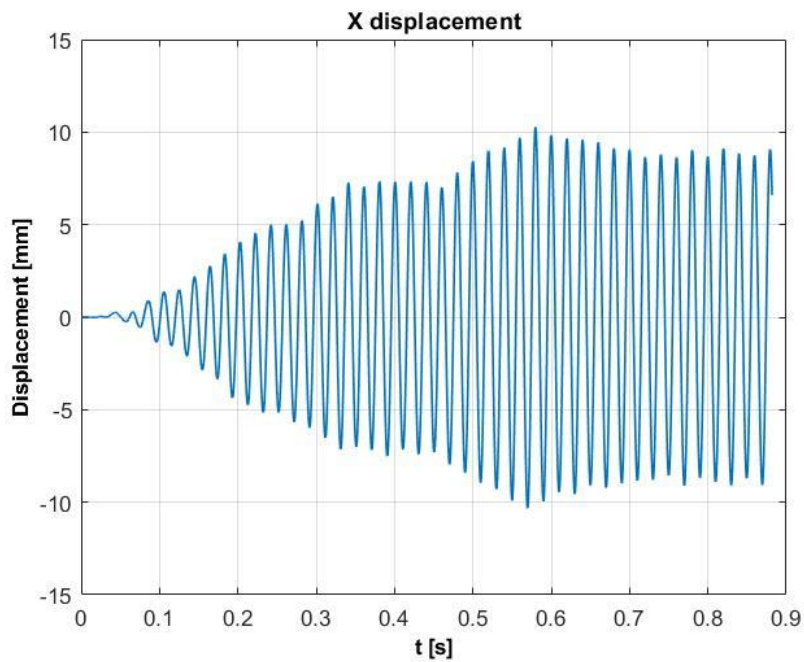

Figure 4.55: Transverse tip displacement, $\varsigma=0.05$

Being this latter value too high, a 0.04 damping ratio was tested. The simulation ran until a dynamic steady state was reached and it was stopped at a flow-time of about 0.8 s, after about 5 days of computation. The obtained temporal evolution of the transverse tip displacement is shown in Figure 4.56 and the associated maximum RMS transverse tip displacement is 8.48 mm.
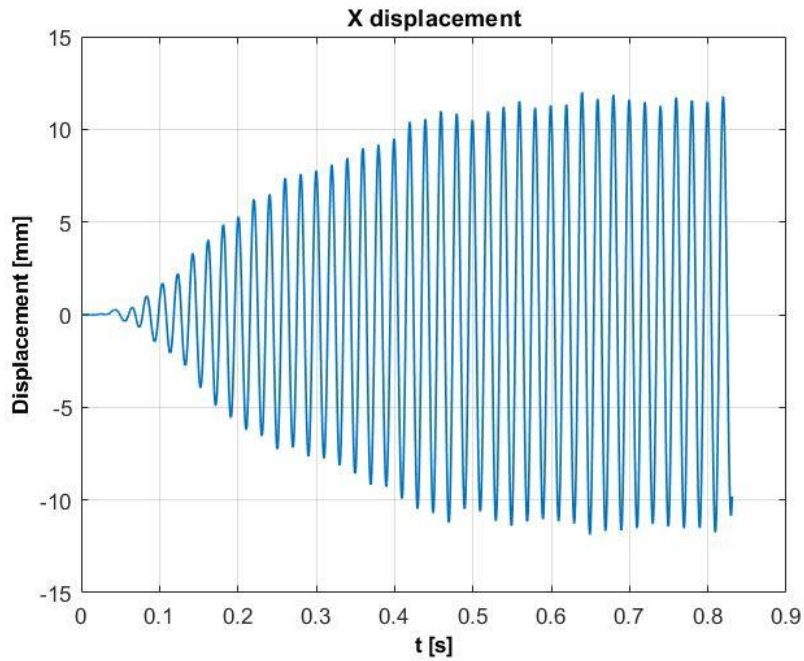

Figure 4.56: Transverse tip displacement, $\varsigma=0.04$

It is clear that the wanted damping ratio falls inside the 0.04 to 0.05 range, therefore a linear interpolation between those two points was built. Using such interpolation and imposing a 8.3 mm maximum RMS displacement, a 0.041 damping ratio was deducted and then tested. The simulation ran until a dynamic steady state was reached and it was stopped at a flow-time of about 0.9 s, after about 5 days of computation. The obtained temporal evolution of the transverse tip displacement is shown in Figure 4.57 and the associated maximum RMS transverse tip displacement is 8.304 mm.
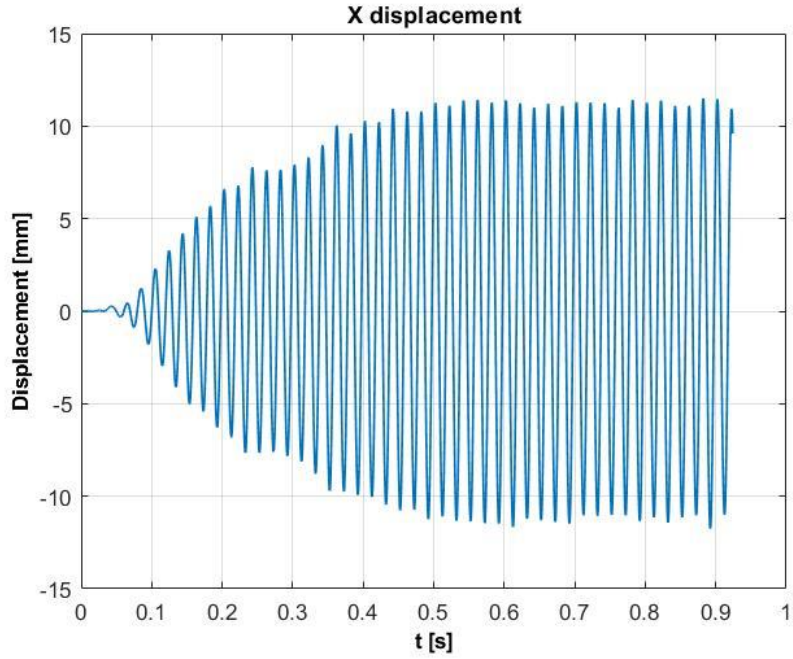
Figure 4.57: Transverse tip displacement, *ς=0.041*

The volume mesh around the tip of the thermowell in correspondence of the maximum transverse displacement with a 0.041 damping ratio is displayed in Figure 4.58. Some degree of mesh distortion is clear but significantly lower than what is visible in Figure 4.53, indeed the CFD solver was able to cope with such distortion and to proceed with the calculation. Hence, once again, the RBF solutions were considered reliable.
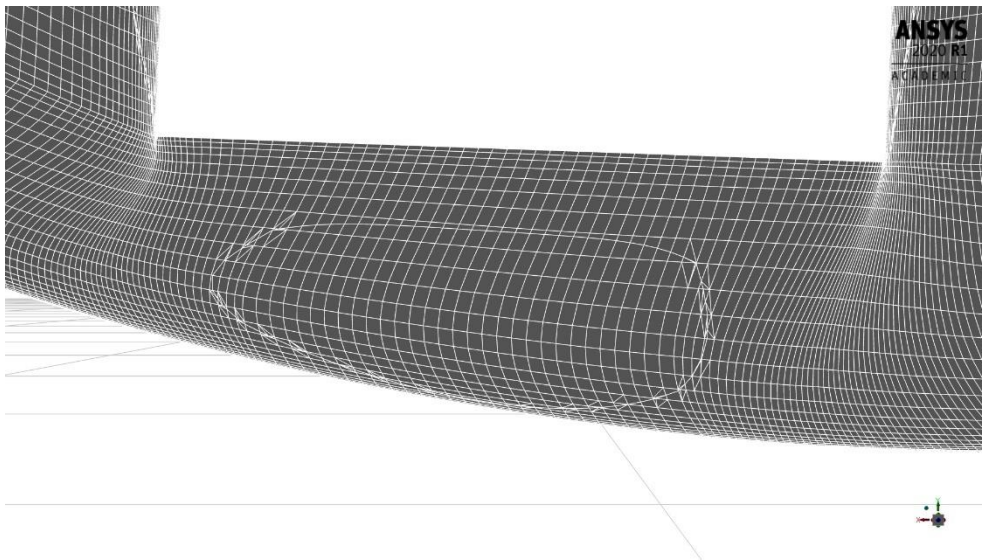

Figure 4.58: Mesh around the tip at maximum transverse displacement (*ς=0.041*)

The obtained results and their relative errors with respect to the experimental data are summarized in Table 4.6.

Damping ratio	Maximum RMS transverse tip displacement at dynamic steady state [mm]	Relative error [%]
0.01	Not reached	-
0.02	Not reached	-
0.05	6.45	22.3
0.04	8.48	-2.17
0.041	8.304	-0.048

Table 4.6: Results of the parametric study

It can be clearly stated that a 0.041 damping ratio, inside the above mentioned range, is able to reproduce the experimental results with sufficient accuracy. For this reason such value was chosen and the parametric study could come to an end.

4.9 FSI analysis results

In this section the results of the FSI analysis, realized using the above described setup, will be presented.

From Figure 4.59 to Figure 4.64 the contours of the velocity magnitude on a plane perpendicular to the thermowell axis are displayed at six different flow-times, corresponding to the maximum transverse displacements, both in the positive and in the negative direction, during three vibration periods once the dynamic steady state was reached.
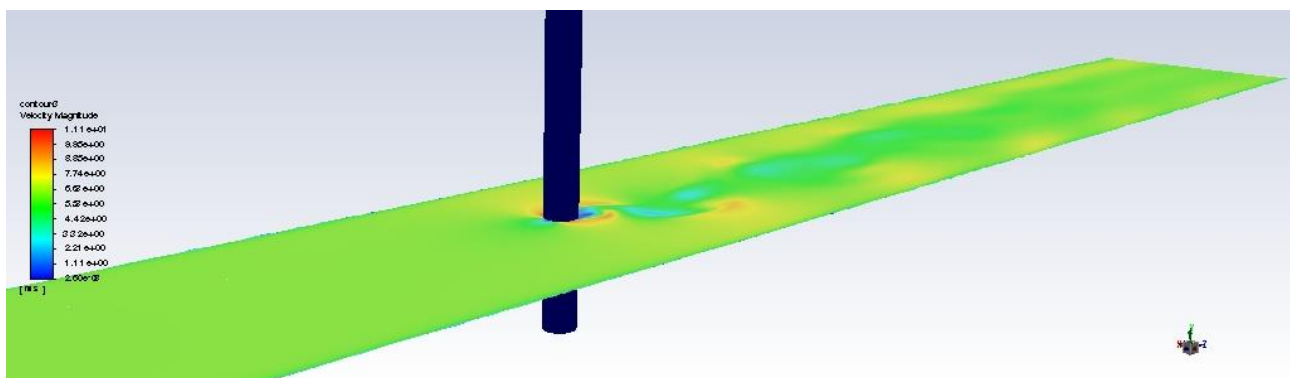

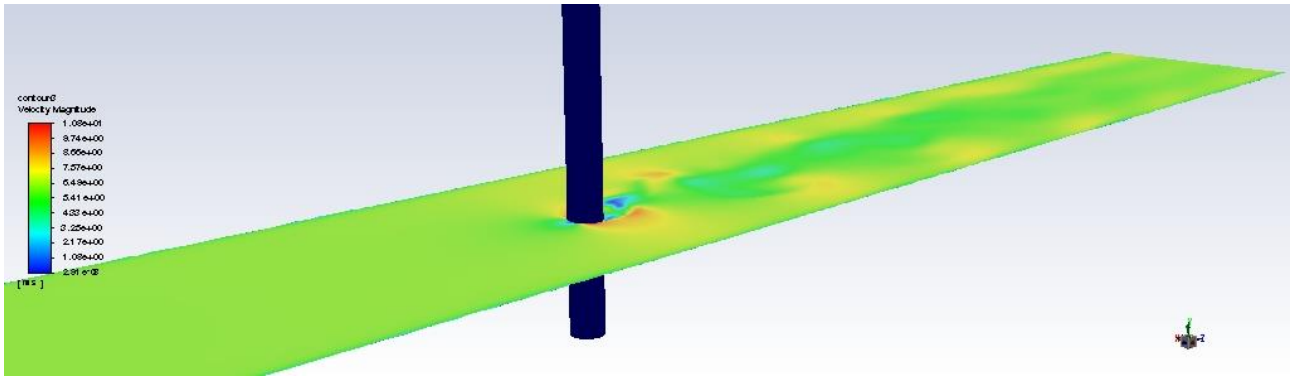**Figure 4.59: Velocity magnitude contours at *t=0.8425 s***

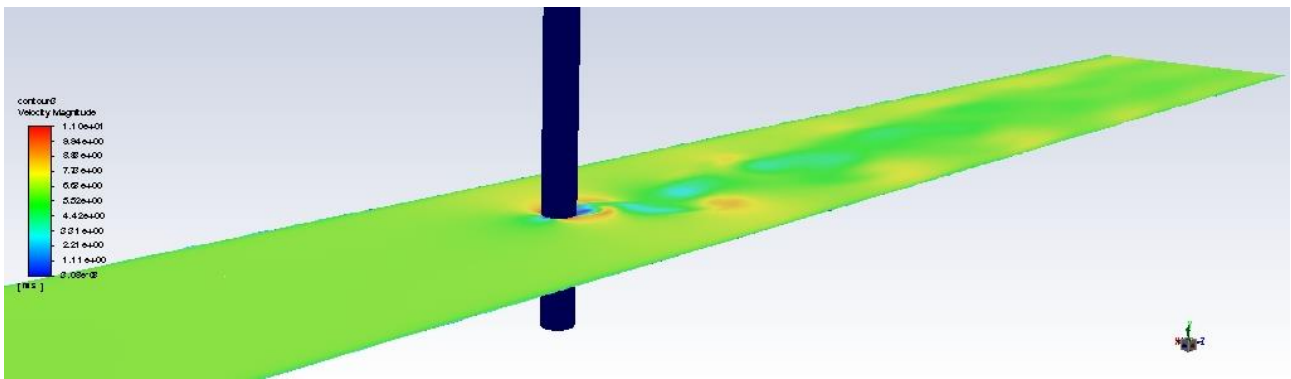**Figure 4.60: Velocity magnitude contours at *t=0.8525 s***

Figure 4.61: Velocity magnitude contours at *t=0.8625 s*
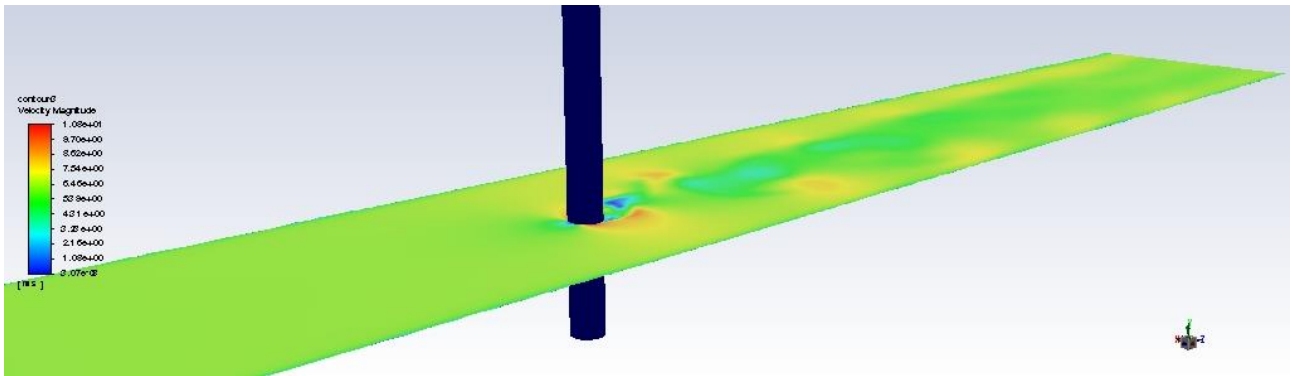

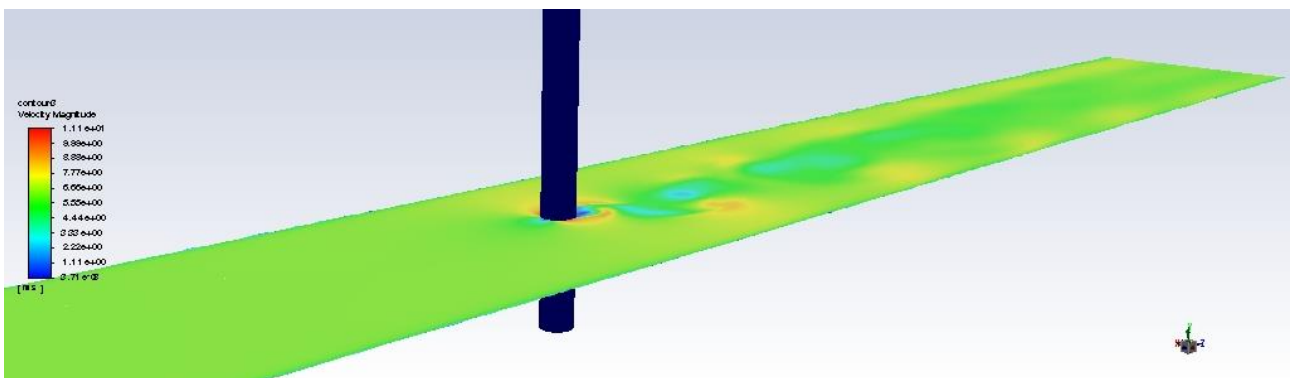**Figure 4.62: Velocity magnitude contours at *t=0.8725 s***

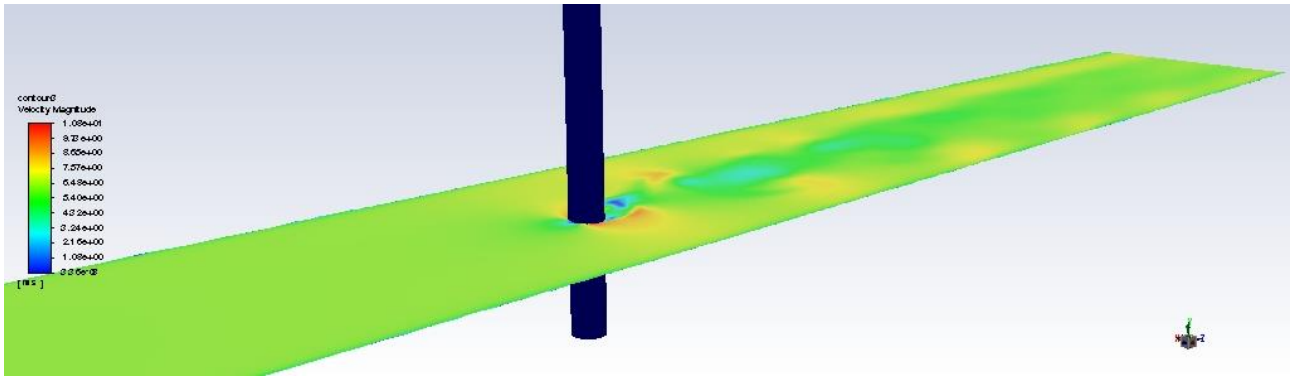**Figure 4.63: Velocity magnitude contours at *t=0.8825 s***

Figure 4.64: Velocity magnitude contours at *t=0.8925 s*

The thermowell oscillations and their synchronization with the vortex shedding are clearly visible.

In Figure 4.65 the temporal evolution of the lift on the thermowell surface is displayed.
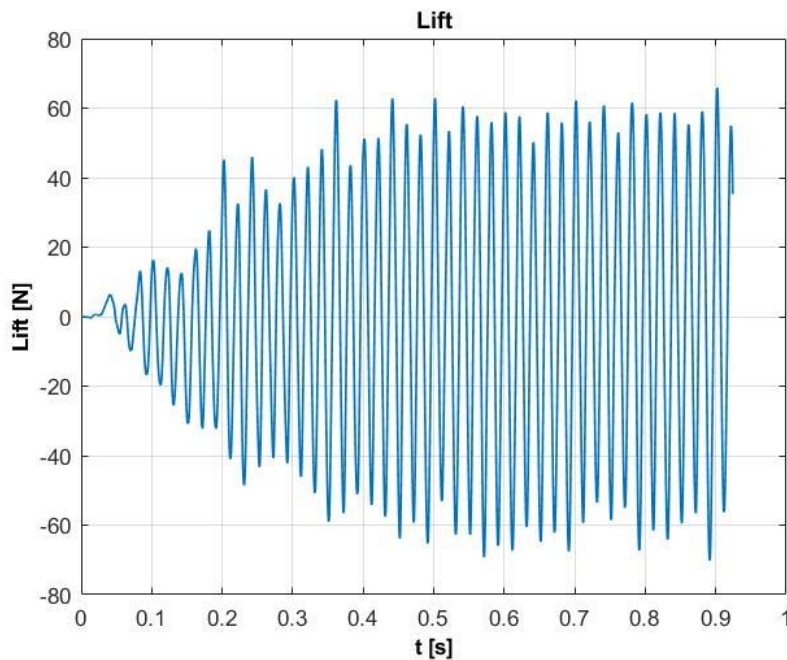
Figure 4.65: Temporal evolution of the lift on the thermowell

The temporal evolution of the transverse tip displacement was already displayed in Figure 4.57, in which the high amplitude of the tip motion caused by the vortex induced vibration can be appreciated. Moreover, as already stated in the previous section, it can be observed that the obtained results, namely the maximum RMS transverse tip displacement, are in perfect agreement with the available experimental data.

The temporal evolution of the streamwise tip displacement is shown in Figure 4.66. It can be observed that oscillations appear initially in the streamwise direction and afterwards the displacements in the transverse direction gain more importance, eventually becoming dominant.

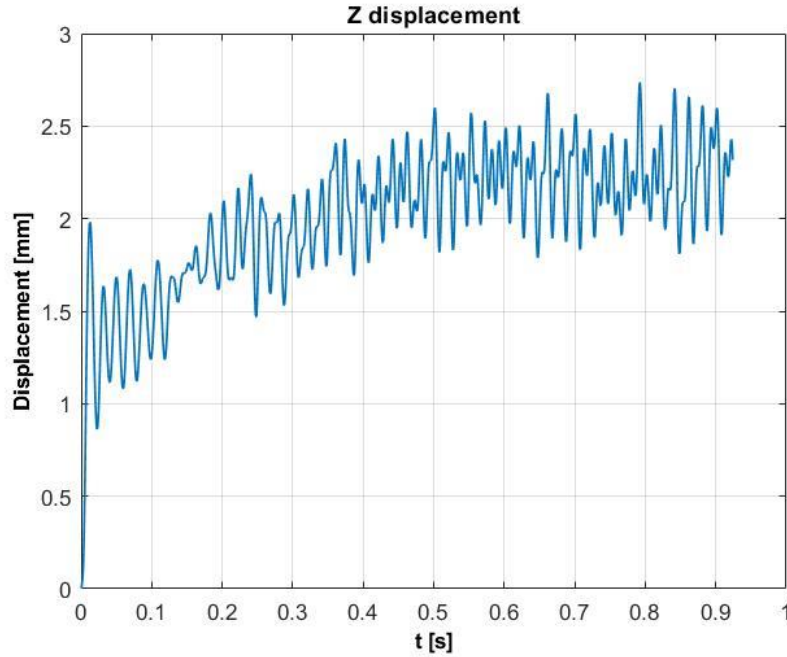**Figure 4.66: Temporal evolution of the streamwise tip displacement**

Comparing the temporal evolution of the lift (Figure 4.65) and of the transverse tip displacement (Figure 4.57), the synchronization between the vortex shedding and the thermowell oscillations is clearly visible, as already stated as a consequence of the observation of the velocity magnitude contours (from Figure 4.59 to Figure 4.64). This condition, as previously introduced, is referred to as "lock-in" and it is responsible for the observed vortex induced vibration. The capture of such condition was the aim of this thesis; hence, to validate the above deduced qualitative results, a quantitative analysis was carried out using the *pwelch* function in a similar way as in section 3.4. The obtained distributions of power spectral density of the two signals (the temporal evolution of the lift and of the transverse tip displacement) as a function of the frequency are shown in Figure 4.67.
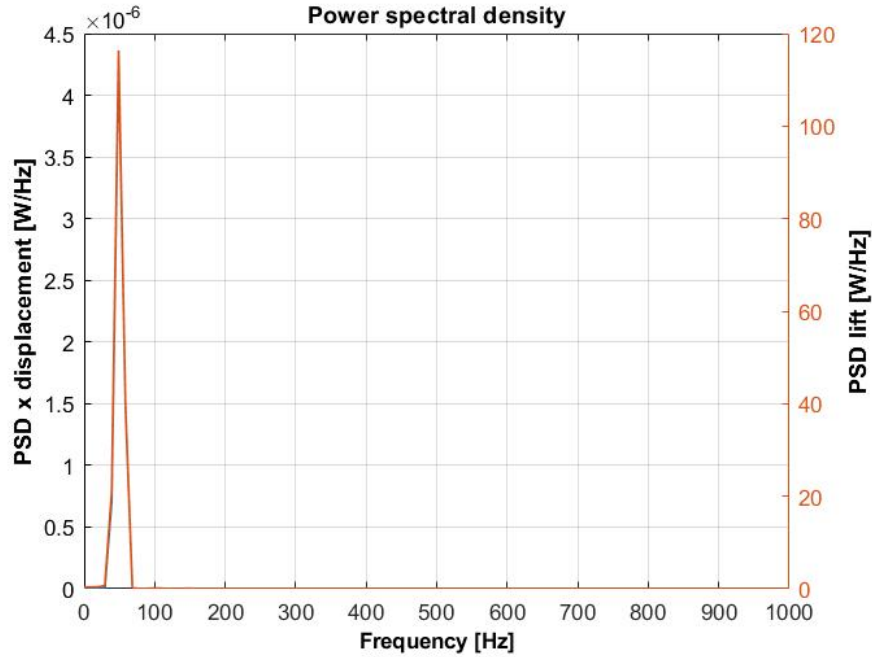
Figure 4.67: Power spectral density distributions of the lift and of the transverse tip displacement

Both signals are characterized by a dominant frequency of 48.8 Hz. Being the same, the lock-in condition is confirmed also from a quantitative point of view. In addition to that, the amplitude of the transverse tip displacement shows a quite constant value, a typical feature of the resonance phenomenon.

Moreover, it can be observed that the dominant frequency is very close to the first natural frequency of the thermowell (53.9 Hz), as expected from the obtained resonance, but with some deviation caused by the structural and the water damping.

This latter observation justifies also the choice of considering only the first six natural modes of the thermowell in the modal embedding (as stated at the end of subsection 4.3.1): in an unsteady FSI analysis using the modal superposition approach the modes truncation is performed retaining only the excited modes. In this application the excitation on the thermowell is the lift generated by the vortex shedding, characterized by a frequency close to the one associated with the first bending mode of the structure, hence the retention of the first two computed natural modes would be sufficient. Nevertheless, the first six modes were retained for the sake of safety.

In order to further confirm what has just been said, the temporal evolution of the modal coordinates of the first, the third and the fifth mode is displayed from Figure 4.68 to Figure 4.70. The difference in the order of magnitude between the modal coordinates associated with the different modes is clearly visible, confirming the negligible influence of the higher-frequency modes.
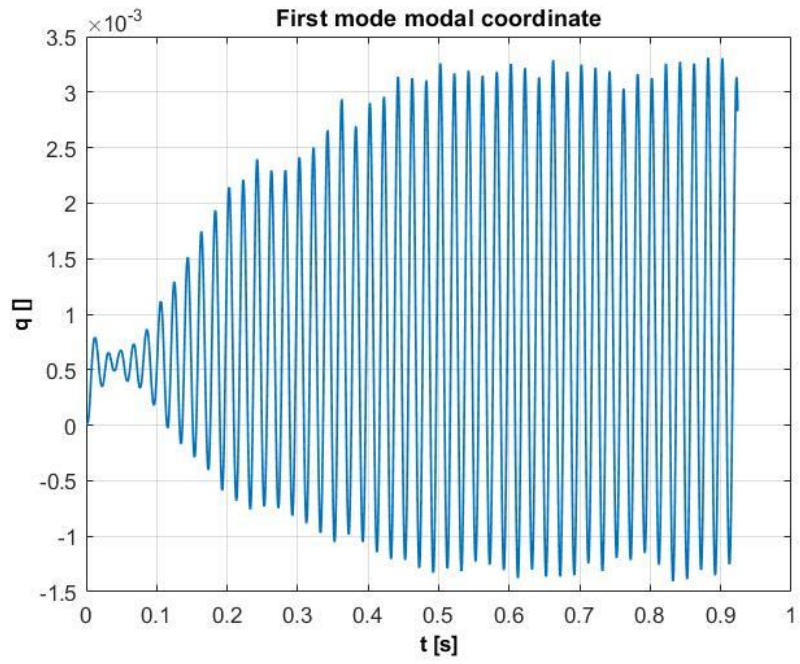
Figure 4.68: First mode modal coordinate temporal evolution
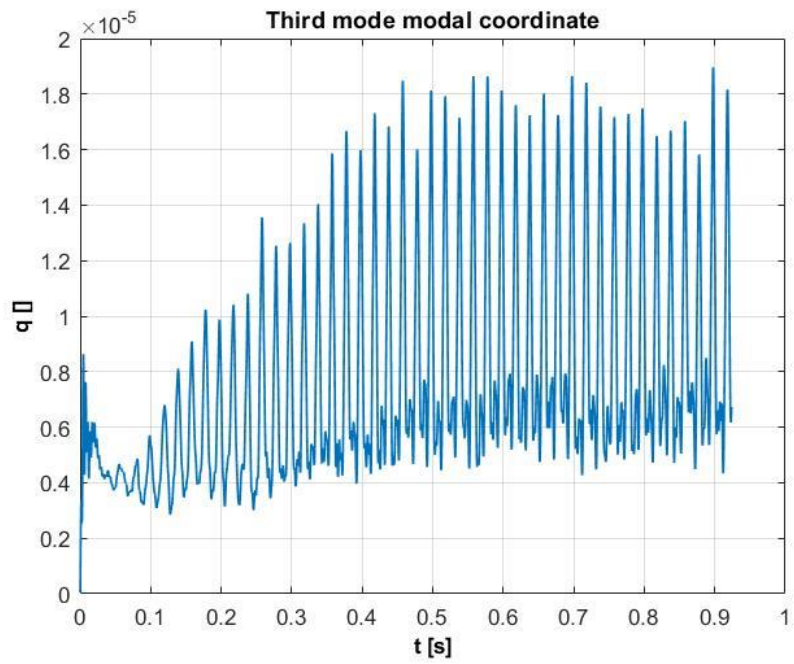
Figure 4.69: Third mode modal coordinate temporal evolution
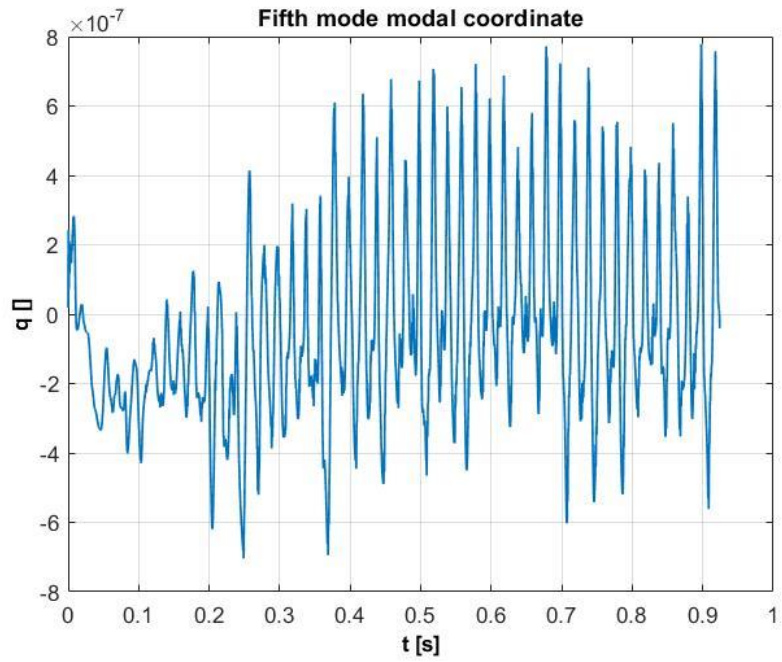
Figure 4.70: Fifth mode modal coordinate temporal evolution

From the exposed results it appears clear that the objective of the presented work was successfully achieved: by properly setting up the modal superposition method for the FSI analysis, it was possible to accurately simulate the vortex induced vibration of the thermowell, obtaining results in good agreement with the experimental data.

Conclusions

The presented thesis focused on an FSI approach based on modal superposition. Such approach, presented in the first sections, was then applied to an industrial problem with a transient analysis conducted computing the natural modes with ANSYS Mechanical and embedding them into ANSYS Fluent through the mesh morphing Add-On RBF Morph. This allowed the removal of the complex data mapping needed between the two solvers in a typical partitioned approach to the FSI study, making the proposed method faster and more robust.

At first the modal superposition approach for the FSI analyses was presented, explaining the theoretical background of all the used tools: the CFD analysis, the modal theory, the modal coordinates formulation, the modal superposition approach for the FSI analyses, the radial basis functions. All the introduced tools were then combined into a complete FSI workflow able to tackle the industrial problem object of this work.

In order to setup a reliable FSI analysis, a preliminary two-dimensional CFD study was carried out. The aim of such 2-D study was to define a computational grid and a CFD setup able to adequately capture the vortex shedding phenomenon. This latter task was accomplished and the obtained setup was validated through a comparison with experimental results available in the literature.

What was obtained through the 2-D study was then translated into a three-dimensional CFD setup modeling the experimental framework of the considered industrial problem: the vortex induced vibration of a thermowell immersed in a fluid flow. In order to implement the proposed FSI approach, the modal analysis of the thermowell was performed and its results, after a comparison with the analytical ones, were used to setup the RBF solutions of the modal shapes. The test of those solutions pointed out the necessity of corrective solutions to reduce the mesh distortion and they were eventually built and checked. After a high quality morphing configuration was obtained, the remaining part of the FSI setup was defined. Then several FSI calculations were performed in order to fine-tune the value of the damping ratio. Finally, a complete FSI setup able to accurately reproduce the experimental data was obtained.

The presented work demonstrated the reliability, the accuracy and the robustness of the proposed FSI transient solver, other than its speed and potential to be applied to complex industrial problems.

Further developments of this thesis might include gathering more comprehensive experimental data concerning the frequency of the thermowell vibration and the damping ratio of the system, in order to carry out a more in-depth evaluation of the obtained numerical results. Then the analysis could be extended to other fluid velocity to capture the lock-in region of the in-line vibration and the lock-off regions. Other mesh setups and turbulence models could be investigated (through a complete sensitivity study), comparing their results with the ones obtained with the proposed configuration. Moreover, the natural frequencies of the thermowell submerged in water could be calculated, in order to fine-tune the proposed FSI setup. Non-linearities could be introduced in the structural deformation, through additional corrective solutions, in order to assess their influence on the system dynamics.

Acknowledgements

Racchiudere in poche righe tutto ciò per cui sono grato giunto alla fine di questo percorso è veramente difficile. È stato un viaggio lungo e impegnativo, ma sicuramente pieno di bei momenti e grandi soddisfazioni, pertanto credo sia doveroso dedicare un pensiero a tutti coloro che ne sono stati protagonisti.

Innanzitutto, vorrei esprimere la mia gratitudine nei confronti del Prof. Marco Evangelos Biancolini, un mentore e fonte inesauribile di conoscenza, per il continuo supporto, la guida e i preziosi consigli che mi ha fornito durante lo svolgimento di questo lavoro di tesi e per avermi fatto scoprire e appassionare al mondo del Computer Aided Engineering. Un altro grande ringraziamento va al Dott. Ubaldo Cella per avermi fornito gli strumenti e le indicazioni necessarie per affrontare al meglio tutte le attività che hanno caratterizzato questo percorso di tesi. Di certo non può mancare in questo frangente un ringraziamento nei confronti di Antonio Martinez, Leonardo Geronzi e Stefano Porziani, per il supporto che mi hanno fornito nella risoluzione delle sfide che questa tesi mi ha posto.

Ringrazio i miei genitori, per avermi dato la possibilità di condurre e concludere con successo questi studi, per avermi sostenuto e per essere stati presenti in ogni momento del mio percorso. Mi avete reso ciò che sono e non ci sono parole che riescano ad esprimere quanto vi sono grato per questo.

Ringrazio Giulia per essermi sempre stata accanto e per avermi accompagnato in questa avventura, condividendo con me le gioie che l'hanno caratterizzata e sostenendomi anche nei momenti più difficili. Sicuramente ho richiesto tanta pazienza ma senza di te questi anni avrebbero avuto tutt'altro sapore.

Ringrazio gli amici di una vita Andrea, Samy e Lorenzo per avermi sostenuto, per avermi spronato a fare meglio e soprattutto per essere amici sempre presenti. Con voi ho condiviso alcuni dei momenti più belli di questi anni e li porterò sempre con me.

Ringrazio Alessio, un amico e una guida, per aver messo a disposizione la sua esperienza nei momenti che lo richiedevano e per avermi supportato e saputo consigliare al meglio. Grazie per le nostre lunghe chiacchierate al telefono, gli allenamenti e i sabati sera pieni di risate.

Ringrazio tutti i colleghi con cui ho avuto modo di condividere momenti di studio e svago durante questo percorso di studi; in particolare Giovanni e Mattia, amici e compagni sempre disponibili. Aver potuto lavorare con voi ai progetti più impegnativi del mio percorso di studi è stato un privilegio e una grande occasione di crescita personale e professionale.

Infine voglio ringraziare me stesso, perché se sono arrivato fin qui è anche merito mio.

Bibliography

[1] Van Dyke M., *"An album of fluid motion, volume 176"*, Parabolic Press Stanford, 1982;

[2] Williamson C. H. K., "*Vortex dynamics in the cylinder wake*", Annu. Rev. Fluid. Mech., 1996;

[3] Roshko A., *"Experiments on the flow past a circular cylinder at very high Reynolds number"*, J. Fluid Mech., 1961;

[4] Norberg C., *"Fluctuating lift on a circular cylinder: review and new measurements"*, Journal of Fluid and Structures. 2003;

[5] Blevins R. D., *"Flow Induced Vibration"*, Van Nostrand Reinhold Company New York, 1977;

[6] Gsell S. M., *"Vortex-induced vibrations of a rigid circular cylinder"*, Ph.D. thesis, Institut National Polytechnique de Toulouse, 2016;

[7] Verzicco R., *"Lezioni del corso di Fluidodinamica"*, Politecnico di Bari, 2001;

[8] Chung T. J., *"Computational fluid dynamics"*, Cambridge University press, 2002;

[9] Verzicco R., *"Appunti di turbolenza"*, Politecnico di Bari, 2006;

[10] Rodriguez S., *"Applied Computational Fluid Dynamics and Turbulence Modeling"*, Springer, 2019;

[11] Amalia E., Moelyadi M. A., Ihsan M., *"Effects of Turbulence Model and Numerical Time Steps on Von Karman Flow Behaviour and Drag Accuracy of Circular Cylinder"*, Journal of Physics: Conference Series 1005, 2018;

[12] Khan N. B., Ibrahim Z., Javed M. F., Jameel M., *"Numerical investigation of the vortex-induced vibration of an elastically mounted circular cylinder at high Reynolds number (Re = 10^4) and low mass ratio using the RANS code"*, PLoS ONE 12(10): e0185832, 2017;

[13] Cox J. S., Brentner K. S., Rumsey C. L., "*Computation of vortex shedding and radiated sound for a circular cylinder: subcritical to transcritical Reynolds numbers*", Theoretical and Computational Fluid Dynamics 12, 1998;

[14] McDonough J. M., *"Introductory lectures on turbulence: physics, mathematics and modeling"*, Departments of Mechanical Engineering and Mathematics, University of Kentucky, 2004;

[15] Pope S., *"Turbulent flows"*, Cambridge University Press, 2003;

[16] Manual, ANSYS FLUENT 12.0. Theory guide, Canonsburg, PA, 2009;

[17] Menter F. R., *"Zonal Two Equation k-w Turbulence Models for Aerodynamic Flows"*, AIAA Paper #93-2906, 24th Fluid Dynamics Conference, 1993;

[18] Menter F. R., *"Two-Equation Eddy-Viscosity Turbulence Models for Engineering Applications"*, AIAA Journal, vol. 32, no. 8, pp. 1598-1605, 1994;

[19] Di Domenico N., Groth C., Wade A., Berg T., Biancolini M. E., *"Fluid structure interaction analysis: vortex shedding induced vibrations"*, Procedia Structural Integrity, 8, 422–432, 2018;

[20] RBF Morph, *"RBF Morph User's Guide"*, 2020;

[21] Meirovitch L., *"Fundamentals of Vibrations"*, McGraw-Hill higher education, McGraw-Hill, 2001;

[22] Biancolini M. E., Cella U., Groth C., Genta M., *"Static Aeroelastic Analysis of an Aircraft Wind-Tunnel Model by Means of Modal RBF Mesh Updating"*, Journal of Aerospace Engineering 29, 2016;

[23] Costa E., Biancolini M. E., Groth C., Caridi D., Lavedrine J., Dupain G., *"Unsteady FSI analysis of a square array of tubes in water crossflow"*, Flexible Engineering Toward Green Aircraft, Springer, 2020;

[24] Costa E., Biancolini M. E., Groth C., Cella U., *"Validation of High Fidelity Computational Methods for Aeronautical FSI Analyses"*, Flexible Engineering Toward Green Aircraft, Springer, 2020;

[25] Emerson, https://www.emerson.com/en-us/asset-detail/rosemount-twisted-square-a-new-twist-on-thermowell-design-1800740, 2017;

[26] Rosemount, *"Rosemount^{TM} 114C Thermowells"*, Product Data Sheet, 2019;

[27] Boyer H. E., Gall T. L., *"Metals Handbook"*, Eds., American Society for Metals, Materials Park, OH, 1985;

[28] RBF Morph, *"RBF Morph – Modelling Guidelines and Best Practices Guide"*, 2020;

[29] Adams V., Askenazi A., *"Building Better Products with Finite Element Analysis"*, OnWord Press, Santa Fe, N. M., 1999;